2020

ASSESSMENT AND IMPROVEMENT OF COMPUTATIONAL FLUID DYNAMICS METHODS FOR SEPARATED TURBULENT FLOWS AT LOW REYNOLDS NUMBERS

Tom Mancuso
Michigan Technological University, tmancuso@mtu.edu

ASSESSMENT AND IMPROVEMENT OF COMPUTATIONAL FLUID DYNAMICS METHODS FOR SEPARATED TURBULENT FLOWS AT LOW REYNOLDS NUMBERS

By

Thomas Mancuso

A DISSERTATION

Submitted in partial fulfillment of the requirements for the degree of

DOCTOR OF PHILOSOPHY

In Mechanical Engineering - Engineering Mechanics

MICHIGAN TECHNOLOGICAL UNIVERSITY

2020

This dissertation has been approved in partial fulfillment of the requirements for the Degree of DOCTOR OF PHILOSOPHY in Mechanical Engineering-Engineering Mechanics.

Department of Mechanical Engineering - Engineering Mechanics

Dissertation Co-advisor: *Dr. Abhijit Mukherjee*

Dissertation Co-advisor: *Dr. Craig R. Friedrich*

Committee Member: *Dr. Fernando L. Ponta*

Committee Member: *Dr. Seong-Young Lee*

Committee Member: *Dr. Gustavo A. Ledezma*

Department Chair: *Dr. William Predebon*

TABLE OF CONTENTS

LIST OF FIGURES

LIST OF TABLES

PREFACE

This dissertation contains already published content. In addition, future publications are planned as listed below.

Already Published:

Preliminary Study on the Heat Transfer and Fluid Flow in Formed, Lap-Wound End Windings of Electric Machinery, Thomas Mancuso, Abhijit Mukherjee. Presented at International Mechanical Engineering Congress and Exposition, 2012

Planned Publications:

Effectiveness of turbulence modeling and turbulent scale resolving methods for low Reynolds number flows and their computational costs, Part 1 staggered tube bank, Thomas Mancuso, Abhijit Mukherjee. Journal of Thermal Science and Engineering Applications

Effectiveness of turbulence modeling and turbulent scale resolving methods for low Reynolds number flows and their computational costs, Part 2 Square in cross flow, Thomas Mancuso, Abhijit Mukherjee. Journal of Thermal Science and Engineering Applications

Modifications for the SST-SAS turbulence model for improved accuracy in low Reynolds number, separated flows, Thomas Mancuso, Abhijit Mukherjee, International Journal of Heat and Mass Transfer

ACKNOWLEDGEMENTS

I would like to thank Professor Abhijit Mukherjee for his tireless support and patience on this project. I also greatly appreciate the members of my committee for their valuable feedback and insight. I owe a deep debt to my family for their patience while I worked for so long on this project, without whom it would not have any meaning. I am grateful to my daughters Olivia and Alexandra for their understanding while dad was preoccupied. Finally, this work would not have been possible without my wife Barbara whose seemingly infinite patience and love for me allowed me to complete this work and still fulfill my family responsibilities.

NOMENCLATURE

Symbol or Abbr.	Description
a_1	0.31; A constant for the SST turbulent viscosity equation
CFD	Computational Fluid Dynamics
CFL	Courant-Friedrichs-Lewy number
C_s	Calibrated coefficient to adjust high wave number damping in SAS model
C_p	Fluid specific heat
D	Tube diameter and square length
DNS	Direct Numerical Simulation
DES	Detached Eddy Simulation
$\bar{e}$	Time averaged fluid energy
e'	Unsteady component of fluid energy
e	Fluid energy
f_k	Ratio of resolved-to-total turbulent kinetic energy
f_ω	Ratio of resolved-to-total specific dissipation
f_d	Empirical Delay function for DES model
F_1	First blending function for SST model
F_2	Second blending function for SST model
k	Turbulent kinetic energy
k_u	Unresolved turbulent kinetic energy
k_r	Resolve turbulent kinetic energy
k_t	Total turbulent kinetic energy
l	Turbulent length scale
l_{DDES}	Alternate turbulent length scale used in DES model
l_{LES}	LES length scale from the DES model
l_{RANS}	RANS turbulent length scale for DES model
$L_{\nu\kappa}$	Von Karman length scale
LDV	Laser Doppler Velocimetry
LES	Large Eddy Simulation
P	Pressure
P_k	Production of turbulent kinetic energy
Pr_t	Turbulent Prandtl number
PANS	Partially Averaged Navier Stokes Equations
Q_{SAS}	SAS modification to specific dissipation equation

Symbol or Abbr.	Description
RANS	Reynolds Averaged Navier Stokes
RNG	Reynolds Normalization Group
RSM	Reynolds Stress Model
SST	Shear Stress Transport
SRANS	Steady Reynolds Averaged Navier Stokes
S	Strain rate magnitude
u_i	Velocity vector
u_i'	Unsteady component of velocity vector
$\bar{u}_i$	Time averaged mean of velocity vector
$\widetilde{u_i}$	Phase averaged coherent velocity vector
U′	First velocity derivative
U′′	Second velocity derivative
UDF	User define function
URANS	Unsteady Reynolds Averaged Navier Stokes
x	Cartesian coordinate
y	Cartesian coordinate
y+	Non-dimensional wall distance, $y^+ \equiv y\sqrt{\frac{\tau_w}{\rho}}/\nu$
z	Cartesian coordinate
α	Blended coefficient for SST specific dissipation equation
α_1	5/9; SST model constant
α_2	0.44; SST model constant
β^*	0.09; model constant for SST turbulent kinetic energy equation
β	Blended coefficient for SST turbulent kinetic energy equation
β_1	3/40; SST model constant
β_2	0.0828; SST model constant
Δ	Local cell length, cube root of cell volume
δ_{ij}	Kronecker Delta
ν_t	Turbulent kinetic viscosity
μ_t	Turbulent viscosity
σ_k	Blended coefficient for SST turbulent kinetic energy equation
ρ	Fluid density
$\sigma_{k,1}$	0.85; Diffusion term of SST turbulent kinetic energy equation
$\sigma_{k,2}$	1.00; Diffusion term of SST turbulent kinetic energy equation
$\sigma_{\omega,1}$	0.5; Diffusion term of SST specific dissipation equation

Symbol or Abbr.	Description
$\sigma_{\omega,2}$	0.853; Diffusion term of SST specific dissipation equation
σ_{ω}	Blended coefficient for diffusion term of SST specific dissipation equation
η_2	Empirical constant for source term in SAS model
κ	0.41; von Karman constant
Ω	Vorticity rate magnitude
ω_u	Unresolved specific dissipation

ABSTRACT

This study investigates the accuracy of Computational Fluid Dynamics (CFD) models to predict heat transfer in turbulent separated flows at low Reynolds numbers. A novel improvement of a Scale Adaptive technique is also presented. A spectrum of turbulence models is used to simulate flow and heat transfer of two geometries; fully developed flow through a staggered tube bank and a square prism in cross flow. Experimental data for both local heat transfer and velocity data are available in the literature for these cases and have been used extensively evaluate various CFD methods. Six unsteady models were used and the results show that the unsteady Shear Stress Transport (SST) model provided good overall accuracy relative to the mean Nusselt number for both cases. However, the SST model failed to accurately predict local variations. The Partially Averaged Navier-Stokes variant of the SST model showed a marked improvement for both cases. The Dynamic Smagorinsky Large Eddy Simulation (LES) showed a much-improved fidelity to the local Nusselt but under predicted the actual values. The computational cost for the LES model was significant. In general, it was found that the computationally expensive models with higher degrees of resolved turbulence did not necessarily return more accurate results.

A Scale Adaptive Simulation (SAS) modification of the SST model (SAS-SST) is also used in this study. The SAS approach for the SST model adjusts the production term of the specific dissipation transport equation based on the second velocity derivative. This modification is intended to improve the SST model where local flow accelerations/

decelerations are detected, as occurs in separated flows. However, the local Nusselt number for the two cases considered were found to be generally less accurate than the baseline SST model. In this study a novel modification to this model was made to reduce the SAS contribution near stagnation points in the simulation. This was done through the Kato-Launder and production limiter modification in the SAS production term. The results showed only a slight improvement of the accuracy of the Nusselt number predictions. It is possible that further adjustments to the SAS terms and constants can be made to properly support and complement the stagnation point modification in this study and yield an overall better turbulence model.

1 INTRODUCTION

The desire of an industrial Computational Fluid Dynamics (CFD) engineer is to accurately predict flow and heat transfer performance for a geometry of interest with limited prior knowledge of the flow field. Many commercial codes are available that can allow qualified engineers to create detailed models in significantly shorter project cycles than previous decades. This is aided by the great strides have been made in the creation of model geometry through automated meshing and direct geometry import.

However, accurate solutions are naturally dependent on the selection of models to properly capture the physics of the problem. The non-linear pressure-velocity relationship of the Navier-Stokes equations along with the lack of a universal, fast and accurate turbulence model makes CFD uniquely challenging when compared to other numerical applications like stress-strain analysis. Commonly used steady, Reynolds Averaged Navier-Stokes (RANS) models have limitations that make it difficult to arrive at accurate solutions for some problems. This can be a particular challenge for CFD engineers because industrial flow problems are typically turbulent [1] and where engineers are looking to extract local heat transfer coefficients to analyze a convection-conduction (conjugate) problem.

An inherent characteristic of a conventional, steady conventional RANS method (k-ε[2], RNG k-ε[3], k-ω[1], or SST [4]) is the assumption of a single length scale at any location in the flow solution when there are in fact multiple length scales in play. Additionally,

these models require calibration of their respective closure coefficients to be used. This calibration is typically performed with boundary layer or free shear flows[1]. For similar conditions in an industrial application, these models would be expected to work well. However, these methods are less effective in situations where there is significant stream-line curvature and flow separation. In these cases, the turbulence production is not in equilibrium with the dissipation and the assumptions used to develop these models are no longer valid.

Other issues with RANS models include premature transition to turbulence and a failure to return to back laminar flow. Some authors have attempted to address these limitations by developing more sophisticated RANS models. These include models that attempt to prevent non-physical, discontinuous jumps from laminar to turbulent flows such as the Intermittency model [5] and transitional models [6]. Second moment closure models such as the Reynolds Stress Model (RSM) remove the isotropic assumption and calculate the Reynolds stresses in all 3 directions. Generally, this model should respond better to streamline curvature [1]. However, this refinement comes at a cost of calculating 6 new variables in addition to the dissipation term.

Large Eddy Simulation (LES) [7] is currently believed to be the solution to the persistent limitations of the RANS approach. Unlike Steady RANS (SRANS) where all the length scales are modeled, LES resolves the larger eddies in a flow field that are bigger than the local filter size, which is typically on the order of the local grid size. Turbulent scales that are smaller than the filter size are modeled through an isotropic eddy viscosity

model. LES is inherently transient in nature and requires sufficient mesh and temporal resolution to capture a sufficient amount of the turbulent energy (typically 80%. [8]) The fundamental drawback of this method is the increased mesh density and compute time required to complete a solution. Further, flow statistics must be recorded for a sufficient number of time steps and then averaged to determine the mean flow characteristics. The result is a significantly increased solution time.

1.1 Turbulent Energy Cascade

The spectrum of available CFD methods can be discussed in terms of the turbulence energy cascade [7], as shown in Figure 1-1. The curve represents the turbulent energy, E, in a flow as a function of the inverse of the turbulence length scale or wave number. The large scales (lower wave number) generally contain more energy, which break down to smaller scales until the Kolmogorov scale is reached and viscous dissipation converts the turbulent kinetic energy to heat [8].

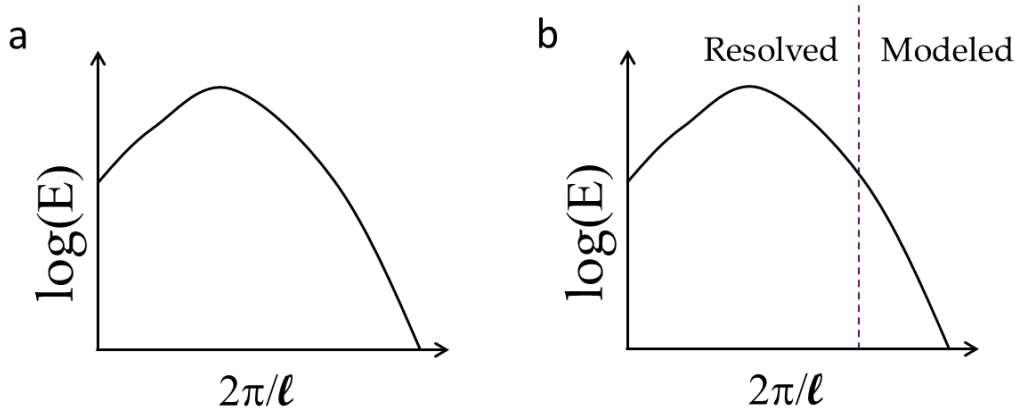

Figure 1-1 Turbulent Energy Cascade,(a), simulation approach for energy cascade for a defined separation of scales like that found LES (a).

With Direct Numerical Simulation (DNS), a transient solution resolves all of the length scales and the turbulent energy cascade of the simulation would be directly represented by Figure 1-1a. However, the mesh and time step size required to do this correctly requires computer resources that are not practical for industrial applications. In an SRANS solution, all of the length scales are modeled and the energy break down is controlled by the dissipation term, ε. In this case the physics of the energy cascade is not represented in the solution because only a single length scale is modeled. The resulting CFD solution generally requires significantly less compute time. With LES, the energy dissipation typically occurs at the local mesh size through the sub-grid viscosity model The local mesh size can be much larger than the Kolmogorov scale which significantly reduces the required mesh and temporal refinement. The separation of the resolved to modeled turbulence is finite with the LES approach, as shown in Figure 1-1b. The improvement of the LES approach can still require significant computational resources however.

Hybrid or bridging solutions can provide improvement over a RANS solution while avoiding the computational impact of LES. The simplest hybrid technique is to run a RANS model as an unsteady solution. This is often referred to as URANS. With this method, it is not possible to explicitly define the change from resolved vs. modeled turbulent energy. However, it can resolve the largest turbulent scales and is most appropriate where there is a large separation of scales like vortex shedding downstream of a bluff body [7]. It should be remembered that a RANS model is calibrated to match mean turbulent flows in a steady solution. Consequently, using them in an unsteady

mode is not specifically consistent with the intent of the model. It will be shown in this study however that switching to an unsteady mode can provide significant improvement in the accuracy of the solution, including the local Nusselt numbers.

The recently developed Partially Averaged Navier Stokes (PANS) [9] method uses a filtering approach that is similar to LES except that the degree of filtering, i.e. the ratio of unresolved to resolved kinetic energy and dissipation, is not be directly dependent on the local mesh size. For this model, the resolved-modeled dividing line is discrete based on the defined ratio of resolved to total turbulent energy. One benefit of the PANS approach is that is can be applied to any existing RANS model. Further, the model for the turbulent viscosity from the RANS model can benefit from the strengths of that model rather than a typically more simplistic sub-grid model used with LES.

Another recently developed hybrid modeling approach for turbulence modeling is the Scale Adaptive Simulation (SAS) [10, 11] which can be developed for any two equation turbulence model. SAS is typically a transient formulation that incorporates the local turbulent length scale found through the second velocity derivative. This method was developed to resolve more turbulence where local flow accelerations/ decelerations are detected. In other areas, the SAS modification is inactive and the model defaults back to the base condition. This can provide improved accuracy by better representing the transient turbulent eddies but within a URANS framework. This approach yields a significantly higher degree of resolved turbulence than a similar URANS solution.

With Detached Eddy Simulation (DES), which is a hybrid RANS-LES approach, the URANS solution is applied near the walls so that very fine meshes can be avoided. Further away from the walls, the model transitions to an LES solution. One aspect of this model is that resolving turbulent structures near the wall that may not occur with a DES model.

The present work with will evaluate the spectrum approaches listed for two well documented flow problems. These are a square prism in cross flow and fully developed flow in a staggered tube bank. These configurations were chosen because they feature the type of separate flow and large-scale transients than can be found in industrial applications. For both cases, local flow and heat transfer data is available to evaluate the accuracy of the models. The required compute time will also be considered in this study. This is not typically addressed in significant detail in the literature. The industrial user cannot benefit from enhanced methods if they require more computer resources than are available. The common assumption when considering this issue is that the incredible expansion in compute capability and steadily falling costs make the concerns about more computationally expensive models only temporary. However, for a given problem with fixed computational capability, the industrial user will always benefit from faster solutions to run more parametric variations and include more geometric detail in the model [12].

1.2 Applications

The two flow configurations that are evaluated in this study feature low Reynolds number, incompressible, turbulent flows with significant flow separation. These flow conditions are found in a wide variety of industrial applications. These include cooling flows in electronics as well as heat exchangers. Shell side flow through in tube banks will also experience this flow regime.

1.2.1 Electric Machinery

One area where these flow conditions are relevant is in the cooling of electric machinery. This would include motors and generators where a variety of machine topologies are used to create the shaft power output from electrical power input or the inverse. One topology for an electric generator uses a rotor that carries permanent magnets or energized copper windings to create a magnetic field. When this field sweeps through the armature, electric current is produced. This electric current will also create ohmic losses (I^2R) and due to its time varying nature, eddy current losses. As a result, proper cooling designs are required to maintain acceptable temperatures in the generator.

The operable temperature rise in the copper conductors in a generator is limited by the allowable temperatures of the ground wall insulation, typically on the order of 120°C to 200°C [13] depending on the insulation grade and conditions. The insulated generator components are designed to stay below this temperature and temperature model predictions are essential to achieving this goal.

Electric machines are typically cooled by forced convection through internal passages in the machine. Some larger units like those designed for large nuclear power plants use direct water cooling for certain components. However, convective heat transfer from the internal gas flow is a common method of heat removal. Hydrogen gas, rather than air, is frequently used in larger utility scale generators to enhance cooling capability. Hydrogen is used because of its favorable specific heat, thermal conductivity and density relative to air.

A number of authors [14-21] have investigated flow structures and heat transfer correlations of the stator end winding geometry found in nearly all synchronous turbo-generators used to produce electric power for distribution.

The internal flow passages of an electric machine are designed to effectively maintain allowable temperatures while at the same time limiting the parasitic power required to remove the heat. One example of the complex internal geometry is the stator bars for a lap wound machine [20]. The flow in this portion of the machine is generally radially inward or outward relative to the stator bars and can also have a tangential component. The application of simple heat transfer correlations may be impractical and inaccurate to use for this geometry. CFD can used to determine flow distributions and cooling performance the various components if machine specific experimental data is not available. However, these flow conditions present the same challenges to the models discussed earlier. The author has personal experience with using CFD models to predict convective heat transfer coefficients on this geometry. The SRANS SST model was

found to underpredict the heat transfer coefficient in the stator end winding. While the resulting design was successful, smaller stator windings could have been used to save cost while still staying below the temperature limits.

The prevalence of generators for electricity production is significant. The total global electricity generation was 20,225 billion kilowatt-hours in 2010, up from 14,612 billion kilowatt hours just 10 years earlier [22]. Nearly all of this production is dependent on the electric generator to convert mechanical energy to electric energy. Energy sources for this production include wind, natural gas, coal, hydro-electric, and nuclear. The use of electric motors for transportation and industry are no less ubiquitous.

Global wind energy has grown more than 10-fold over recent years, from 31.4 billion kilowatt hours in 2000 to 341 billion kilowatt hours in 2010. While this growth has been aided by subsidies from governments, the wind industry is expected to be competitive relative to other sources without these incentives. To achieve this end, wind turbines have grown in size both in terms of swept blade diameter and electrical output, in order to benefit from economies of scale. With generators for wind turbines, proper sizing can reduce the cost of the generator and prevent the compounding cost impact of up tower weight [23]. (The generator and gearbox drive train can account for 5-15% of the up-tower weight.) The application of accurate CFD methods that can be completed during a limited product development cycle can help enable the proper sizing of this equipment.

1.2.2 Other applications

Low Reynolds number (10,000-50,000) incompressible turbulent flow also exists in other industrial applications including electronics and heat exchangers. While flow and heat transfer in tube banks has been studied for some time [24-30] this topic has received more attention to more accurately predict flows in the heat exchanger of a nuclear reactor [31-35]. Other applications of an arrangement of cylinders in cross flow similar to tubed heat exchangers include pins fin heat sinks [36]. These are smaller in scale than typical heat exchangers and do not include internal flow. Pin fins are also frequently used for internal cooling of gas turbine blades [37].

All of these flows feature significant flow separation and flow unsteadiness that would challenge an SRANS approach. Additionally, the flow space of interest for a typical industrial problem is sufficiently large that memory and compute time of these problems for a CFD solution requires a judicious use of resources. As a result, an improvement in the accuracy of an SRANS solution that is more economical than an LES model is needed to aid CFD engineers in industrial settings to develop better products.

2 MODEL FORMULATION

2.1 Governing Equations

The conditions for the flow fields of interest are for transient, incompressible flow. The governing Navier-Stokes equations [38, 39] in Cartesian coordinates for these conditions can be written as

$$\frac{\partial u_i}{\partial x_i} = 0 \tag{1}$$

$$\rho \frac{\partial u_i}{\partial t} + \rho u_j \frac{\partial u_i}{\partial x_j} = -\frac{\partial P}{\partial x_i} + \mu \frac{\partial}{\partial x_j}\left(\frac{\partial u_i}{\partial x_j}\right) \tag{2}$$

$$\rho \frac{\partial e}{\partial t} + \rho u_j \frac{\partial e}{\partial x_i} = \frac{\partial}{\partial x_j}\left(k \frac{\partial T}{\partial x_j}\right) \tag{3}$$

Equations (1), (2), and (3) are sufficient to model any transient incompressible flow in DNS. However, the required time step and mesh size for an industrial turbulent flow problem would be too computationally expensive to be practical. This is because the dissipation of the energy from the momentum equation (2) would occur at very small scales relative the geometry and flow structures and these scales would need to be fully resolved in the solution.

The smallest, energy dissipative length scale is referred to as the Kolmogorov length scale. This and the related time scales [40]and are defined in equation (4).

$$\eta \equiv (\nu^3/\varepsilon)^{1/4}\ , \tau = (\nu/\varepsilon)^{1/2} \quad (4)$$

Here the smallest turbulent length scales, η are found from the kinematic viscosity, ν, of the fluid and the dissipation, ε, which is defined as $\varepsilon = 2\nu(S_{ij}S_{ij})$.

The Kolmogorov scale can be estimated for one of the cases in this study. For the square in cross flow case, the square is 0.03 m on a side and the inlet flow velocity is on the order of 10 m/s. The dissipation can be estimated as $\varepsilon = U^3/L$. Using the equations listed here yields a Kolmogorov length scale of $1.8\ x\ 10^{-5}$m and the time scale is $21\mu s$. The smallest cell size for the mesh used for the Large Eddy Simulation (LES) solution in this study was $2.5\ x\ 10^{-4}$m. This is an order of magnitude larger than the Kolmogorov scale. Further this small mesh was only used nearest the walls. Much larger cells were used in the wake area behind the square where the appropriate dissipation would be critical. The time step used for the LES solutions was $7.5\mu s$. A time scale for the turbulent eddies of $21\mu s$ would require time steps at least an order of magnitude smaller to properly resolve the flow. The net result would be a significantly finer mesh with a much finer time step than ultimately used for the LES solution. Therefore, the computational requirements to resolve these turbulent length scales in a DNS solution is impractical.

Modeling the turbulence allows for the appropriate dissipation of the eddies without resolving the turbulence. Reynolds averaging is used to develop a model for the turbulence for RANS models. The conservation equations can be re-written in terms of

the sum of the time averaged velocity, $\bar{u}_i$, and the random component, $u_i{}'$, rather than the instantaneous velocity, u_i.

$$u_i = \bar{u}_i + u_i{}' \tag{5}$$

Substituting this definition of velocity into Equations (1), (2) and (3) yields the same continuity equation (6) except it is written with $\bar{u}_i$ rather than u_i. The momentum equation (7) gains an additional term representing the Reynolds stress tensor $\tau_{ij} = -\rho\overline{u_i' u_j'}$. Likewise the replacement of the fluid energy, e, with the time averaged fluid energy $\bar{e}$ yields and the additional term in the energy equation (8) representing the turbulent heat flux, $\rho\overline{u_i' e'}$. For low speed flows the fluid energy can be represented by product of the specific heat and the static temperature. These equations are then written as

$$\frac{\partial \bar{u}_i}{\partial x_i} = 0 \tag{6}$$

$$\rho\frac{\partial \bar{u}_i}{\partial t} + \rho\bar{u}_j\frac{\partial \bar{u}_i}{\partial x_j} = -\frac{\partial \bar{P}}{\partial x_i} + \frac{\partial}{\partial x_j}\left(2\mu S_{ij} - \rho\overline{u_i' u_j'}\right) \tag{7}$$

$$\rho C_P\frac{\partial \bar{T}}{\partial t} + \rho C_P\bar{u}_j\frac{\partial \bar{T}}{\partial x_j} = \frac{\partial}{\partial x_j}\left(k\frac{\partial \bar{T}}{\partial x_j} - \overline{u_i' T'}\right) \tag{8}$$

These are the Unsteady Reynolds Averaged Navier Stokes (URANS) equations for incompressible flow. These equations are used as the basis for all the turbulence models used in the present study except for the LES model which is discussed later.

The Boussinesq approximation [1] is employed to model the Reynolds stress tensor and is calculated from the turbulent viscosity, ν_t,and the turbulent kinetic energy, k as shown in Equation (9).

$$\overline{u_i' u_j'} = \frac{2}{3} k \delta_{ij} - \nu_t \left(\frac{\partial u_i}{\partial x_j} + \frac{\partial u_j}{\partial x_i} \right) \tag{9}$$

The values for k and ν_t values are found during the simulation and the method to calculate these terms is presented later with each specific model.

All of the simulations in this study employ the gradient diffusion hypothesis [8] when solving the energy equation. This theorem states that the apparent turbulent heat flux ($\overline{u'_\iota T'}$) can be modeled by defining a turbulent Prandtl number and using the turbulent viscosity [41] to define an effective thermal conductivity as shown in Equation (10) and (11).

$$\overline{u_i' T'} = \frac{\mu_t}{\mathrm{Pr_t}} \left(\frac{\partial \bar{T}}{\partial x_j} \right) \tag{10}$$

$$\mathrm{k_{eff}} = \mathrm{k} + \frac{\mu_t C_p}{\mathrm{Pr_t}} \tag{11}$$

The energy equation can then be solved using an effective thermal conductivity rather than solving transport equations for the turbulent heat fluxes separately. This eliminates the need to solve three more transport equation in addition to the energy equation. This

approach is generally accepted in the literature. The turbulent Prandtl number used for all of the models in this study is 0.85.

For LES models, an alternate approach is used in developing the transient momentum and model closure equations. With LES, the velocity and fluid energy is filtered rather than averaged over a small physical volume in the flow space, typically the local cell of the mesh[7]. The turbulent scales larger than this filter size are resolved while the turbulent scales smaller than the filter size are modeled with the sub-grid model. The sub-grid model provides closure to the equations and it enables dissipation of the turbulence to occur at a much larger scale than the Kolmogorov scale. The turbulent scales smaller than the local mesh have lost their anisotropy and can be appropriately modeled as isotropic. Thus, the larger mesh and time step size enables a more practical solution than DNS. The Dynamic Smagorinsky-Lilly LES model [42] (or simply the Dynamic Smagorinsky model) is used in this study and specifics are presented in the next section.

For both flow cases under consideration for this study, the steady RANS models do not adequately model the flow after separation occurs. Specifically, the near wall eddies and the von Karman vortices do not develop in a steady solution and the solution that does develop is not an accurate time averaged solution for this flow field. Additionally, the solution shows very poor convergence characteristics in the wake region. A work around for this problem is to only model half of the flow space and to take advantage of the geometric symmetry. While a more robust convergence can be found when symmetry is used, the accuracy of the local velocity profiles and heat transfer coefficient on the heated

object was found to be poor. The accuracy of all the SRANS models are be greatly improved when run as an URANS model for the two cases considered in this study.

2.2 Turbulence Models

The six turbulent simulation techniques used in this study are presented in this section. There are multiple variations for these models presented in the literature so specific references are provided for each.

2.2.1 SST

Of the commonly available models, the SST model [4, 43, 44] has proven particularly effective for a wide range of situations. SST is a RANS that model combines the Launder k-ε model and the Wilcox k-ω model through the use of blending functions into a single model. In the boundary layer the k-ω model is used but then transitions to the k-ε model further away from the wall. This allows each model to be used for which its closure coefficients were calibrated. The transition is managed with a blending function to modify the coefficients in the transport model. This approach also addresses the sensitivity the k-ω model has to free stream values, as these are provided by the k-ε model. The k and ω transport equations are written in equations (12) and (13) [4]. Turbulent viscosity is found with equation (14).

$$\frac{\partial(\rho k)}{\partial t} + \frac{\partial(\rho u_j k)}{\partial x_j} = P_k - \beta^* \rho k \omega + \frac{\partial}{\partial x_j}\left(\mu + \sigma_k \mu_t \frac{\partial k}{\partial x_j}\right) \tag{12}$$

$$\frac{\partial(\rho\omega)}{\partial t}+\frac{\partial\left(\rho u_j\omega\right)}{\partial x_j}$$

$$=\alpha\frac{\rho P_k}{\mu_t}-\rho\beta\omega^2+2(1-F_1)\rho\frac{1}{\sigma_{\omega,2}}\frac{1}{\omega}\frac{\partial k}{\partial x_j}\frac{\partial\omega}{\partial x_j} \tag{13}$$

$$+\frac{\partial}{\partial x_j}\left(\mu+\sigma_\omega\mu_t\frac{\partial\omega}{\partial x_j}\right)$$

$$\nu_t=\frac{a_1 k}{\min\left(a_1\omega, SF_2\right)} \tag{14}$$

$$P_k=\mu_t S^2, \qquad S=\sqrt{2S_{ij}S_{ij}}, \qquad S_{ij}=\frac{1}{2}\left(\frac{\partial u_i}{\partial u_j}+\frac{\partial u_j}{\partial u_i}\right) \tag{15}$$

The F_1 blending function is defined as

$$F_1=tanh\left\{\left(min\left\{max\left(\frac{\sqrt{k}}{\beta^*\omega y},\frac{500\nu}{y^2\omega}\right),\frac{4\rho\sigma_{\omega2}k}{CD_{k\omega}y^2}\right\}\right)^4\right\} \tag{16}$$

The cross-diffusion term $CD_{k\omega}$ is defined as

$$CD_{k\omega}=max\left(2\rho\sigma_{\omega2}\frac{1}{\omega}\frac{\partial k}{\partial x_i}\frac{\partial\omega}{\partial x_i},10^{-10}\right) \tag{17}$$

The F_2 blending function is defined as

$$F_2=\tanh\left[\left\{max\left(\frac{\sqrt{k}}{\beta^*\omega y},\frac{500\nu}{y^2\omega}\right)\right\}^2\right] \tag{18}$$

The values for α and β are in Equation (13) are found from the with the F_1 blending function of the SST model. Similarly, σ_ω and σ_k are found from using the same blending equations and the constants from the k-ε and k-ω equations.

$$\alpha = F_1\alpha_1 + (1 - F_1)\alpha_2 \tag{19}$$

$$\beta = F_1\beta_1 + (1 - F_1)\beta_2 \tag{20}$$

The production of the turbulent kinetic energy term (15) can sometimes over predict the turbulence production at a stagnation point. Modifications to P_k can be made to address this issue. The changes include the Kato Launder [45] modification which uses the strain rate magnitude times the vorticity magnitude $(S\Omega)$ rather than the strain rate squared (S^2). The other modification is production limiter as presented with the original model. Used together these two modifications to the production term are written as

$$P_k = \min\left(\mu_t S\Omega, 10\beta^*\rho k\omega\right) \tag{21}$$

Both of these modifications are used in this study for P_k in the SST model as well as the variants of this model, namely the SST-SAS and PANS-SST. The values at the wall used the standard definitions [43], namely

$$\omega = \frac{6\upsilon}{\beta_1 y^2} \tag{22}$$

$$k = 0 \tag{23}$$

where y is the distance from the wall to the cell center. The SST model is typically implemented without wall functions and sufficient mesh resolution is required so that the first element is inside the viscous sub-layer (y+ ~ 1). Meeting this requirement allows the model to better represent flows where flow separation occurs than a model with wall functions.

2.2.2 Scale Adaptive Simulation

The Scale Adaptive Simulation (SAS)[10, 11] approach is a typically transient solution that provides a modification to the scale determining equation based on local von Karman length scale, L_{vk} [10]. By using this length scale, the model can identify areas of non-homogenous turbulence. As such, it is better able to capture turbulence in areas where flow separation and streamline curvature occur. This approach can be applied to any two-equation model and is used in this study as a variant of the SST model. The SAS modification is based on work originally presented by Rotta [46] that included an additional length scale containing term in the second scale resolving equation based on the third velocity derivative. While this initial derivation was found to be ineffective, it was later [10] improved upon to create the SAS model. In the present model, the von Karman length scale is calculated with the second velocity derivative. This allows the SAS modification to be activated in areas of flow separation but revert back to the baseline model when this is not the case.

The k equation for the SST-SAS model is the same as the SST model as shown in (12) as is the calculation of the turbulent viscosity. Equation (24) shows the ω equation for the SST-SAS model. This equation includes an additional source term, Q_{SAS}.

$$\frac{\partial(\rho\omega)}{\partial t}+\frac{\partial(\rho u_j\omega)}{\partial x_j} = \alpha\frac{\rho P_k}{\mu_t}-\rho\beta\omega^2+2(1-F_1)\rho\frac{1}{\sigma_{\omega,2}}\frac{\partial k}{\partial x_j}\frac{\partial\omega}{\partial x_j}+Q_{SAS} + \frac{\partial}{\partial x_j}\left(\Gamma_\omega\frac{\partial\omega}{\partial x_j}\right) \tag{24}$$

$$Q_{SAS}=\max\left[\rho\eta_2\kappa S^2\left(\frac{L}{L_{\nu\kappa}}\right)^2-C\frac{2\rho k}{\sigma_\Phi}\max\left(\frac{1}{\omega^2}\frac{\partial\omega}{\partial x_j}\frac{\partial\omega}{\partial x_j},\frac{1}{k^2}\frac{\partial k}{\partial x_j}\frac{\partial k}{\partial x_j}\right),0\right] \tag{25}$$

The Q_{SAS} term contains the ratio of the modeled length scale $\left(L=k^{1/2}/\beta^*\omega\right)$ to the von Karman turbulent length scale ($L_{VK}=\kappa|U'/U"|$). The term, $L/L_{\nu K}$, "allows the turbulence model to recognize resolved scales in unstable flows and to adjust the eddy-viscosity" [11]. The Q_{SAS} term serves to increase the local specific dissipation production in areas of inhomogeneous turbulence. Consequently, smaller scale eddies are resolved than would be found from the baseline SST model. This can lead to a more accurate prediction of the local heat transfer coefficient where flow separation has occurred. Because the two test cases in this study do show this type of flow characteristics, the SAS model would be expected to work well for these cases. However, this model was calibrated for higher Reynolds number. The results will show that the model in its present form is not well suited to this application

2.2.3 Reynolds Stress Model

The Reynolds Stress Model (RSM) [47], [48], [49] is a second moment closure model that models the Reynolds stress' ($\overline{u_i' u_j'}$) directly and does not rely on the Boussinesq hypothesis to determine a turbulent viscosity. Instead, the transport equation is solved for each Reynolds stress term. For a three-dimensional problem, the six Reynolds stress parameters must be solved, along with the specific dissipation to make seven simultaneous equations. The benefit of this model is that by not using Boussinesq hypothesis, which assumes isotropic turbulent stresses, it is better suited for flow with severe turbulent anisotropy.

The derivation of the Reynolds stress transport equation results in of many terms that cannot be calculated directly and must be modeled. These terms require significant ad hoc modeling and the use of tunable coefficients [50]. The Reynolds stress transport equation for incompressible, non-buoyant flow is written as

$$\rho\frac{\partial\overline{u_i'u_j'}}{\partial t}+\frac{\partial}{\partial x_k}\left(\rho u_k\overline{u_i'u_j'}\right)=-\rho\left(\overline{u_j'u_k'}\frac{\partial u_i}{\partial x_k}+\overline{u_i'u_k'}\frac{\partial u_j}{\partial x_k}\right)+$$

Transient and convection — Mean shear

$$\overline{p'\left(\frac{\partial u_i'}{\partial x_j}+\frac{\partial u_j'}{\partial x_i}\right)}-\frac{\partial}{\partial x_k}\left(\rho\overline{u_i'u_j'u_k'}+\overline{p'u_i'}\delta_{ik}+\overline{p'u_j'}\delta_{ik}-\mu\frac{\partial\overline{u_i'u_j'}}{\partial x_k}\right)$$

Pressure-Strain — Diffusion

$$-2\mu\overline{\frac{\partial u_i'}{\partial x_k}\frac{\partial u_j'}{\partial x_k}}$$

Viscous Dissipation

(26)

While the mean shear term can be calculated directly, the remaining terms, require modeling. Further development of the modeled terms is quite detailed and is not presented here. The specific dissipation term from the k-ω [1, 48] model is used to model the turbulent dissipation.

The additional computational requirements for this model from a standard two equation model are significant. A three-dimensional CFD solution requires the solution of transport equations for continuity, momentum for each direction in space and energy. For a two-equation turbulence model, this results in a sum of seven simultaneous equations. With the Reynolds stress model, the number is 12. The added computational

cost can only be justified if the improvement in accuracy is found for a particular problem.

2.2.4 Partially Averaged Navier-Stokes

The PANS model [9, 51] is an approach that re-evaluates the initial assumptions of the RANS derivation to only model a portion of the turbulence and allow the transient flow solution to resolve the rest. This model directly controls the ratio of the modeled (unresolved) to total turbulent kinetic energy. A PANS model is similar to an LES approach in that turbulent scales larger than the filter size are resolved while those smaller than the filter size modeled (or unresolved.)

The ratio of unresolved (modeled) to total turbulent kinetic energy f_k is written as

$$f_k = \frac{k_u}{k_t} = \frac{k_u}{k_r + k_u} \tag{27}$$

Similarly, the unresolved-to-total specific dissipation ratio is written as $f_\omega = \omega_u/\omega_t$. The unresolved turbulence is then modeled with the k_u and ω_u equations and the resolved turbulence is present in the transient flow solution.

The transport equation for k is the same as the standard SST model (Equation (12)) but the specific dissipation equation [52] is re-written as

$$\frac{\partial(\rho\omega_u)}{\partial t}+\frac{\partial(\rho u_j\omega_u)}{\partial x_j}$$

$$=\alpha\frac{\rho P_k}{\mu_t}-\left(\frac{1}{f_\omega}-1\right)\frac{\alpha\rho\beta^*\omega_u}{\mu_t}-\frac{\rho\beta{\omega_u}^2}{f_\omega} \tag{28}$$

$$+2(1-F_1)\rho\left(\frac{f_\omega}{f_k}\right)\frac{1}{\sigma_{\omega,2}}\frac{1}{\omega_u}\frac{\partial k}{\partial x_j}\frac{\partial\omega_u}{\partial x_j}+\frac{\partial}{\partial x_j}\left(\Gamma_\omega\frac{\partial\omega_u}{\partial x_j}\right)$$

The diffusion coefficients for the PANS solution are written as

$$\Gamma_k=\mu+\frac{\mu_t}{\sigma_k}\frac{f_\omega}{f_k}\qquad\Gamma_\omega=\mu+\frac{\mu_t}{\sigma_\omega}\frac{f_\omega}{f_k} \tag{29}$$

Inspection of Equation (28) shows that when $f_k = 1$ and $f_\omega = 1$, the equation collapses down to the standard ω transport equation (13). Conversely, when f_k and f_ω tend towards 0, the specific dissipation gets infinitely large. Accordingly, k would go to 0 as would the turbulent viscosity. The result would be a DNS solution as the turbulent model parameters have been suppressed.

When values for f_k are between 0 and 1, the specific dissipation is increased which leads to a reduction of the unresolved turbulent kinetic energy, as well as the turbulent viscosity. The transient solution then yields smaller turbulent length scales and more turbulent energy is captured in the flow transients and thus can more accurately capture the local flow physics. The local grid size is included in the calculation of f_k to determine if the local turbulent scales can be resolved. In this solution, all of the specific dissipation is unresolved, hence $f_\omega = 1$

A constant value of f_k for the entire flow space have been used [9, 53] but this does not take full advantage of this approach when the turbulent scales and cell size vary in the solution space. Methods have been developed that are based on the ratio of the local cell size $\Delta = (\Delta x \Delta y \Delta z)^{1/3}$ and the turbulent length scale

$$L = k^{1/2}/\beta^* \omega \tag{30}$$

Two methods to define f_k can be found in the literature [54]. The first is a derivation by adapting the Kolmogorov argument to define the minimum scale a grid can resolve as presented by Girimaji [51]. This expression is written as

$$f_k = 3(\Delta/(L))^{2/3} \tag{31}$$

This approach has been used in a number of papers [52, 55]. A more robust derivation used in the present study is based on the turbulent energy cascade as presented by Foroutan and Yavuzkurt [56]. These authors developed the relation provided in Equation (32).

$$f_k = 1 - \left[\frac{\left(\frac{L}{\Delta}\right)^{\frac{2}{3}}}{0.23 + \left(\frac{L}{\Delta}\right)^{\frac{2}{3}}} \right]^{4.5} \tag{32}$$

This expression yields noticeably lower values for f_k, as shown in Figure 2-1, than Equation (31). As a result, higher levels of resolved turbulence are found in the solution.

Additionally, this equation does not need to be clipped at 1 as required for equation (31) and provides a continuous response to the cell size to turbulent length scale ratio.

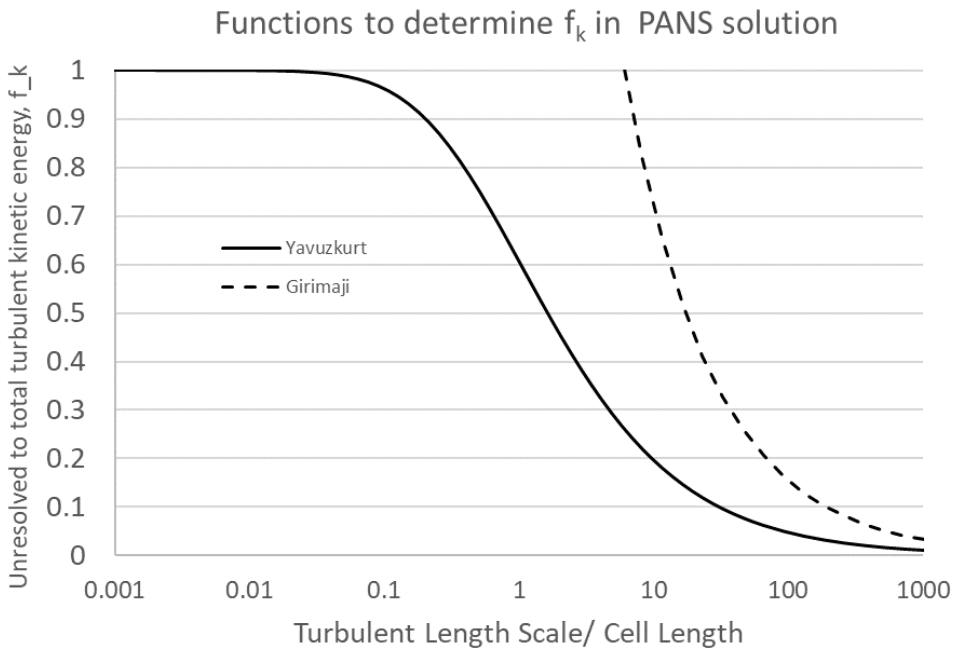

Figure 2-1 Function to determine f_k in PANS solution

The f_k field is determined through an iterative approach because the solution to the k and ω field in the flow space is coupled to f_k equation. From an initial condition, periodic updates to the f_k field is made and an updated time averaged flow field can be found. Successive iterations are needed until the f_k field is stable and the final transient run can be completed. As such, a PANS approach requires more computational time and more intervention from the user to create the solution.

To start, the unresolved turbulent kinetic energy is found from a steady RANS solution. This is an approximation of the actual field and its accuracy is limited by the RANS model itself. With the solution of the initial k field, equation (32) can be used to

calculate f_k in the flow space and this is used as an initial condition and the first part of the transient flow solution. With the f_k values fixed, the solution is run for a sufficient number of time steps to achieve a stable, time averaged solution. This solution can then be used to calculate the time averaged turbulent kinetic energy of the solution by the standard definition shown in equation (33)

$$k_r = \frac{1}{2}\overline{u_i' u_i'} \tag{33}$$

This value can then be used to determine the total turbulent kinetic energy from the sum of the unresolved and resolved components, namely

$$k_t = k_r + k_u \tag{34}$$

This updated turbulent kinetic energy is used in Equation (30) and Equation (32) to update the f_k field. With this calculation, the PANS method is determining the appropriate degree of resolved and unresolved turbulence based on the local mesh size and flow conditions. The solution is run again to update both resolved and unresolved turbulent values and this process is repeated until the f_k field has converged.

2.2.5 Detached Eddy Simulation

DES is hybrid approach that employs an unsteady RANS solution near the wall but transitions to an LES solution away from the wall. As such, a DES model requires a blending function to facilitate the transition between to two regions[57]. The same RANS model that is used for the near wall turbulence can also be used as a sub-grid

viscosity model. There are a number of DES approaches available in the literature and the Delayed DES (DDES) model [58] was used in the present study. DDES uses the SST model as the RANS and sub-grid viscosity model. It is calibrated with a number of test cases including a backward facing step where the Reynolds number of 28,000. This flow condition is similar to the two cases evaluated in the present study.

The turbulent kinetic energy equation for the DDES model is shown in Equation (35) while the specific dissipation equation for this model uses the standard found in the SST model (Equation (14).)

$$\frac{\partial(\rho k)}{\partial t} + \frac{\partial(\rho u_j k)}{\partial x_j} = P_k - \rho k^{\frac{3}{2}}/l_{DDES} + \frac{\partial}{\partial x_j}\left(\mu + \sigma_k \mu_t \frac{\partial k}{\partial x_j}\right) \quad (35)$$

This equation is slightly different from the standard SST turbulent kinetic energy equation. It separates out the standard RANS length scale for this model, $l_{RANS} = \sqrt{k}/C_\mu \omega$, and replaces it with an expression for the local turbulence length scale modeled in the DDES model, l_{DDES}. The l_{DDES} term is then calculated with conditional terms that evaluate whether to use the standard RANS model or an LES model based on local mesh size and flow conditions. This expression is show in Equation (36).

$$l_{DDES} = l_{RANS} - f_d \max(0, l_{LES} - l_{RANS}) \quad (36)$$

The length scale for the LES scales is shown in Equation (37) and the coefficient, C_{DES}, is determined by the standard blending function used in the SST model (Equation (38)) and the h_{max} is the maximum length of cell.

$$l_{LES} = C_{DES} h_{max} \tag{37}$$

$$C_{DES} = C_{DES1} F_1 + C_{DES2}(1 - F_1) \tag{38}$$

The empirical blending function, f_d is defined in Equations (39) and (40) and the tuning of the coefficients C_{d1} and C_{d2} can be found in [58]

$$f_d = 1 - \tanh\left[(C_{d1} r_d\right)^{C_{d2}} \tag{39}$$

$$r_d = \frac{\nu_t + \nu}{\kappa^2 d_w^2 \sqrt{0.5 * (S^2 + \Omega^2)}} \tag{40}$$

The DDES model is expected to facilitate a more accurate solution at locations away from the wall than the other hybrid solutions but may not be able to resolve the turbulent flow structures nearest the wall as well as LES would.

An alternate Detached Eddy Simulation, namely IDDES (Improved DDES) [58] was also attempted for the two cases in this study. However, the results for the local Nusselt number were inferior than those from the DDES model. This may be because IDDES uses a wall modeling approach which does not typically work well with heat transfer solutions.

2.2.6 Large Eddy Simulation

The derivation of the LES model is based on filtering rather than averaging the velocity or other parameter of interest [59]. The general filtering expression can be written as

$$\hat{\phi} = \int_{-\infty}^{+\infty} G(x-\xi)\phi(\xi)d\xi \tag{41}$$

Here the variable ϕ is operated on with the filtering function G(). The instantaneous value of ϕ as the sum of the filtered $\hat{\phi}$ and sub-grid value ϕ' are shown in equation (42)

$$\phi = \hat{\phi} + \phi' \tag{42}$$

The filtered term is resolved in the solution while the sub-grid term is modeled. A variety of filter types can be used [7]. These include a box, spectral cutoff and Gaussian.

Rewriting equation (42) for the velocity ($u_i = \hat{u}_i + u'$) and substituting it back in to the momentum equation results in filtered momentum equation, namely

$$\rho\frac{\hat{u}_i}{\partial t} + \rho\hat{u}_j\frac{\partial\hat{u}_i}{\partial x_j} = -\frac{\partial\hat{P}}{\partial x_i} + \frac{\partial\tau_{ij}}{\partial x_j} \tag{43}$$

The sub-grid stress tensor τ_{ij} is defined as [42]

$$\tau_{ij} = \left(\hat{u}_i\hat{u}_i - \widehat{u_i u_j}\right) \tag{44}$$

This is of course similar to the Reynolds Stress tensor used for a RANS derivation. To close this model, the sub-grid stress tensor is defined as

$$\tau_{ij} - \frac{1}{3}\delta_{ij}\tau_{kk} = 2C\Delta^2|\hat{S}|\hat{S}_{ij} \tag{45}$$

where $\hat{S} = \frac{1}{2}(\partial \hat{u}_i/\partial x_j + \partial \hat{u}_j/\partial x_i)$ and $|\hat{S}| = \left(2\hat{S}_{kl}\hat{S}_{kl}\right)^{1/2}$

The filter scale, Δ, is typically the local grid size. The only remaining item required to close the momentum equation is to define C, the Smagorinsky coefficient. It has been found that a single definition of C for the entire flow space does not yield satisfactory results [59]. The Dynamic Smagorinsky model solves this problem by dynamically calculating the local values for Smagorinsky coefficient in the flow field for every time step. This is achieved by creating a second filter that is typically twice the size of the original filter. These two definitions for the same sub-grid stress tensor yields multiple equations and one unknown. The method of least squares is then used to find the best fit solution for C. This procedure is required for each cell in the flow space and at every time step. Further, the Smagorinsky constant is clipped to keep it within reasonable values [48] , namely $0 < C < 0.23$.

In addition to the Dynamic Smagorinsky model, the Wall-Adapting Local Eddy-Viscosity (WALE) [60] model was also used for the two cases presented in this study. This model is intended to provide better behavior for wall bounded flows and also properly represent laminar flows when present [48]. However, it was found that the local Nusselt number values for the Dynamic Smagorinsky model more accurate than the WALE model for the cases presented here.

3 TEST CASES

Two test cases were chosen for this study represent the types of flows that can appear in industrial applications. The first is flow through a staggered tube bank. The specific case studied here is a small section of the tube bank where the flow is fully developed and periodic boundary conditions can be applied. The turbulence is relatively uniform across the flow space and is dominated by the effects of the boundary layers as well as the separation/ recirculation zone behind the tubes. The second case is a square prism in cross flow in a wind tunnel. At the inlet of the tunnel, the flow has a uniform profile with low turbulence intensity. The flow then impinges on the front surface of the square and then separates around the sides and rear, generating a von Karman vortex sheet with a significant periodic flow component. The turbulence is present very near the square and then dissipates downstream. Both cases have been thoroughly researched by a number of authors and the pedigree of the experimental data is well regarded.

3.1 Staggered tube bank

Flow around tube tanks has been studied extensively for some time [24-26, 28, 29, 32, 61-64]. These studies generally focused on determining the mean heat transfer coefficient on the external surface of the tube as well as the pressure drop. This information could be used to determine the shell side heat transfer coefficient and flow resistance when performing heat exchanger calculations. This work also focused on

generating correlations from wide variety of tube spacings so that the heat transfer performance of a tube arrangement not specifically tested could be predicted. [61]

For developing and improving CFD models, more detailed experimental data is required than bulk heat transfer and pressure drop values. A few studies have provided detailed flow profiles and local Nusselt numbers that vary at different angular locations around a tube [62, 65-68]. Of particular interest is the experiments performed by Meyer [68]. In this work, local Nusselt numbers were found for a staggered tube bank with the same spacing and Reynolds number as another study by Simonin and Barcouda[69] that measured the local velocity and Reynolds stress profiles in the flow. Together, these two data sets provide an excellent platform to evaluate the performance of CFD methods.

The flow study used Laser Doppler Velocimetry (LDV) to find instantaneous two component velocity values at a number of locations in one-unit cell of a fully developed region of the tube bank. The transient data was used to determine mean velocity values as well as the Reynolds stresses. A sketch of the tube bank layout from this experiment is shown in Figure 3-1.

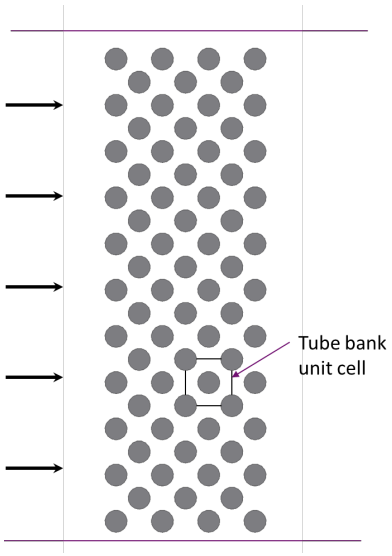

Figure 3-1 Experimental configuration for fully developed flow in a staggered tube bank

The tube diameters are 21.7 mm with a spacing of 45 mm and the normalized tube spacing (S/D) is 2.074 x 1.037. Time averaged velocity and Reynolds stress data is available at a number of locations in the periodic flow space as shown in Figure 3-2.

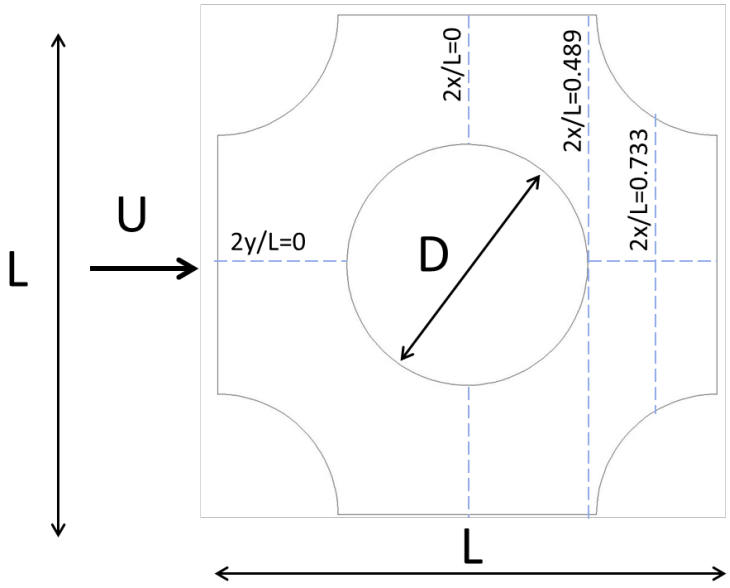

Figure 3-2 Locations for velocity and Reynolds stress profiles for fully developed flow in a staggered tube bank

The normalized locations for the measurements used by Simonin and Barcouda [69] is 2x/L or 2y/L. The center of the center tube is 0 and the limit of the model space as shown in Figure 3-2 is 1 or -1. This convention will be used in the present study.

With LDV measurements, two laser beams are directed at a single point at an acute angle and the resulting interference pattern allows the detection of the local velocity. Because the beams are at an angle, the location where the beams cross cannot be placed very close to the wall. For this reason, the velocity and Reynolds stress data are not available near the wall. This data is available at the ERCOFTAC Classic database [70].

The Meyer [68] experiments were performed in air to find the local heat transfer coefficients. A staggered tube bank array is created with steel tube tubes with a diameter of 45 mm with the same spacing ratios that were used for the flow experiments [69]. In the 5th of 7 rows, one acrylic tube is wrapped with a gold coated mylar sheet. When current is applied to the sheet, a uniform heat flux is created. At one point on the sheet thermocouples are attached to the back side of the film to provide the local temperature. With knowledge of the inlet air temperature, the heat flux and the local surface temperature, the local Nusselt number can be found.

The heated tube can be rotated a with better than 1° angular accuracy. This allows the Nusselt number to be found at all locations around the tube with a single thermocouple. The data was corrected to account for radiation and conduction heat transfer along with the temperature dependency of the gold layer electrical resistance so that the adjusted

heat flux can be used to provide accurate data. The accuracy of the data is reported to be +/- 3% of the Nusselt number at the front and sides of the tube and +/- 5% on the rear.

The stated Reynolds number for the flow experiments is 18,000. This calculation is based on the tube diameter and the flow velocity prior to entering the tube bank. It is more typical however for the Reynolds number for a tube bank to be defined from on the max velocity (i.e. min flow area) [25]. The higher velocity found in this area, rather than the open flow prior to entering the tube bank results in a Reynolds number of 40,000 rather than 18,000. While the Meyer data is reported to be taken at a Reynolds number of 40,000, it is the same flow condition as Simonin and Barcouda data. The results in this study are reported as having the higher although equivalent Reynolds number of 40,000.

The local Nusselt numbers are reported as an angular position relative to the stagnation point on the center tube as shown in Figure 3-3. The value of 0° correspond to the front stagnation point and the angle of 180° corresponds to the opposite side.

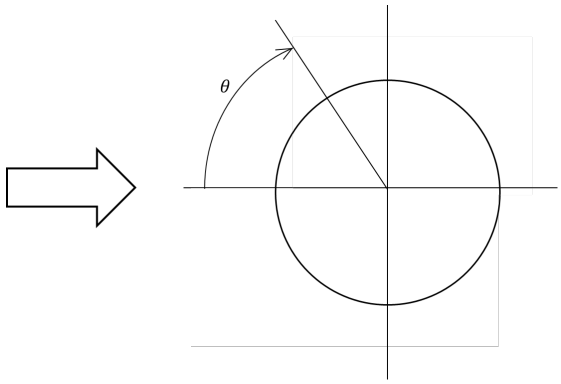

Figure 3-3 The angle θ from the stagnation point on the tube

The local Nusselt number data from this experiment, along with the error bars is shown in Figure 3-4.

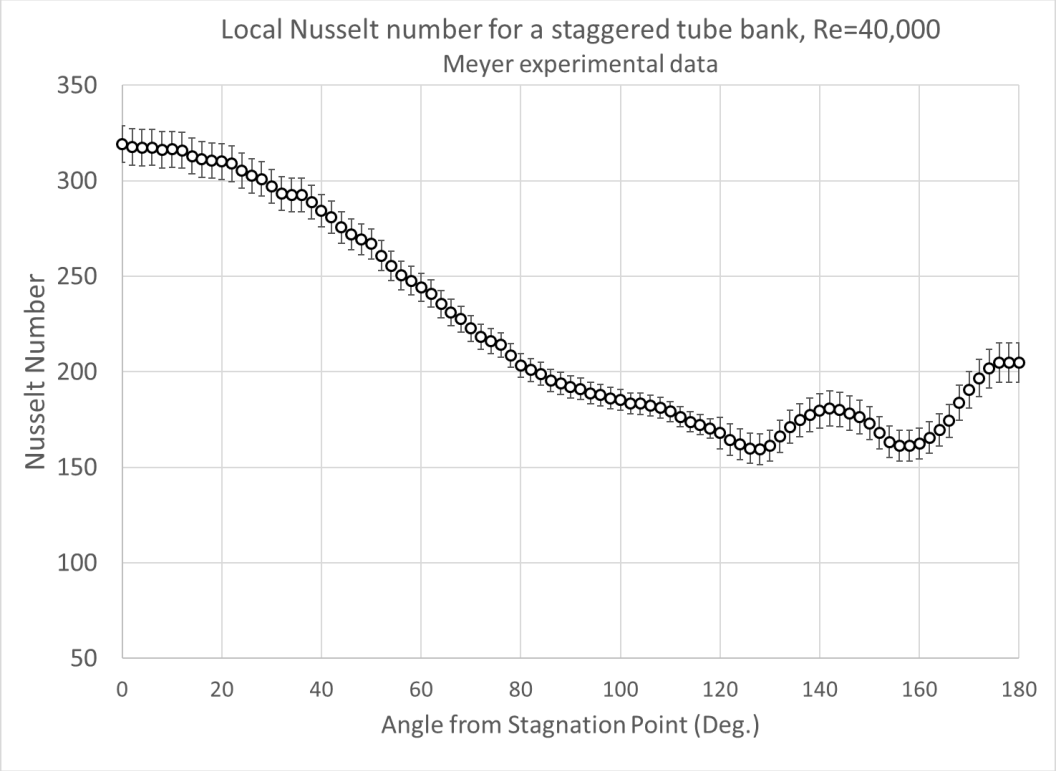

Figure 3-4 Local Nusselt number data for staggered tube bank from Meyer [68]

The mean Nusselt number from this data is 222.4 and while a tube bank correlation [25] provides a value of 203.9 [68] resulting in an error 9.1%. Since the stated accuracy of this correlation is +/- 15%, it confirms the accuracy of the experimental results.

Meyer lists the mean Nusselt number for the experimental data as 192.8 but this value is incorrect based on the average of the data shown in Figure 3-4. Since this data was extracted from a figure where the Nusselt number is normalized by the Reynolds number to the 0.6 power it is appropriate ensure the data extraction was conducted accurately. Meyer [68] also presents experimental local and mean heat transfer data for an additional normalized tube spacing of 2.0 x 2.0 at a Reynolds number of 41,500. This is nearly identical to the 40,000 value for the 2.074 x 1.037 data used in this study. The mean

experimental Nusselt number for the 2.0 x 2.0 case is reported as 190.7. However, the local Nusselt number for both cases as shown in Figure 3-5 clearly shows higher overall values for the 2.074 x 1.037 case. Therefore the 222.4 mean Nusselt value for the data shown in Figure 3-4 is correct and will be used to compare against the CFD cases rather than the 192.8 value reported by Meyer.

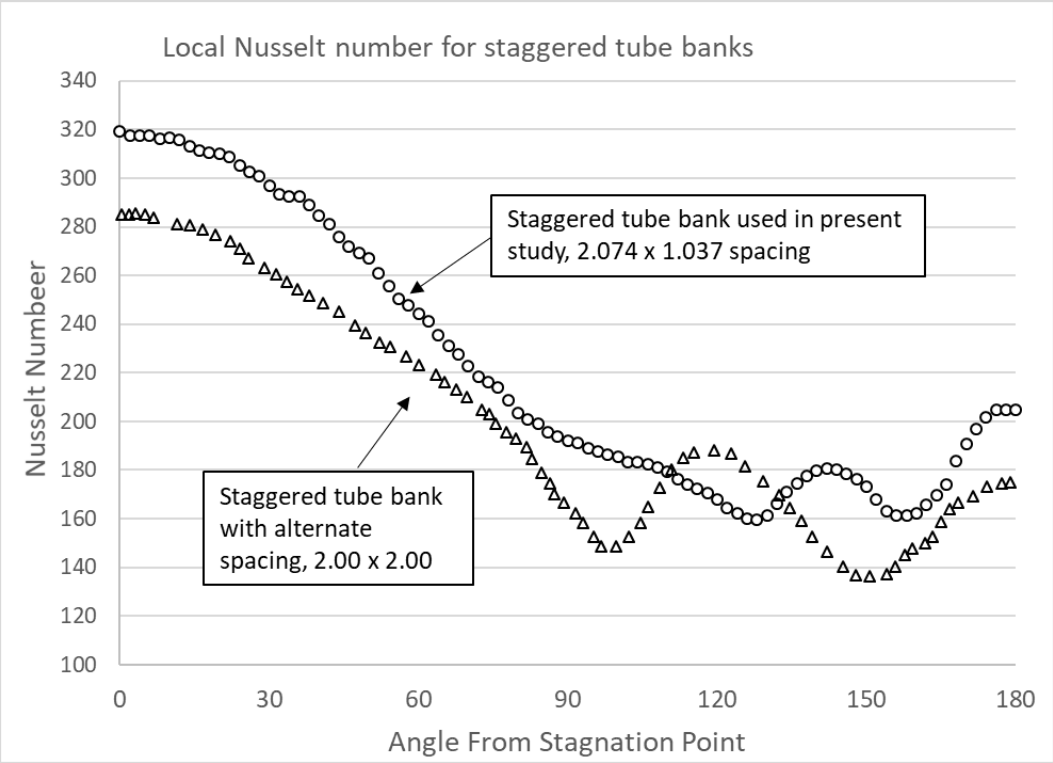

Figure 3-5 Local Nusselt found by experiment two tube bank configurations Meyer [68]

It is also interesting to compare the local Nusselt values for the two spacings provided in Figure 3-5. The tighter tube spacing of the 2.074 x 1.037 shows higher heat transfer as already discussed for a similar Reynolds number. The general shapes of the curves are the same, with two distinct 'bumps' where the local heat transfer is increased. In both cases, the second bump that peaks at 180° results from the separated flow impinging on

the rear surface. The first bump is due to a small eddy that develops between this point and the point where the flow first separates. The case with the wider tube spacing shows earlier flow separation because the flow is less constrained.

The flow and heat transfer data have been used to evaluate CFD models by a number of researchers. Recently a number of authors [35, 71, 72] studied flows through tubes banks as part of larger DOE study on Very High Temperature (Gas) Cooler Reactor (VHTR) for use in a nuclear reactor. This work focused on the ability of a spectrum of scale modeling and scale resolving methods to accurately predict flows in tube banks. The steady RANS models [72](k-ε, RNG k-ε, SST, and RSM) were all found to provide "marginal to poor" results. In the second part of this study [73] simply using these same models in a unsteady mode resulted in a significant improvement in the accuracy of for the velocity and Reynolds stress predictions.[74]

The staggered tube bank flow data was used to compare an LES approach using a Smagorinsky model to a PANS modification of a three equation variant of the k-ε model [55]. This study used a mesh for the PANS solution that is that is more than an order of magnitude finer than that used for the present study. The LES mesh was four times finer. The results showed that the PANS approach yielded similar results than the LES model although the LES mesh was twice the cell count.

In another study [75] a fine and course LES simulation along with an unsteady RSM model was employed to match the flow data. This study was run at a lower Reynolds number (9,000) to limit the mesh refinement required to resolve a sufficient portion of the

turbulence. The results of both models were comparable except in the near wall region. This study also references two other DNS [74, 76] studies to compare the results of their study. The LES results were found to match well relative to the DNS study. The RSM model results were also satisfactory.

While the experimental flow data alone has received a lot of attention as a platform to evaluate CFD methods, the heat transfer experiments have been leveraged less in the literature. The Meyer experimental data for the 2.0 x 2.0 normalized spacing was used to benchmark a numerical study to optimize the tube bundle spacing [77]. This work used a number of SRANS models to evaluate experimental data sets including the Meyer data. This study found that the RNG k-e model provided a very good match until flow separation occurred at about 90° past the stagnation point. This result was used to understand the optimal spacing of the tubes based on the calibration from the Meyer data. Another study by the same author [78] extended these results to three dimension by varying the width of the flow area between plates perpendicular to the tubes.

Finally, a few studies have looked at closely related topics. These include unsteady heat transfer and velocity data in a tube bundle along with an evaluation of the coherence between the two [62]. Another is an experimental and computational study of flow in a staggered tube bank with a Reynolds number of 9,300 [32]. The SRANS methods were found to not predict the flow and turbulence quantities well.

In summary it has been shown that URANS and scale resolving models will show improved accuracy for the staggered tube bank. The benefits of the more

computationally expensive methods relative to the accuracy will be determined in the present study. In addition, evaluation of URANS and scale resolving methods with the Meyer data has not yet been published. Evaluating the accuracy of the CFD methods for this case, in addition to the flow data provides a contribution to the existing knowledge in this area.

3.2 Square in cross flow

As with the staggered tube bank, experimental flow and heat transfer data is available in the published literature for a square prism (or cylinder) in cross flow for nearly identical conditions. For these cases, the prism is tested in a wind tunnel with a low inlet turbulence intensity, flowing left to right as shown in Figure 3-6. The square causes significant flow separation and a von Karman vortex sheet is created in the rear of the object.

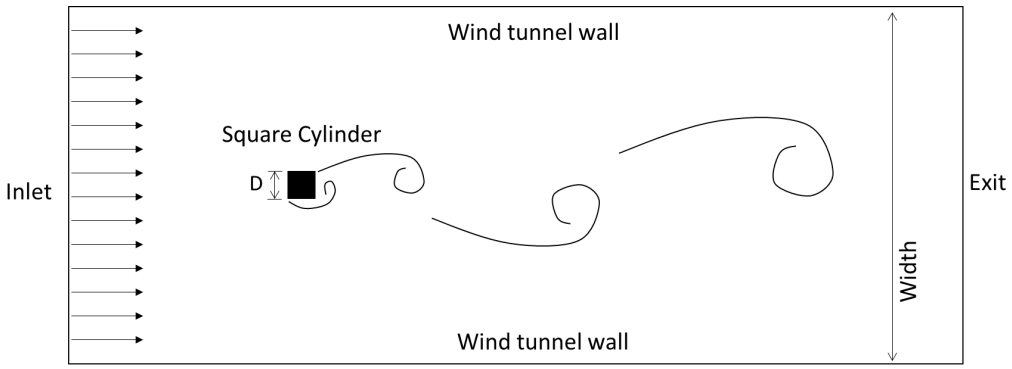

Figure 3-6 General wind tunnel configuration for thermal and flow measurement

One of the most common shapes to study in this context is a one with a circular cross section. Experimental data is available for both the local flow field and the location of

flow detachment. Local heat transfer coefficients have also been found experimentally [79].

The square prism has also been evaluated, but to a lesser extent. The square differs from the circular prism because the flow will separate at the front corners of the square while the separation location on the cylinder will be dependent on the inlet turbulence and the Reynolds number, among other factors.

The flow for the square data is provided by Lyn et al. [80]. This study used a two component LDV system to measure u- and v-velocity data at a large number of cross sections as shown in Figure 3-7. This figure also provides a cross reference to locations on that square surface for the local Nusselt number data for the heat transfer data.

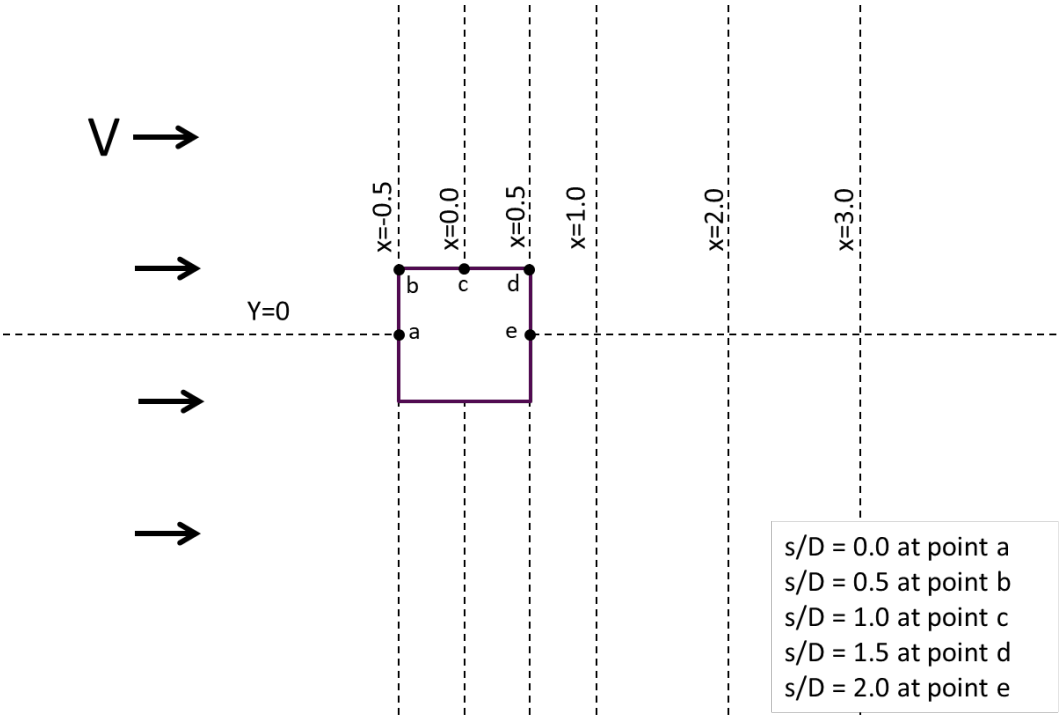

Figure 3-7 Square in cross flow, selected locations for data collection [80] with cross referenced locations for the heat transfer data from Igarashi [81]

This study was performed in water with a Reynolds number of 21,400. The square prism was D=40 mm on a side and the flow channel was 560 mm wide, perpendicular to the flow direction. This makes the normalized flow channel width 14D the blockage area of the prism is 7.1%. The channel is 9.75D deep and the inlet turbulence intensity is 2%. The reported Strouhal number ($St \equiv fD/U$) for this case is 0.132 +/- 0.004.

The time averaged velocity and Reynolds stress data is available at the ERCOFTAC Classic database [70]. The flow data is a standard benchmark for URANS and LES analysis [45, 52, 53, 82-84]. This includes the development of the Kato-Launder modification of the turbulent kinetic energy production term [45] as well as the PANS model [53]

he local heat transfer coefficient data was created by Igarashi for a range of Reynolds numbers (5,600 to 56,000) [81, 85] and for a number of angles of incidence (0° to 45°) for the square in the wind tunnel. The test data used in the present study is for a Reynolds number of 18,500 based on the free stream velocity and the side length, D, of the square. In the Igarashi experiment, the square is 30mm (D) on a side while the wind tunnel was 400 mm (13.3D) wide in direction transverse to the flow. The wind tunnel is 800 mm long in the flow direction and the square prism is 150 mm (5D) tall. This configuration results in a blockage factor of 7.5%. The inlet turbulent intensity is 0.5%

A 0.02 mm stainless-steel sheet is folded around a square acrylic bar and alternating current is applied through the metal to generate a uniform heat flux. Copper-Constantan thermocouples are mounted on the surface of the metal determine the local temperature. The heat transfer coefficient is based on the heated surface temperatures and the inlet air temperature. The measurement accuracy is not provided in these papers but the same author conducted a very similar experiment and a later paper [86] and report a measurement accuracy of +/- 5%.

The experimental correlation developed for the mean Nusselt number data from this experiment is

$$Nu = CRe^{n} \tag{46}$$

The mean and side specific values for the coefficients C and n in this equation are provided in Table 3-1

Table 3-1 Coefficients for Nusselt number experimental correlation for square in cross flow [81, 85]

	C	n	Nu for Re=18,500
Total	0.14	2/3	97.9
Front	0.64	1/2	87.0
Sides	0.131	2/3	91.6
Back	0.173	2/3	121.0

The exponent provided from this paper [81] is listed at 0.66 rather than 2/3. However, using 0.66 results in an overall mean Nusselt number of 91.7 which is below the arithmetic average of the values found for each side of the square from their respective correlations. Consequently, 2/3 was probably the intend value rather than the truncated 0.66.

The flow and heat transfer data together provide an excellent data set to evaluate the effectiveness of CFD methods to predict local flow fields and heat transfer coefficients. The Reynolds number for the flow data is 21,400 while the Reynolds number for the heat transfer data is nearly the same at 18,500. Likewise, the water tunnel for the flow data is slightly wider with a percent blockage of 7.1% instead of 7.5% for the heat transfer experiments. These conditions are close enough that the heat transfer and flow data can be evaluated together. The CFD model for this study is based on the heat transfer tests.

This combined data set has been used in a number of recent studies. This includes the development of the PANS-SST model [52] used in the present study. In this paper a wall resolved and wall function approaches were used. Not surprisingly, the wall resolved case showed a better match to the local Nusselt number around the square. The

velocity and Reynolds stress data also showed very good results. Another study used the Lyn dataset only to evaluate improvements of a PANS- k-ω model [82]. These authors evaluated an alternate method to determine the ratio of resolved to total turbulence kinetic energy than the one used in this study. The results showed that the flow profiles as well as drag coefficients and Strouhal numbers could be predicted accurately with a coarser mesh than one required for an LES solution. A similar result was found in another study using a PANS-k-ε model [53].

In summary, both of the test cases have been used to assess and improve a variety of CFD models. They also present an opportunity to asses two different flow configurations at an approximately the same Reynolds number. Consequently, the conclusions drawn from the results from both cases will carry more weight than either one of them alone.

4 METHODS OF ANALYSIS

4.1 Mesh Creation

The geometry for each flow case was created in ANSYS Workbench. The geometry for each case is created in two dimensions and then extruded in the z direction. The thickness of the extrusion for each case is the same depth as the characteristic length (tube diameter or square side) as the object in cross flow. For the staggered tube this depth is 45mm and for the square it is 30mm. ANSYS Mesh was used to create a paved quadrilateral grid that was extruded in the z-direction to create an all hexahedral mesh. Meshing tools were used to refine the mesh near the wall to ensure that the first cell had a $y+ \sim 1$, well inside the viscous sublayer. The meshes used for the SST, RSM, PANS-SST and SST-SAS solutions as well as their boundary definitions are shown in Figure 4-1 and Figure 4-2. The meshes used for the DES and LES solutions were similar but used finer grids. For the mesh sensitivity study, all the meshes evaluated follow the same general pattern shown here. For the square model, the region downstream of the square was refined to properly capture the vortex shedding in wake region.

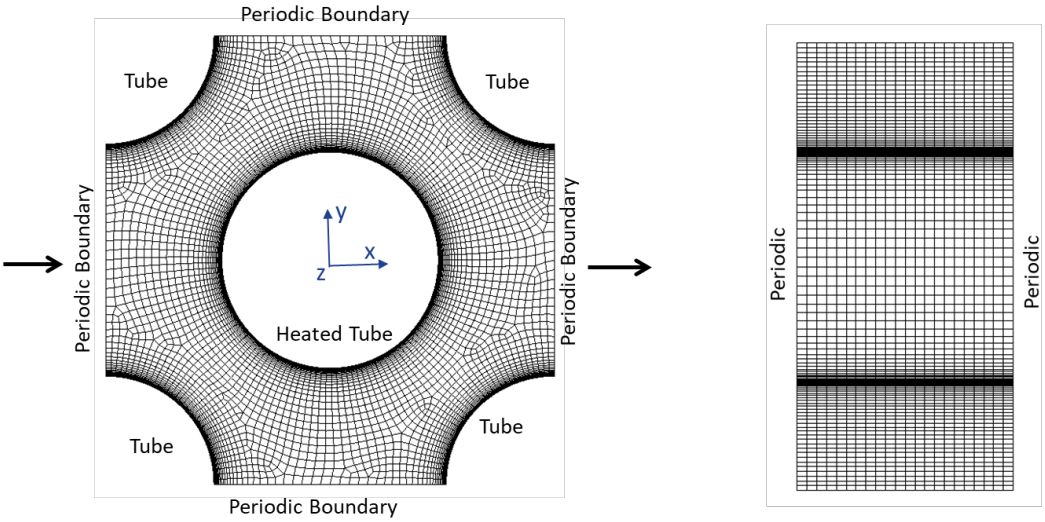

Figure 4-1 Mesh C for staggered tube bank

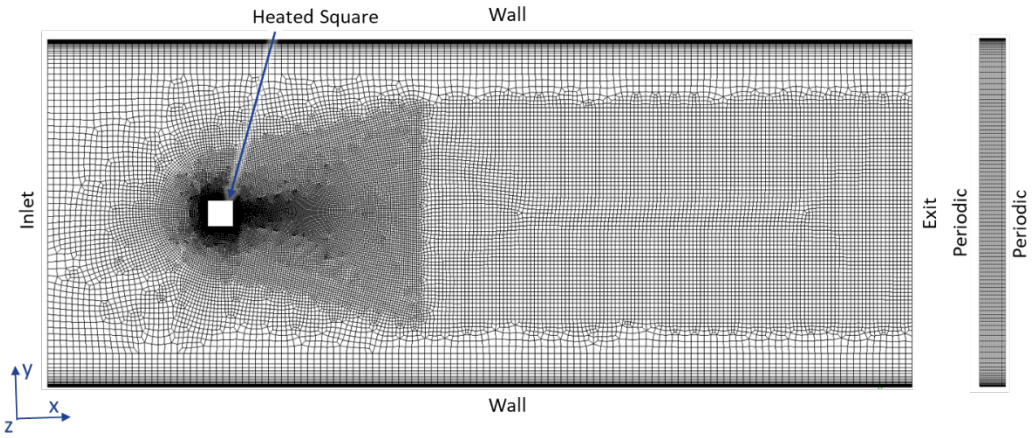

Figure 4-2 Mesh C for square in cross flow

4.2 Problem Configuration

4.2.1 CFD model conditions

The fluid is defined as air with temperature dependent fluid properties (density, viscosity, specific heat and thermal conductivity.) A constant heat flux of 1,000 W/m² K is applied to the surface to emulate the heat generation at the surface. For both cases, a periodic

boundary condition is applied to the surfaces perpendicular to the z-axis. For the staggered tube bank, a fixed mass flow rate of 0.031099 kg/s in the flow x-direction results in the appropriate Reynolds numbers. Similarly, the inlet velocity of 9.7082 m/s for the square in cross flow creates a Reynolds number to match the Igarashi heat transfer data. The inlet temperature for both cases is 300K.

4.2.2 Solution Methods

The solution for this study was performed with ANSYS Fluent v17.1, which is an unstructured finite volume code [48]. The models for RSM, DES and LES used the standard model in the Fluent software. The SST, SST-SAS and SST-PANS models were programed into the software through User Defined Functions (UDF) [87]. The turbulent kinetic energy (k) and the specific dissipation (ω) terms are represented in the software as scalars. This turbulence model is then linked to the remainder of the solution through the turbulent viscosity calculation in a UDF. The source terms and diffusion coefficients for the k and ω equations are provided to the solver via UDFs. The remainder of the solution of the scalar transport equation including discretization is handled by the software. The implementation of the turbulence model in ANSYS Fluent is presented in Appendix A, including a listing of the source code. The solver numerics used in the solution are presented in Table 4-1.

Table 4-1 Solver settings for solution

Scheme/ Spatial discretization	**Model**	**Value**
Pressure Velocity Coupling	All	SIMPLE
Pressure Gradient	All	Second order
Momentum	SST, RSM, PANS-SST	Second order upwind
	SST-SAS, LES and DES	Bounded Central Differencing
Reynolds Stresses	RSM	Second order upwind
Turbulent Kinetic Energy	SST, SST-SAS, SST-PANS, DES	Second order upwind
Specific Dissipation	SST, SST-SAS, SST-PANS, RSM, DES	Second order upwind
Energy	All	Second order upwind
Transient	All	Bounded Second Order Implicit

4.2.3 Transient results

After providing an initial condition based on the inlet fluid velocity, the steady solver is run until the solution residuals stop decreasing monotonically. Because the steady solution is not able to resolve the instability caused by the flow separation for both cases, neither will demonstrate good convergence in this mode. The solution was then switched to transient and restarted with the steady solution used at its initial condition. The time step is manually adjusted for each solution to ensure that Courant-Friedrichs-Lewy (CFL) number was less than 5 in all locations for the URANS solutions and less than 1 for the DES and LES solution.

When starting from a transient solution from a steady state initial condition, there is a start-up time required to reach a physically realistic, unsteady solution. Results from the start up period were not included in the final time averaged results.

4.2.4 Time averaging solution

One of the challenges of this study was to determine the both start up time and the number of time steps required to reach a time invariant solution. Thousands of time steps are run and the data files from these results are post-processed separately. ANSYS Fluent can determine the time averaged value for any parameter from a transient analysis. However, this capability does not directly allow the user to confirm that a true time invariant solution has been reached. It was found to be more reliable to write data files at each time step that could be analyzed by a separate program specifically written for this purpose.

For the calculation of the Nusselt number, the surface temperature for the entire heated surface is written at each time step (or every other time step for the larger meshes and smaller time step solutions.) Likewise, the velocity and other data required to find the Reynolds stress profiles is written to another set of files. The data is then used to calculate the Nusselt number, Reynolds stress, etc., and are averaged over time. In addition, the data is averaged in the z-direction because the time averaged flow is two dimensional and it therefore statistically homogeneous in this direction. The Nusselt number profiles are sub-divided into ten sub-groups and the mean value for each sub-group is reported. These sub-averages are used to determine if time invariance has been achieved.

A sample data set for the mean Nusselt number for the square in cross flow is provided in Figure 4-3 for a case that is not time invariant. Figure 4-3a shows the local Nusselt

number for each sub-average, the final average and the experimental data. The x-axis is the non-dimensional distance from the stagnation point or the center of the front of the square. (Figure 3-7 provides details on the non-dimensional distance relative to the corners on the square.) In Figure 4-3b, the mean Nusselt number by side is plotted relative to the characteristic time, which is defined as the time required for the mean flow to travel the length of the square side. The local Nusselt number is averaged by surface on the square for each of the 10 sub-averages (dashed line) as well as a cumulative average (solid line). This cumulative average can be used to determine if the model has been run long enough by looking at the slope of last few sub-averages.

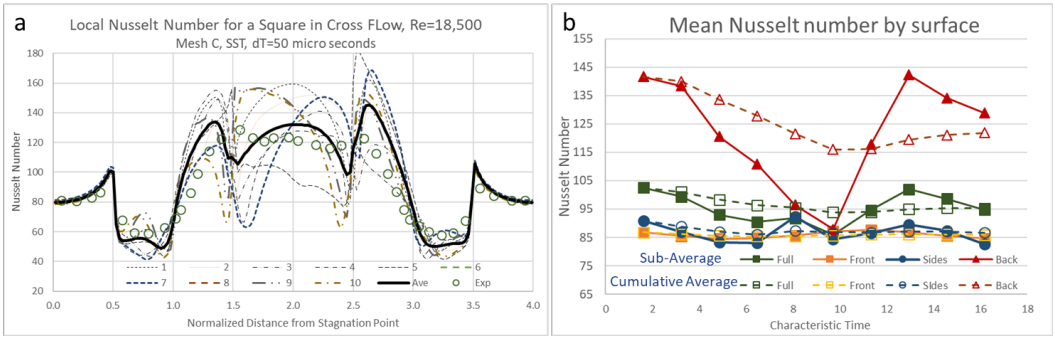

Figure 4-3 Sample time averaging result for square in cross flow with local Nusselt number (a) and averaged by surface (b); incomplete case

The data from this case shows that the model has not been run for a sufficient number of steps to achieve a time invariant solution. These plots also show some interesting features of the solution. The first is that the local Nusselt number in Figure 4-3b exhibits significant variation in the areas where the flow is separated such as the rear, while the area where the flow stays attached on the front of the square shows little to no variance. It was found the rear surface was the last to settle on a time invariant solution.

Figure 4-4 shows the results of the same model for a longer averaging period as a well as a longer delay from the start of averaging. The characteristic time for the duration of the averaging is nearly 350. The sides of the square show very little variation from one sub-average to another. There is a small amount of variation on the rear face which is where the strongest degree of resolved turbulence would be found.

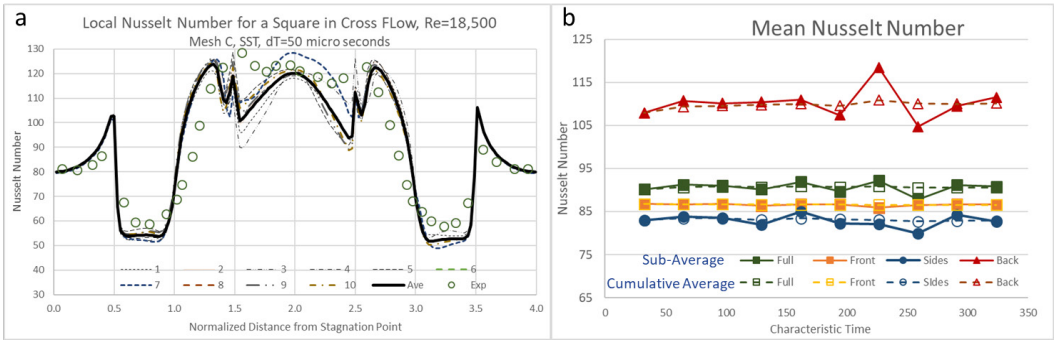

Figure 4-4 Sample time averaging result for square in cross flow with local Nusselt number (a) and averaged by surface (b); completed case

For each model case, this data is carefully evaluated for the following criteria. The final cumulative mean values for each side cannot change by more than ~1.0% than from the previous mean. In addition, the values from the first one or two sub-averages is checked to make sure that they are generally in line with the remaining data. This ensures that time averaging is not started too soon after the transient solution began to show non-physical artifacts of the transition from steady state to transient.

The different turbulence models were not run for the same characteristic time because the time required to reach a time invariant solution was not the same for each model. In general, turbulence models that resolved more of the turbulence required longer run times, while simulations where more turbulence was unresolved required less. This is

because the solutions that resolved more turbulence experienced more random fluid motions that required more time to reach stable averages.

The velocity and Reynolds Stress profiles are calculated with the same start and end time as the average Nusselt number.

4.3 Mesh Independence

Multiple meshes were created for each flow problem to ensure mesh independent results. The meshes were set up to roughly double in cell count for each successive refinement and all had the same general appearance as those shown in in Figure 4-1 and Figure 4-2. A summary of the meshes used for the mesh independence study and their cell count is provided in Table 4-2 The meshes shown in Figure 4-1 and Figure 4-2 are for Mesh C in this table. All of the meshes maintained a sufficiently small first cell size to achieve y+~1.

Table 4-2 Meshes used for CFD analysis

Mesh	Staggered tube bank	Square in cross flow
A	73,570	268,755
B	127,566	394,763
C	186,340	1,036,800
D	332,021	1,600,320
E	476,820	2,996,452
F	1,850,760	4,849,152
G	2,335,500	

The analysis was run for the three standard URANS models; SST, SST-SAS and RSM for each mesh, starting with mesh A. The mean Nusselt number for each mesh is compared on a relative basis to ensure mesh independence. These results are shown in and Figure 4-5 for the staggered tube bank and Figure 4-6 for the square in cross flow.

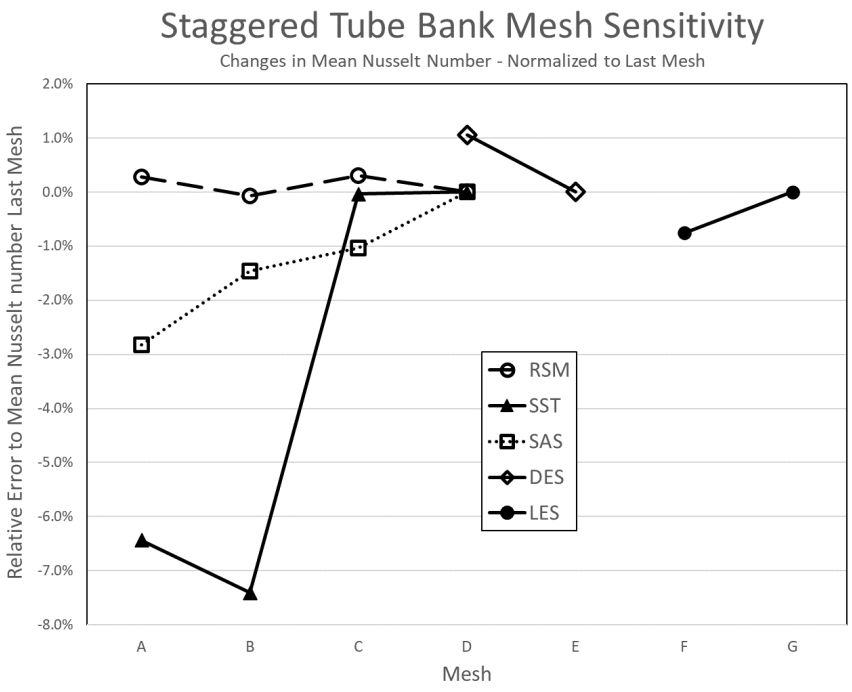

Figure 4-5 Staggered tube bank mesh sensitivity study

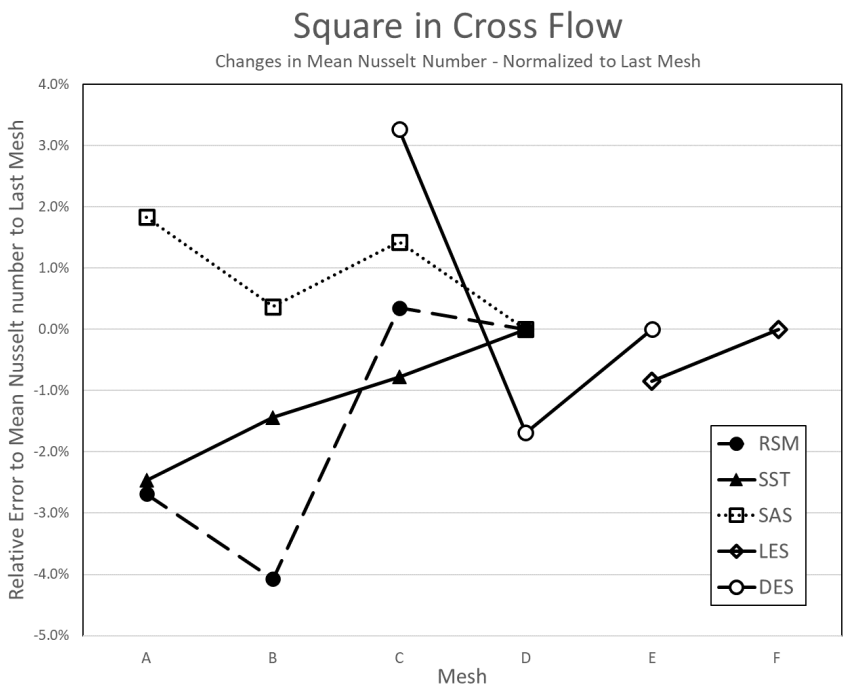

Figure 4-6 Square in cross flow mesh sensitivity study

The results show that Mesh C is sufficiently fine for both cases because the variation to the next level of mesh refinement is small mesh independence is confirmed. Since the PANS-SST is a variant of the SST model, Mesh C was also used for these simulations to demonstrate the benefits of the improved model.

For the DES model of the staggered tube bank, Mesh E showed only a 1% improvement relative to Mesh D, so Mesh D was chosen. Likewise, for the LES model, Mesh F only showed less than a 1% change from Mesh G. For the DES model for the square, the normalized results for meshes C, D and E relative to the results of mesh E are shown in Figure 4-6. The DES model has an explicit mesh dependence in its formulation and a truly mesh independent solution is not necessarily possible. However, the results in this figure show that mesh D is sufficient. Finally, Mesh E for the square was used for the

LES model with this geometry. The LES formulation is also dependent on the local mesh (filter) size but these results show little variance from Mesh E to F

4.4 Calculating Reynolds Stresses

The Reynolds stresses from the CFD solutions are a summation of the unresolved (modeled) and resolved components as shown in Equation (47). The unresolved Reynolds stress is found from the Boussinesq hypothesis as shown in Equation (48) and is calculated from the modeled turbulent kinetic energy, the turbulent viscosity and the strain rate. The resolved turbulence is calculated from the flow transients and the mean velocity as shown in Equation (49).

$$\overline{u'_i u'_j}_{total} = \overline{u'_i u'_j}_u + \overline{u'_i u'_j}_r \tag{47}$$

$$\overline{u'_i u'_j}_u = \frac{2}{3} k \delta_{ij} - \nu_t \left(\frac{\partial u_i}{\partial x_j} + \frac{\partial u_j}{\partial x_i} \right) \tag{48}$$

$$\overline{u'_i u'_j}_r = \overline{(\overline{u_i} - u'_i)(\overline{u_j} - u'_j)} = \overline{u_i u_j} - \overline{u_i}\,\overline{u_j} \tag{49}$$

Equation (49) is derived from the standard Reynolds decomposition ($u_i = \bar{u} + u'$) and can also be called a two-part Reynolds decomposition. An alternate approach is to employ a three-part Reynolds decomposition that also includes a separate term for a phase averaged coherent velocity term with a mean of 0 as shown in Equation (50)

$$u_i = \bar{u} + \tilde{u} + u' \tag{50}$$

In turbulent flows where there is a coherent periodic flow component like that found in a von Karman vortex sheet, the three-part decomposition can be used. This serves to separate the impact of coherent, large scale velocity fluctuations [88] from the Reynolds stress calculation. While vortex shedding is found both cases, the experimental data for the Reynolds stresses for the staggered tube bank used the two-part decomposition. The three component decomposition was used for the square in cross flow [80], but only for the velocity component in the streamwise direction (u) to be consistent with the experimental data. Applying a time average to Equation (50) and solving for the Reynolds stress results in Equation (51).

$$\overline{u_i' u_i'} = \overline{u_i u_i} - \overline{\tilde{u}_i \tilde{u}_i} - \bar{u}_i \bar{u}_i \tag{52}$$

The Reynolds stress in direction perpendicular to the streamwise flow is calculated by Equation (49).

This approach was used for the SST, SAS, PANS-SST, and DDES models. For the RSM model, the unresolved Reynolds stresses from the model were used directly, rather than equation (48). For the LES solution, the unresolved turbulent kinetic energy is zero and the sub grid viscosity is used with equation (48) to calculate the Reynolds stresses.

5 RESULTS OF COMPARITIVE STUDY

The results of both geometric cases for this study are discussed separately and the final conclusions will be discussed together in the final section. For both cases, the SRANS SST model results are included for reference. Initially, the steady SST solution for the staggered tube bank and square in crossflow was run for the same mesh as the unsteady case. However, neither case was able to converge properly due to flow instability. Consequently, the model was cut in half along the center of the tube or square in the flow direction and a symmetry boundary is applied. (An equivalent Mesh C was used for this purpose.) This change prevents the buckling of the flow down-stream of the bluff body and facilitates a numerically stable solution. In this configuration, the square converged very well while the staggered tube bank continued to show difficulty converging. Nonetheless, the results provide a reference to compare to the unsteady models.

5.1 Staggered tube bank

In the confined space of the tube bank, the von Karman vortex sheet is not able to develop as typically found in bluff body flows. Vortices are created from alternating sides of the tubes but a coherent vortex that is the same size of the tube does not propagate downstream. Rather, and the flow downstream of the tube sweeps from one side to the other due to the instability created by the upstream tube. As a result, the location of the upstream stagnation point, as well as the point where the reverse flow impinges on the rear of the tube, oscillates. An example from the PANS-SST solution is

shown in Figure 5-1. The instantaneous streamline plot is shown in Figure 5-1a and the time averaged streamlines are shown in Figure 5-1b. The later shows where the time averaged separation point occurs as well as the size of recirculation bubble. The stream line plots provide a qualitative information of the flow patterns in this model and will aid in interpreting the results of the CFD models.

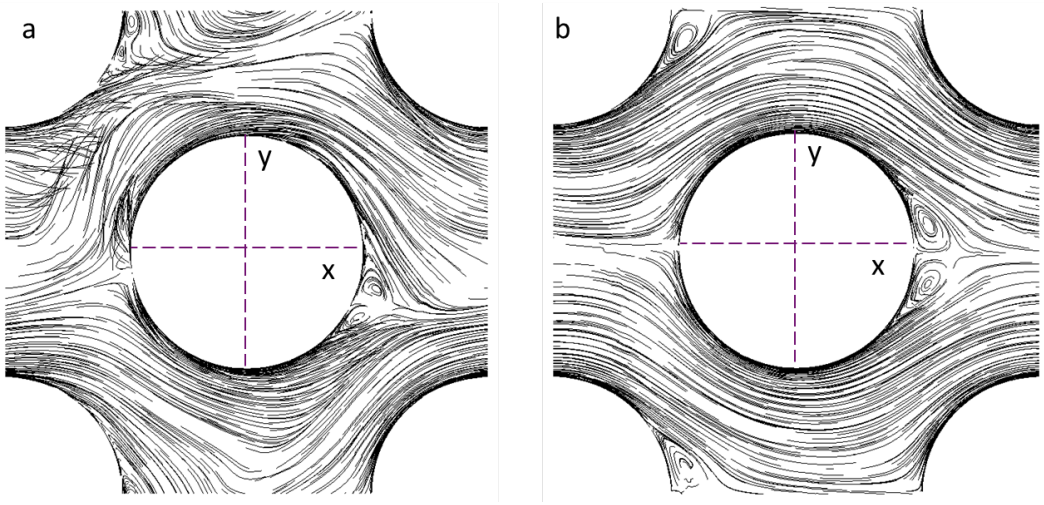

Figure 5-1 Instantaneous (a) and time averaged (b) flow path lines for PANS-SST solution for staggered tube bank

The local Nusselt number data from the experimental data [68] and the six models used in this study are shown in Figure 5-2 and in Table 5-1. The results from an SRANS SST solution is also presented in this figure and table.

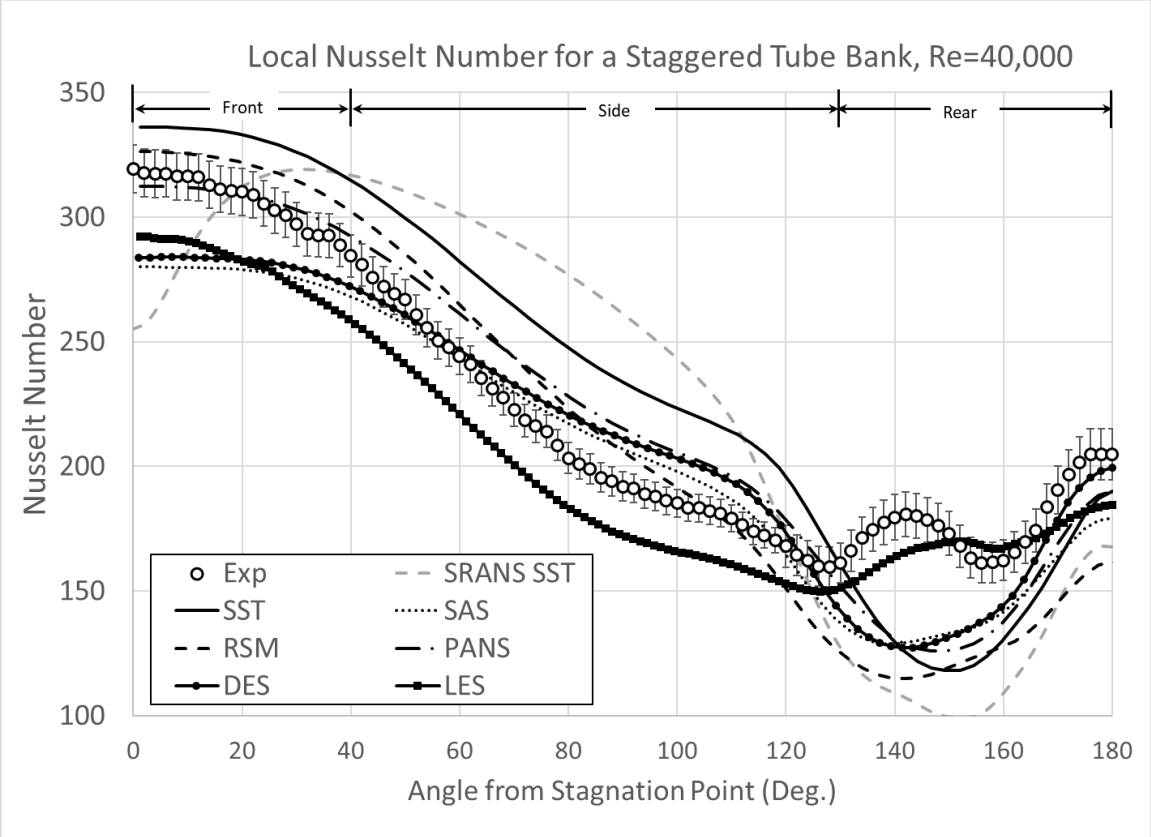

Figure 5-2 Local Nusselt Number, staggered tube bank, Re=40,000

All the unsteady models are a significant improvement over the SRANS SST results relative to the overall shape of the local Nusselt number profile. While the overall mean Nusselt number for SRANS-SST (228.2) is approximately the same as URANS version (234.9), the local accuracy of the URANS SST model is a significant improvement over the SRANS version. This is shown in both the local distribution of the Nusselt number as well as the averaged values by sections of the tube.

Table 5-1 Mean and local results for staggered tube bank Nusselt number

Model	Mean Nusselt number				Mean Nusselt number error			
	All	Front	Sides	Back	All	Front	Sides	Back
Exp	222.4	306.3	207.5	178.8	+/-3%	+/-3%	+/-3%	+/-5%
SRANS SST	228.2	300.0	253.4	122.5	2.6%	-2.1%	22.1%	-31.5%
SST	234.9	330.1	243.6	143.5	5.6%	7.8%	17.4%	-20%
SAS	207.6	277.1	211.1	145.7	-6.7%	-9.5%	1.7%	-19%
RSM	215.3	319.0	216.2	130.7	-3.2%	4.1%	4.2%	-27%
PANS	221.5	306.6	224.8	147.6	-0.4%	0.1%	8.3%	-18%
DES	212.5	281.1	216.2	151.1	-4.5%	-8.2%	4.2%	-16%
LES	203.3	280.1	188.9	169.1	-8.6%	-8.6%	-9.0%	-5.4%

The u- and v-velocity profiles along with the normalized Reynolds stress profiles for the locations shown in Figure 3-2 are provided in Figure 5-3 through Figure 5-6. The experimental data [69]is also included in these figures. The effective thermal conductivity is plotted for same locations as the data and can be used to interpret the heat transfer results. Because the effective thermal conductivity is calculated from the turbulent viscosity (Equation (13)), it can also provide an indication of the degree of modeled turbulence. A higher level of effectively thermal conductivity indicates a higher level of modeled turbulence while a value closer to the molecular thermal conductivity indicates that the turbulence is mostly resolved. The local convective heat transfer from the surface can be described by the equation

$$q" = h(T_s - T_\infty) = k_{eff}\frac{\partial T_f}{\partial n} \tag{53}$$

In this equation, k_{eff} is the effective thermal conductivity of the fluid at the surface and $\frac{\partial T_f}{\partial n}$ is the temperature gradient in the fluid. In a turbulent solution where the turbulent viscosity is zero at the surface, the effective thermal conductivity of the fluid is simply the molecular thermal conductivity. The enhanced heat transfer in a turbulent flow is manifested by the increased temperature gradient at the surface. This steeper gradient is either due to the higher effective thermal conductivity of the fluid or a higher fluid velocity impinging on the surface. The former can be due to a higher degree of unresolved turbulence while the later can be due to a higher degree of resolved turbulence. These two effects in tandem control the local Nusselt number result.

The degree of modeled turbulence can also be directly viewed for each model as shown in Figure 5-9. Here the time averaged percentage of resolved-to-total turbulent kinetic energy is presented at the y/D=0 plane, downstream of the tube. The contour plots in Figure 5-7 shows this instantaneous vorticity magnitude ($\Omega = \sqrt{2\Omega_{ij}\Omega_{ij}}$, $\Omega_{ij} = \partial u_i/\partial u_j - \partial u_j/\partial u_i$) for the six models. The LES results show a very high degree of resolved turbulence as manifested by small concentrations of high vorticity magnitude evenly distributed throughout the flow space. The other solutions show that the fluid rotation is more limited to the vortex created at the point of flow separation. Finally, contour plots of the instantaneous turbulent viscosity ratio (μ_t/μ) at an arbitrarily chosen time step also aides in visualizing the degree and nature of turbulence modeling for each model.

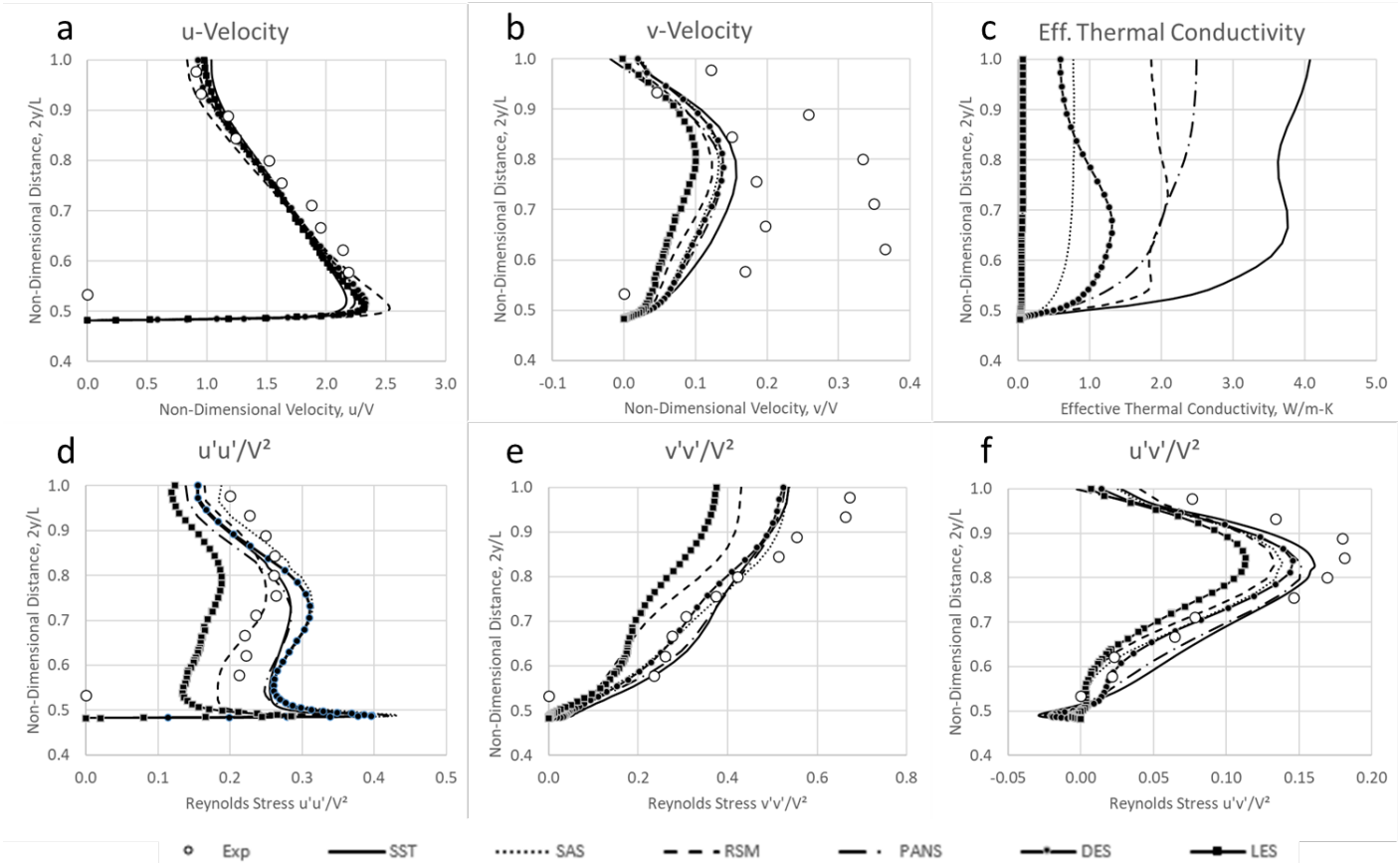

Figure 5-3 Staggered tube bank profiles, 2x/L=0.0, Re=40,000; u-velocity (a), v-velocity (b), effective thermal conductivity (c), normalized Reynolds stress $\overline{u'u'}$/V² (d), $\overline{v'v'}$/V² (e), and $\overline{u'v'}$/V² (f)

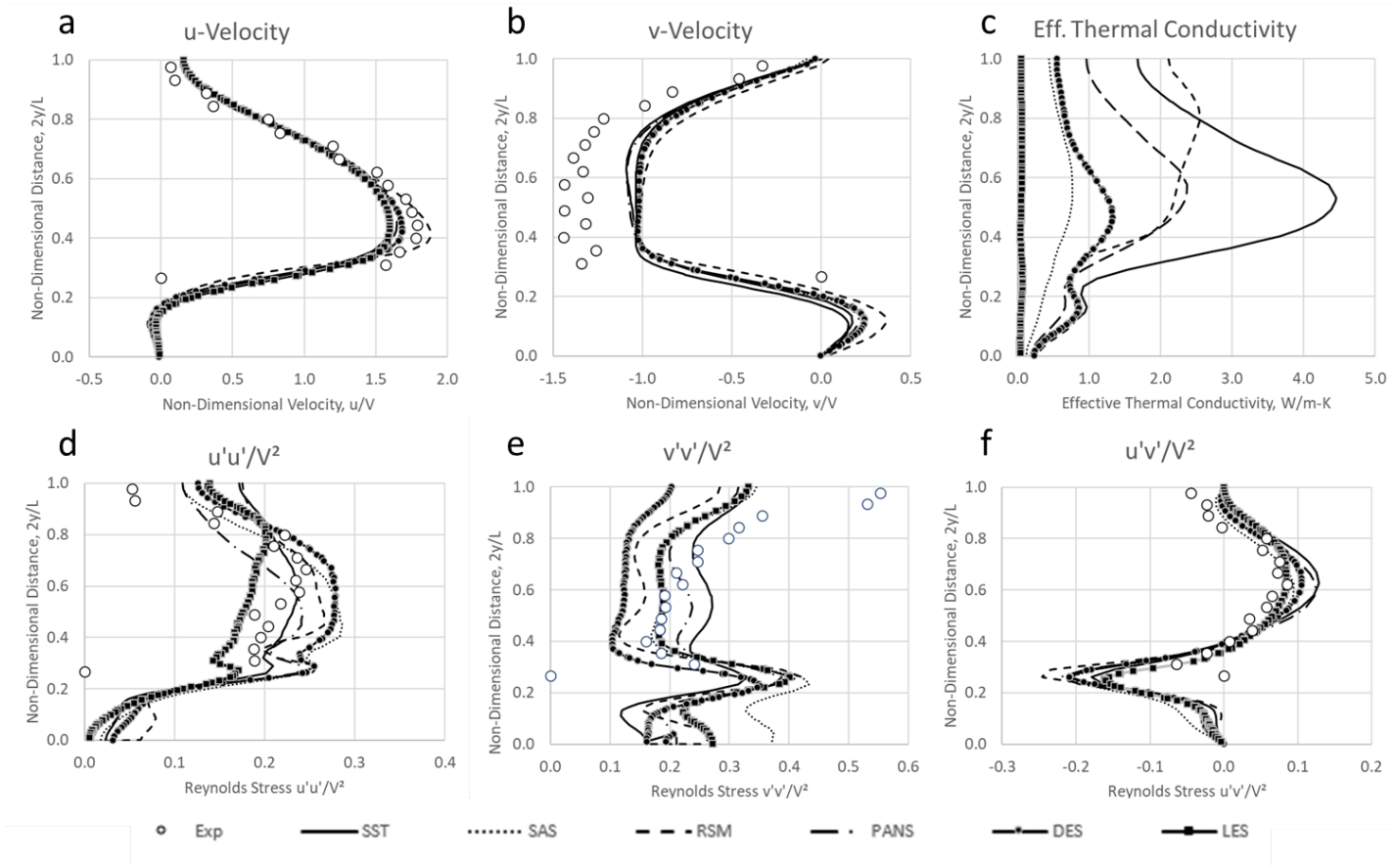

Figure 5-4 Staggered tube bank profiles, x/D=0.507, Re=40,000; u-velocity (a), v-velocity (b), effective thermal conductivity (c), normalized Reynolds stress $\overline{u'u'}/V^2$ (d), $\overline{v'v'}/V^2$ (e), and $\overline{u'v'}/V^2$ (f)

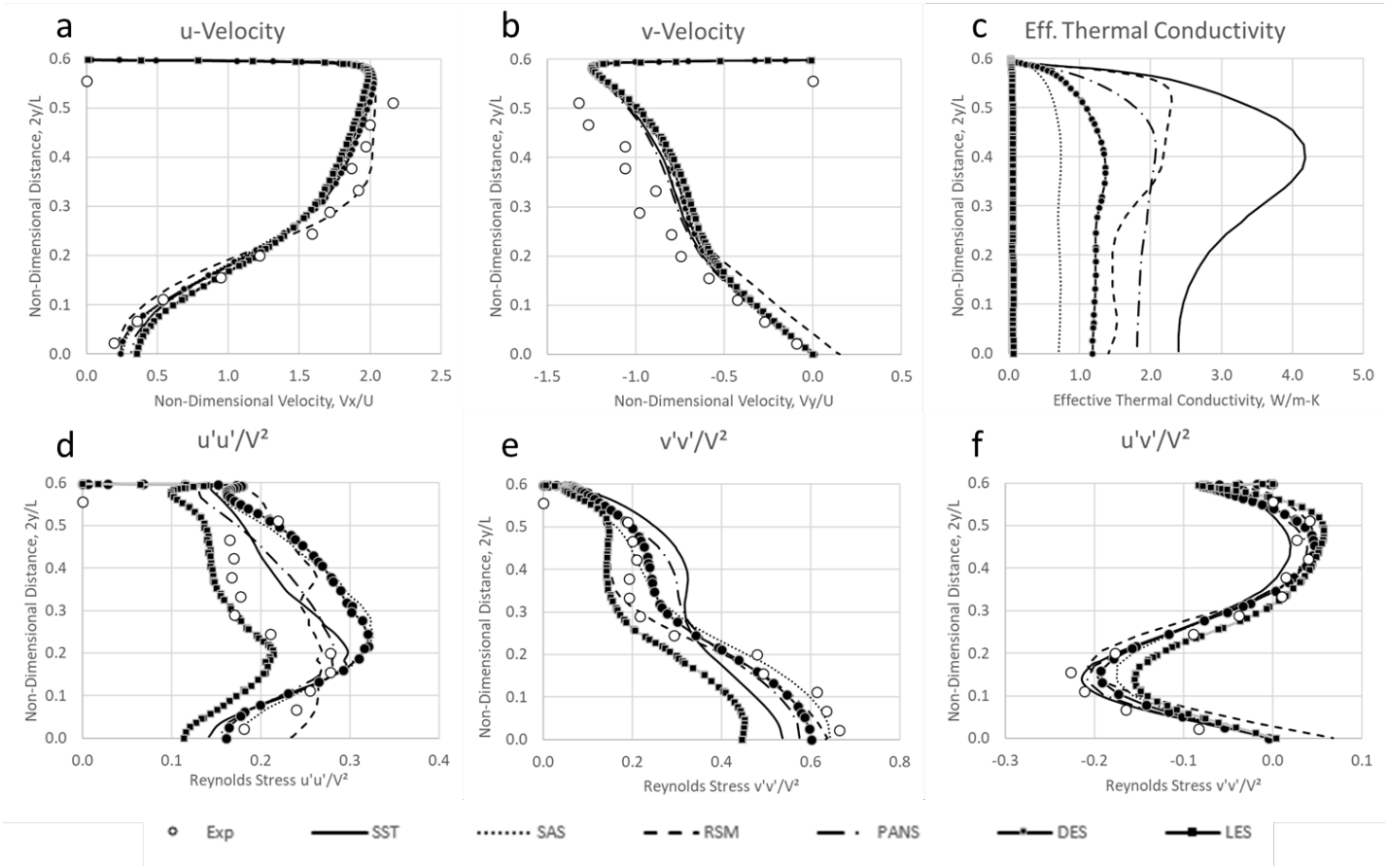

Figure 5-5 Staggered tube bank profiles, 2x/L=0.733, Re=40,000; u-velocity (a), v-velocity (b), effective thermal conductivity (c), normalized Reynolds stress $\overline{u'u'}/V^2$ (d), $\overline{v'v'}/V^2$ (e), and $\overline{u'v'}/V^2$ (f)

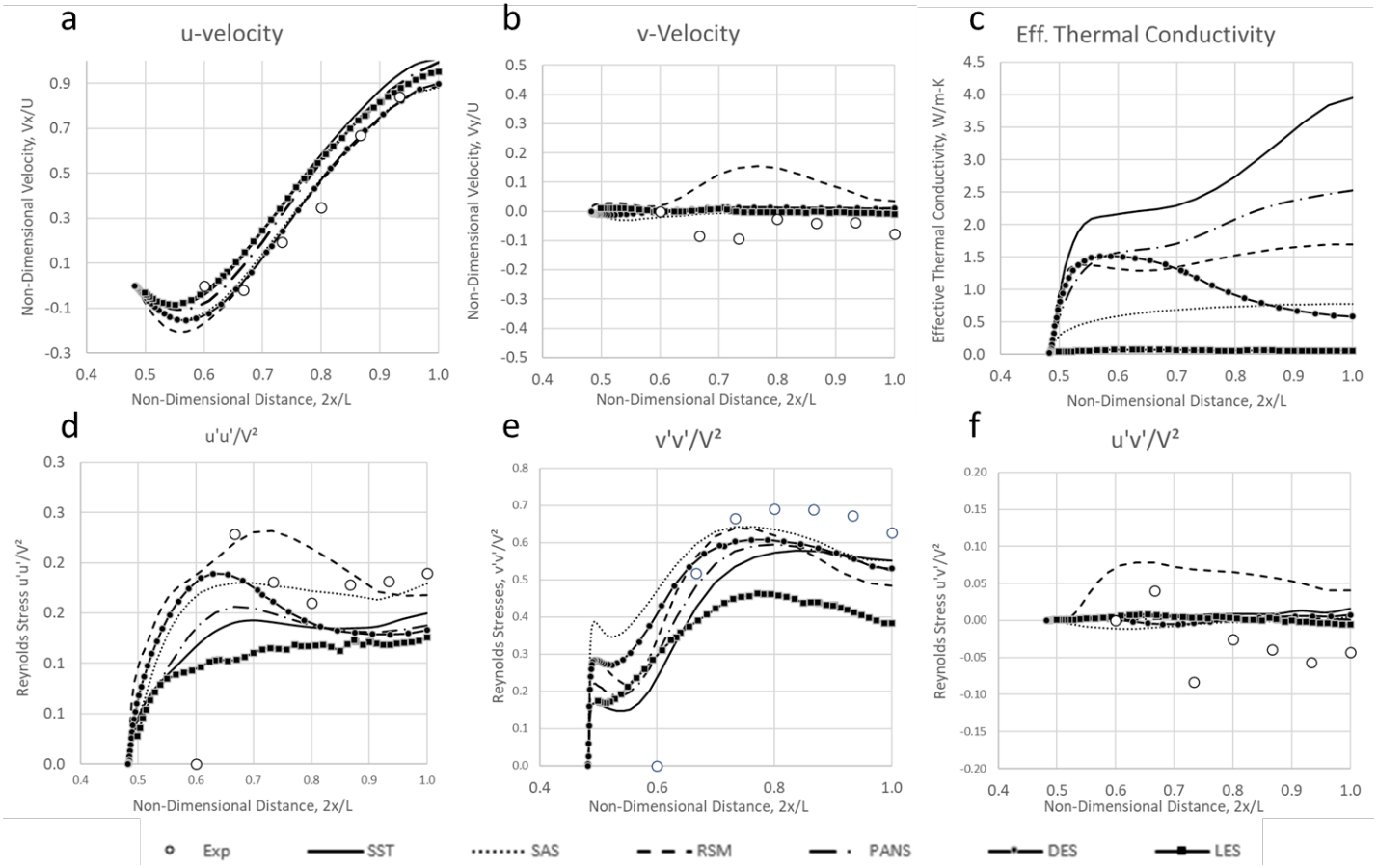

Figure 5-6 Staggered tube bank profiles, 2y/L=0.0, Re=40,000; u-velocity (a), v-velocity (b), effective thermal conductivity (c), normalized Reynolds stress $\overline{u'u'}/V^2$ (d), $\overline{v'v'}/V^2$ (e), and $\overline{u'v'}/V^2$ (f)

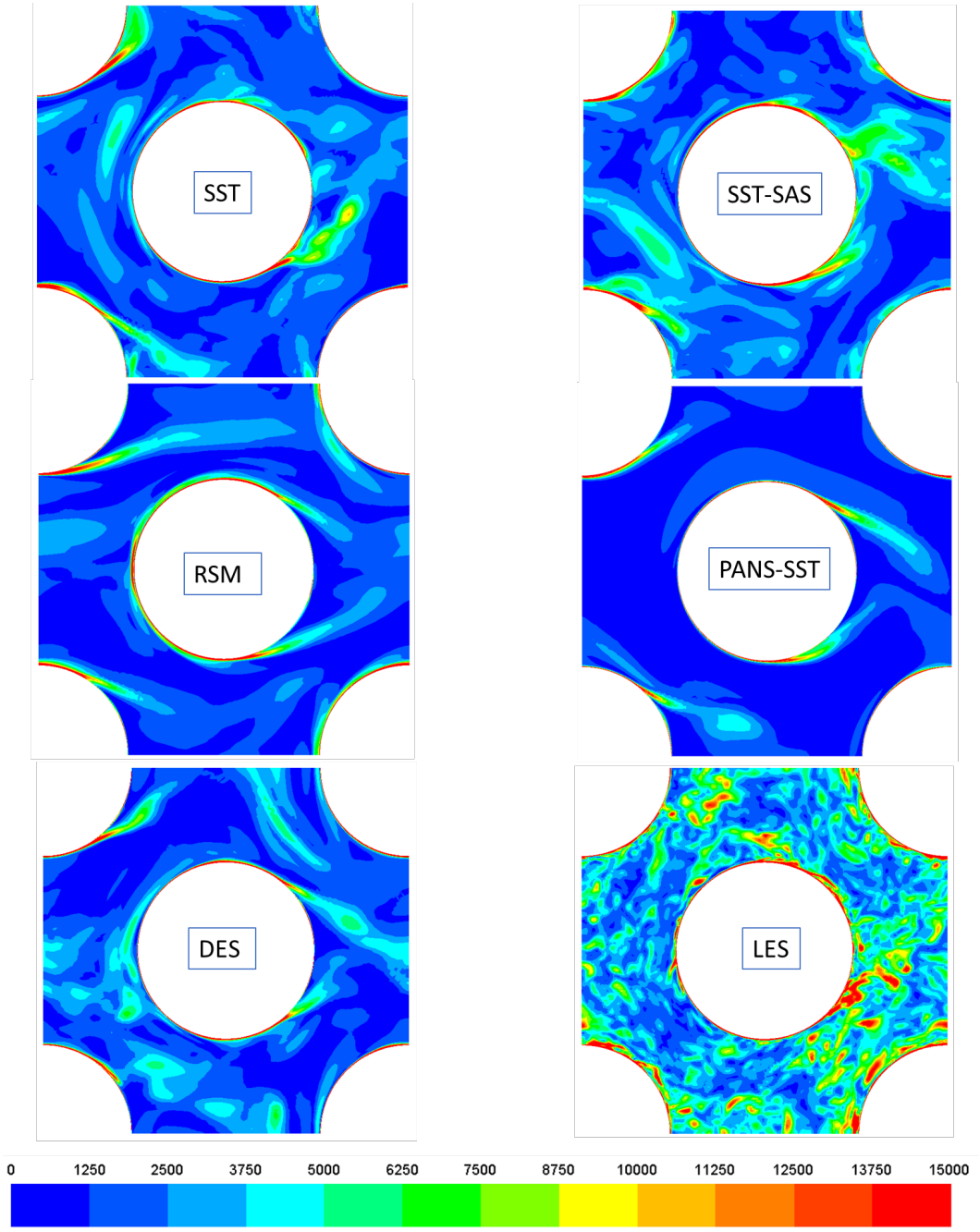

Figure 5-7 Vorticity magnitude for the staggered tube bank for the six models

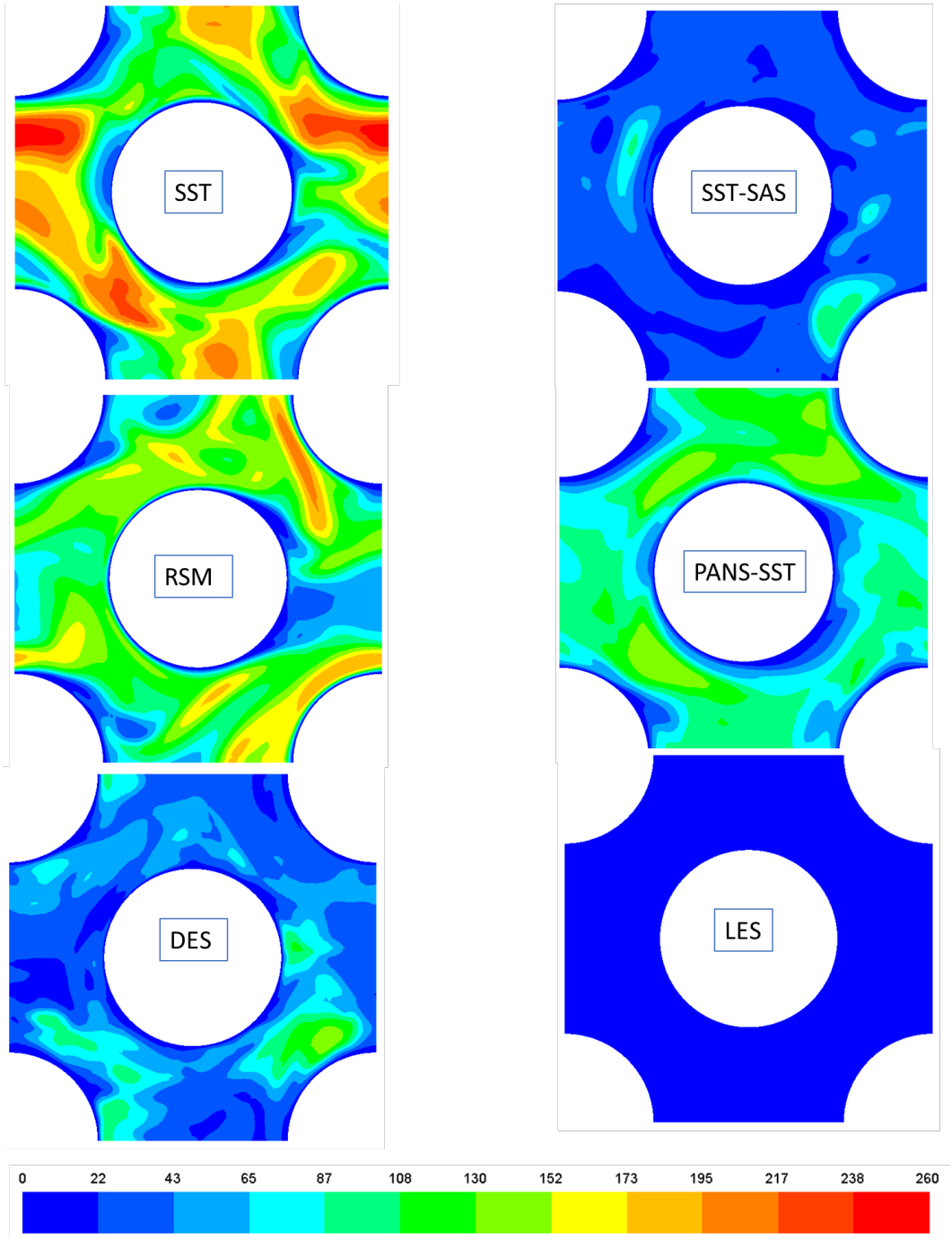

Figure 5-8 Instantaneous turbulent viscosity ratio (turbulent viscosity/ molecular viscosity) for staggered tube bank for the size models

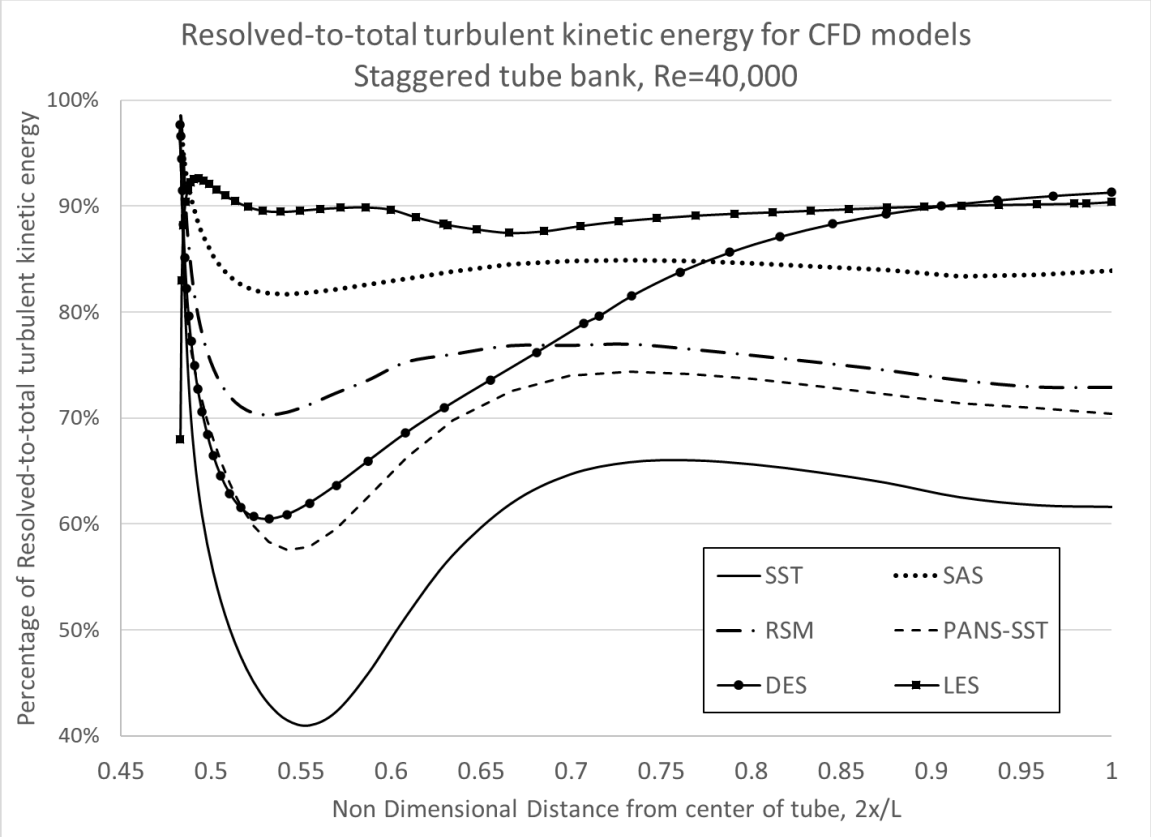

Figure 5-9 Ratio of resolved-to-total turbulence for the staggered tube bank y=0, downstream of the tube

Experimental data is not available in the literature for Strouhal numbers or drag and lift coefficients for this configuration. However, this data is compiled for the six models for comparative purposes in Table 5-2 to future researchers. This table also includes the normalized size of the recirculation bubble, l_R, behind the tube. This value is measured from the center of the tube to the point behind the tube where the time averaged u-velocity is zero. The normalizing factor is 2x/L where L is twice the spacing between tubes in the lateral (flow) direction. Because the experimental velocity profile in this area does not clearly show where the zero velocity occurs, it is not appropriate to claim a specific experimental value from this data.

Table 5-2 Drag, Lift and Strouhal number for staggered tube bank

Model	C_d	C_d'	C_l'	St	l_R
SST	1.172	1.562	1.271	0.722	0.619
SST-SAS	1.273	0.316	1.431	0.662	0.654
RSM	1.310	0.369	1.841	0.688	0.663
PANS-SST	1.229	0.321	1.479	0.733	0.637
DES	1.184	0.248	1.431	0.704	0.661
LES	0.979	0.193	0.846	0.711	0.614

5.1.1 Assessment frequency domain analysis and degree or resolved turbulence for the staggered tube bank

The frequency domain of the velocity traces taken at a point downstream of the tube for each model are provided in Figure 5-10. The coordinate for this point is x/D=0.733 and y/D=0. The results show the dominate vortex shedding frequency created in the wake of the tube as well as the relative level of the other turbulent scales. The magnitude of the spike for the shedding frequency relative to the magnitudes for the other frequencies indicates the level of resolved turbulence other than the dominant shedding frequency.

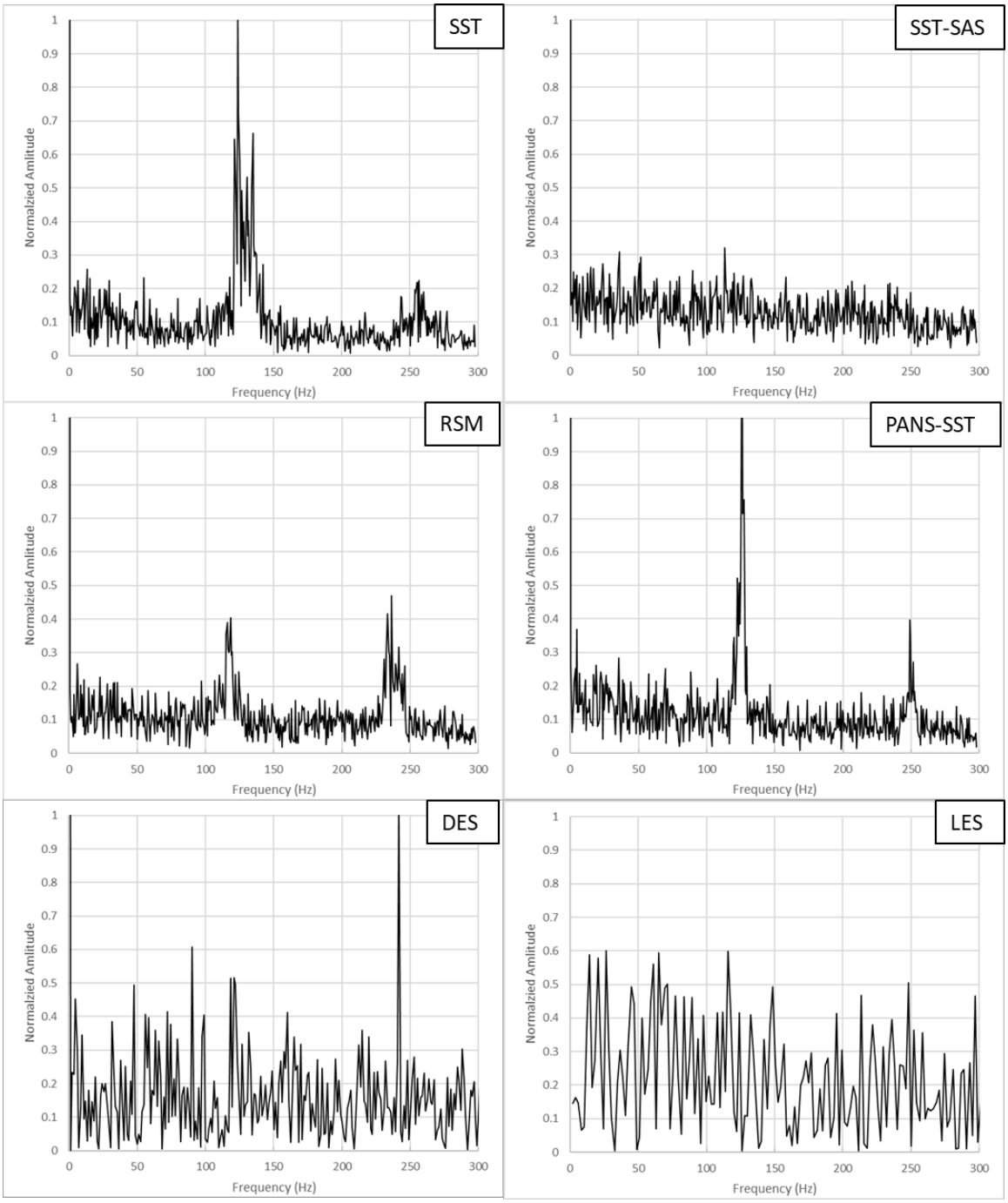

Figure 5-10 Frequency domain analysis of velocity trace from CFD models for staggered tube bank

The results for the SST model show a high relative amplitude at and near the vortex shedding frequency and is much smaller elsewhere. This result is expected for a URANS model that does not include any scale resolving capability, i.e. only the dominant turbulent scales are resolved. This model also showed the lowest percentage of resolved turbulence than the other models as show in Figure 5-9. The SST-SAS model shows that while a dominate shedding frequency can be found at 114 Hz the relative amplitude of the other frequencies is only slightly lower, confirming the increase in resolved scale relative to the SST model. This is also evidenced in the significant reduction in the profiles of the effective thermal conductivity values shown in Figure 5-3c to Figure 5-6c as well as the increased percentage of resolved scales in Figure 5-9. In addition, this figure shows that the percentage of resolved scales is much higher than the baseline SST model.

For the PANS-SST model, the PANS modification results in a degree of resolved scales that is higher than the base SST model but is less than that found with the SST-SAS model. This is indicated by the ratio of resolved-to-total turbulence shown in Figure 5-9 that is below the SST-SAS result. The frequency domain analysis for the PANS-SST model is not significantly different for the SST result, indicating a similar size of the resolved length scales. With the Reynolds Stress model, the dominant shedding frequency is evident but the peaks are smaller relative to other the frequencies. The percentage of resolved turbulence is approximately the same as the PANS-SST method. The DES results show a very strong response at the shedding frequency despite the high

degree of resolved turbulence at this point (~75%). Finally, the LES model shows a peak at the shedding frequency but it is not substantially larger than the response at other frequencies. As expected, the LES model showed the largest degree of resolve-to-total turbulence with an average value at approximately 90%. This results also shows that the this simulation meets the minimum recommended level of resolved turbulence [8]

5.1.2 Heat transfer and flow profiles for the staggered tube bank

5.1.2.1 SST Model

The SST model generally over predicts the heat transfer, particularly near the stagnation point as well as along the sides of the tube. The overall mean Nusselt number was 234.9 relative to an experimental value of 222.4. On the front and side portions of the tube, the SST model overpredicts the experimental data +7.8% and +17.4% respectively. On the rear portion (> 130°) of the tube, the model underpredicts the experimental data. (This is true for all of the models except for LES.) In the rear portion the mean Nusselt number is 143.5 relative to an experimental value of 178.8. With the experimental data there is a local rise in the Nusselt number between 130° and 150° that is due to a small eddy very near the wall in this location. The SST model fails to capture this result but does capture the increase in heat transfer at the rear most portion of the geometry where the reversed flow impinges on the back of the tube.

SST model had the smallest recirculation bubble of all the models, indicating the lowest degree of impinging flow on the rear surface of the tube. While this could lead to a lower

Nusselt number, the high effective thermal conductivity of the fluid behind the tube enables better heat transfer as previously discussed.

5.1.2.2 SST-SAS Model

The SST-SAS model is expected to improve on the accuracy of the SST model for this case because the flow field is dominated by non-homogeneous turbulence. This is expected to activate the Q_{SAS} term for this model as shown in Equation (25). As a result, the model should resolve smaller scales throughout the flow field and improve the accuracy relative to the baseline SST model. However, the accuracy of the Nusselt numbers are lower than those found for the SST case with the overall accuracy dropping from a +5.6 to -6.7%. The loss in accuracy is mainly at the front of the tube. The SST model overpredicted the Nusselt number for the front region by 7.8% while the SST-SAS model underpredicted it by 9.5%. Along the sides of the tube, the accuracy is much improved with this model and the Nusselt number values are nearly within the error bars of the experimental data. In the rear portion, the SST and SST-SAS models show essentially the same result. The percentage of resolved turbulence is never lower than 82% for the SST-SAS model while the SST model is on the order of 20 percentage points lower. The higher degree of resolved turbulence is also manifested in the lower effective thermal conductivity for all profiles. One conclusion from this analysis is that an increase in the level of resolved turbulence does not directly translate to an improvement in accuracy.

One issue with the SST-SAS model in its present embodiment is that it is tuned for higher Reynolds number and does not appear to be well calibrated for this case [10, 11]. Improvements to this model will be presented in the next section to address this overcorrection at the stagnation point.

5.1.2.3 Reynolds Stress model

The Reynolds Stress model provides a very good match, only slightly over predicting the local Nusselt number from the stagnation point to the 110°. Slightly after that a similar under prediction is found in the rear section of the tube and the heat transfer results of local eddy centered at 140° is not captured. The velocity and Reynolds stress profiles matched well with the experimental data. Overall, the model was effective at matching the data but the number of times steps to reach a time invariant average was much longer than the of SST models. The SST and the SST-SAS models required runs lasting 180 in characteristic time and the PANS-SST model required a characteristic time of 275. In contrast the Reynolds Stress model was nearly double that at over 500. The increased time required to reach a time invariant result would presumably be due to the increased randomness in the instantaneous local heat transfer caused by higher levels of resolved turbulence. This was not found to be the case however. The Reynolds Stress model had the longest characteristic time but did not have the highest percentage of resolved-to-total turbulence. The anisotropic nature of the Reynolds Stress model may account for this apparent increase temporal variation in local heat transfer.

5.1.2.4 PANS-SST

The PANS-SST solution showed a marked improvement in the local Nusselt number over the baseline SST model and the simulation matches the profile of the local Nusselt number very well. The mean Nusselt number improved 5.6% to less than 1%. The largest improvement was for the front and sides of the tube where the error was reduced from 7.8% to 0.1% and 17.4% to 8.3% respectively. The changes to the rear facing portions were less significant.

This improvement came at a cost however of 2.9 times the computational cost. This is because more computation time is required to determine a mature f_k field. As presented in Section 2.2.4 the updates of the f_k value is required because the total turbulent kinetic energy must be determined by the solution itself so an iterative approach is required. To accelerate the process, the preliminary calculations do not need to be run to the same characteristic time however since converging on the final f_k field is the primary goal. Seven updates were required to reach the a stable f_k field, the final of which is shown in Figure 5-11.

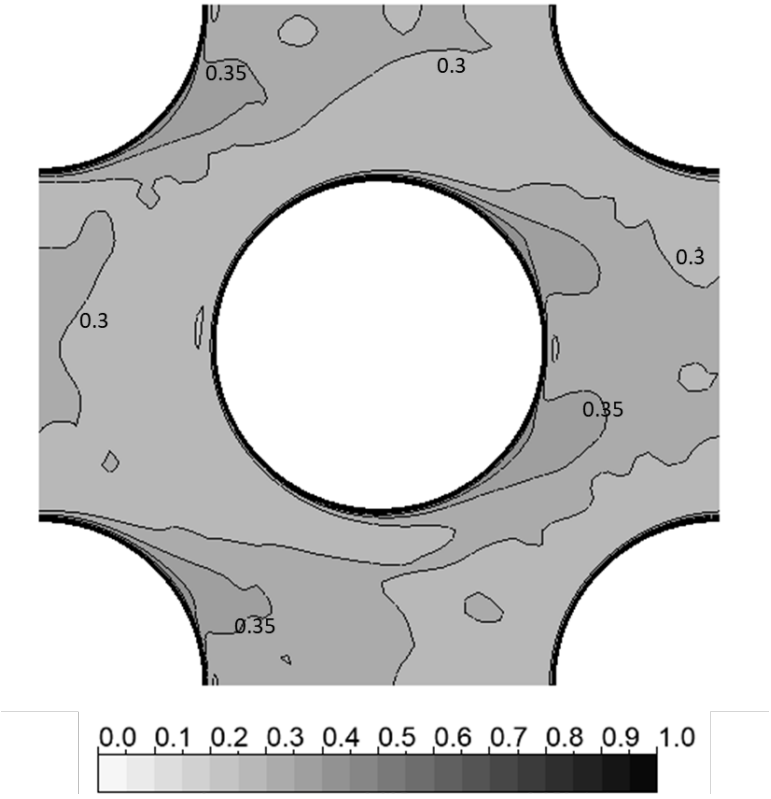

Figure 5-11 Final ratio of unresolved-to-total turbulent kinetic energy, fk, field for PANS-SST solution for the staggered tube bank

The ratio of unresolved-to-total turbulent kinetic energy is mainly in the range of 0.3 to 0.4. This result correlates well to the downstream profile of the percentage resolved-to-total turbulence kinetic energy shown in Figure 5-9 that is around 0.6 to 0.7. The match of the velocity and Reynolds stress profiles do not deviate dramatically from the baseline SST model but are a little closer toward the LES and DES models.

5.1.2.5 DES

The local Nusselt number for the DES solution was below the experimental value at the stagnation point as well as the previously mentioned bump at centered at 140°. The predicted value at the front of the tube was 281.1 relative to the experimental value of

306.3, an error of -8.2%. The back portion of the tube was under predicted by 16%, mostly because it did not capture near wall eddy at 140°.

The DES model showed a lower degree of resolved turbulent kinetic energy closer to the wall as shown in Figure 5-9. Because more of the turbulence is modeled in this area, a modest decrease in the turbulent Prandtl number may improve the accuracy of the Nusselt number predictions.

This model was run with mesh D (see Table 4-2). The DES model required smaller time steps than the other URANS models as the CFL number was kept near or below one to be consistent with the recommendations for this model [58]. The resulting time step was 25μs relative to 100μs for the URANS model and it would be expected that the required characteristic time would be at least as long, if not longer than the other models. This was not the case however as time invariant mean values were found with a characteristic time of less than 60. The summary of the ten averages used to achieve the final average, as shown in Figure B.10, indicates that the analysis has been run for enough time steps.

5.1.2.6 LES

The LES model showed a very good overall match to the local Nusselt number but with a small underprediction. Of the six models evaluated in this study, the LES model provided the most accurate prediction at the rear of the tube and it was able to capture the shape of the profile in this area. The mean value from the CFD prediction was only -9.1% below the experimental data. Because the low level of unresolved turbulence, any

adjustment to the turbulent Prandtl number found from the sub-grid viscosity would not benefit the Nusselt number results.

The drag coefficient for the LES model was noticeably smaller than the other models with a value of 0.979 while the five other models reported a value over one. Additionally, the size of the recirculation zone is smaller than the other models at 0.614. The next largest l_R value is 0.619 for the SST model while the largest of the models was 0.663 for RSM. As stated previously, the experimental velocity profile at the rear of the tube (Figure 5-6a) does not provide sufficient detail to identify the size of the recirculation bubble. However, review the u-velocity experimental data in this chart does show that the LES results are generally shifted higher than the experimental data. Despite this discrepancy, the local Nusselt number on the rear portion of the tube showed a very good match with a mean error less than the reported error bands for the experimental heat transfer data.

The y+ values for this model are on the order of 1. The mean y+ value is 0.98 and the max is 2.5. The x+ and z+ values are both < 17. (The first cell size aspect ratios can be important for LES models.) The results for this solution may have been improved if all the y+ values were less than 1. (The implicit mesh dependence of the LES filter approach does not facilitate a full mesh independent solution.) To achieve this, the size of the first element would need to be more than halved in all three directions to maintain the same y+, x+ and z+ values. The net increase in the number of cells in the solution may have increased up to 8 times and the time step would need to be reduced by a factor

of two as well. The available computer resources for this study would have made this adjustment impractical.

Finally, if this much finer model did result in a perfect or near perfect match with the experimental data, the overall conclusion of this study would still confirm conclusions reached later in this chapter: The computational cost of the improved accuracy with LES approach is prohibitively expensive for the industrial used and simpler URANS approaches are more cost effective for many applications.

In addition to the Dynamic Smagorinsky model used as the LES simulation in this study, the WALE [60] model was also attempted for the staggered tube bank with the same mesh. The Dynamic Smagorinsky model was found to be slightly more accurate for this case as shown in Figure 5-12. For this reason, the Dynamic Smagorinsky model was chosen for this study because this increased in accuracy.

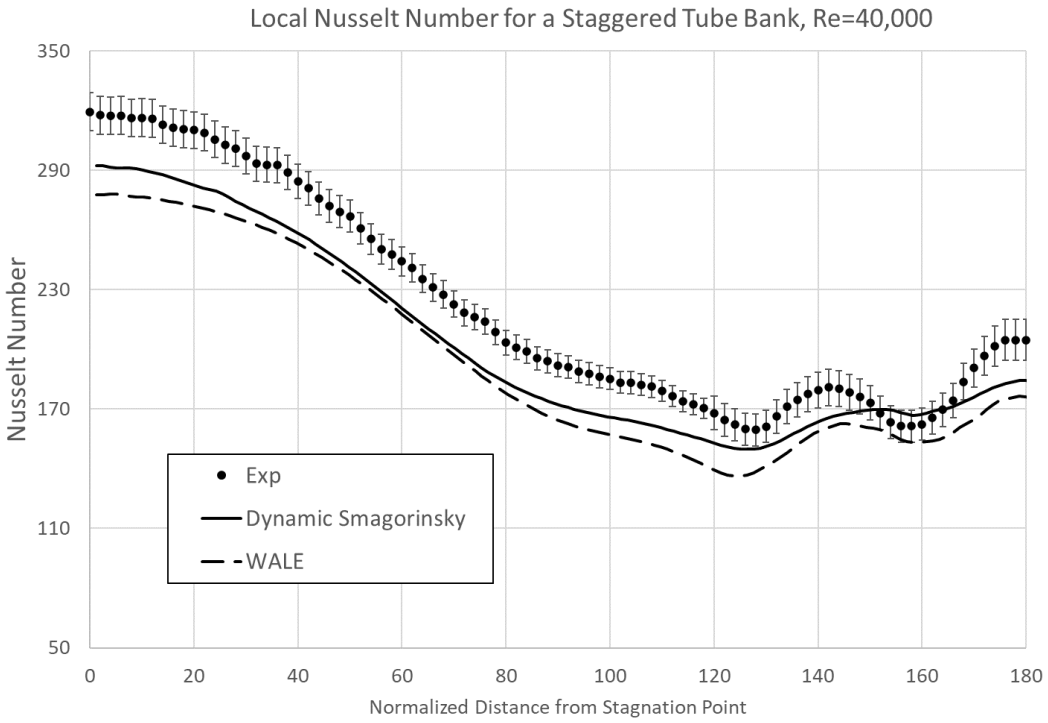

Figure 5-12 Local Nusselt number for staggered tube bank as found by the Dynamics Smagorinsky and WALE LES models.

5.2 Square in cross flow

Before evaluating the results of the six models relative to the experimental results, it is useful to consider the flow patterns for this geometry. Flow separation occurs just past the leading face of the square and generally does not permanently reattach again anywhere on the square. The downstream wake behind the square is dominated by the von Karman vortex sheet while local transient eddies near the rear and side faces are created. The interaction of the eddies with the wall directly impacts the shape of the local heat transfer profile. Smaller eddies are created on the sides within the separation bubble and are approximately an order of magnitude smaller than the square. Simultaneously,

larger eddies are shed off the rear of the square that are the same order of magnitude as the square. A steam line plot that shows the instantaneous flow pattern for the PANS-SST model is shown in Figure 5-13. The oscillating flow pattern on the rear and sides of the square also impacts the location of the stagnation point on the front face. As shown in this figure, the stagnation point is off center (y=0) in this arbitrarily chosen instant. The stagnation point will oscillate up and down with the action of the separated flow. This up and down movement of the stagnation point tends reduce the variation in the time averaged local Nusselt number on the leading face. The up and down sweeping of the attaching-detaching turbulent flow on the rear surface also enhances the heat transfer on this location. Overall, the turbulent flow impinging on the rear face results in a higher Nusselt number than the front face despite the lower impinging velocity.

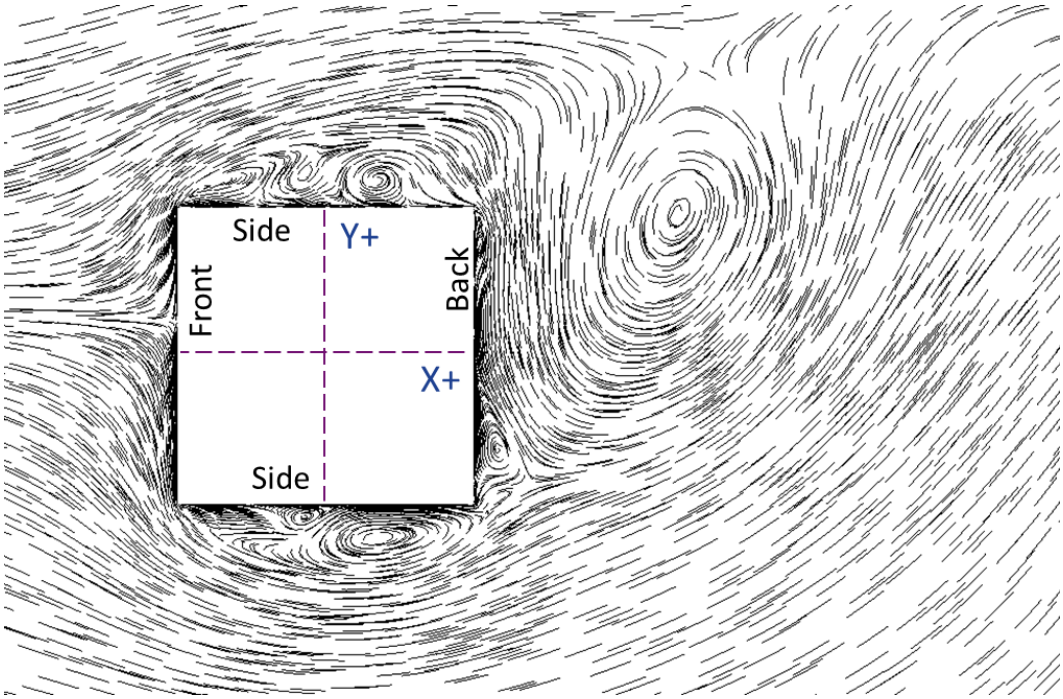

Figure 5-13 Streamline plot for transient solution for PANS-SST model at arbitrary instant in time

The time averaged streamlines are shown in Figure 5-14. In this figure, the time averaged eddies on the rear surface are attached and centered on the geometry symmetry. The size of the recirculation bubble and the areas of flow separation and reattachment are clearly evident. The ability of a CFD model to properly resolve these eddies, or at least model them in a time averaged way, directly impacts the accuracy of the local Nusselt number prediction. This short qualitative discussion of these flow patterns will help understand the performance of the CFD models relative to the experimental data.

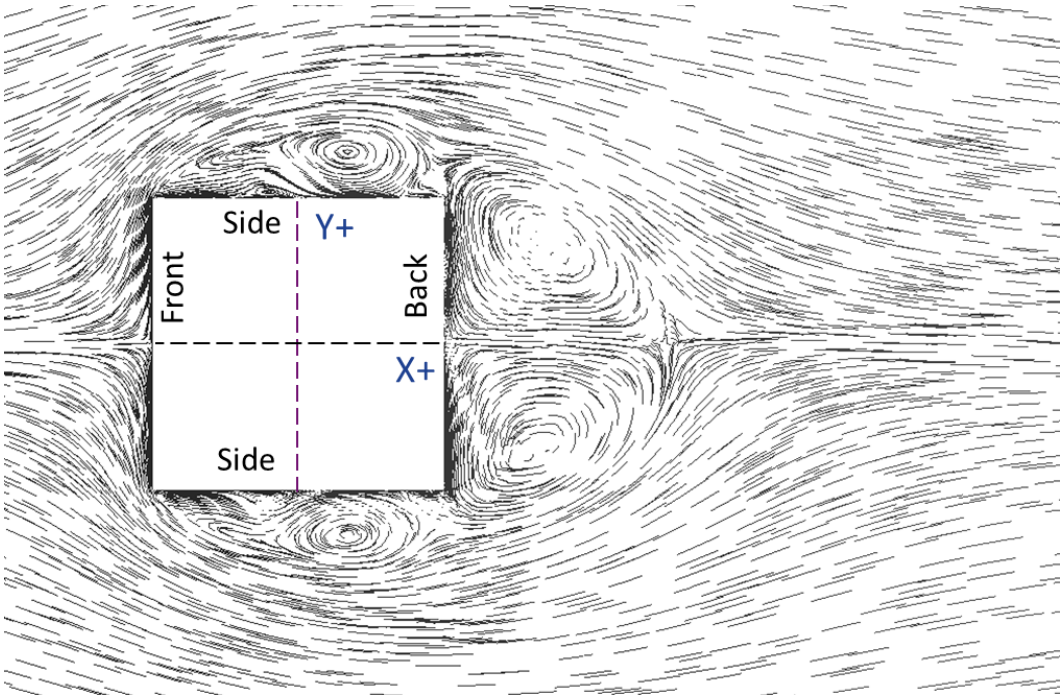

Figure 5-14 Time averaged streamline plot for PANS-SST model

The Nusselt number results of the six unsteady models along with the SRANS SST model for the square in cross flow are provided in Figure 5-15. Also plotted in this figure is the experimental data [85] with error bars of +/- 5% [86]. The x-axis on this chart is the normalized distance on from the stagnation point, s/D. In addition to the portions of the square labeled at the top of Figure 5-15, the s/D values for the corner points of the square are provided in Figure 3-7.

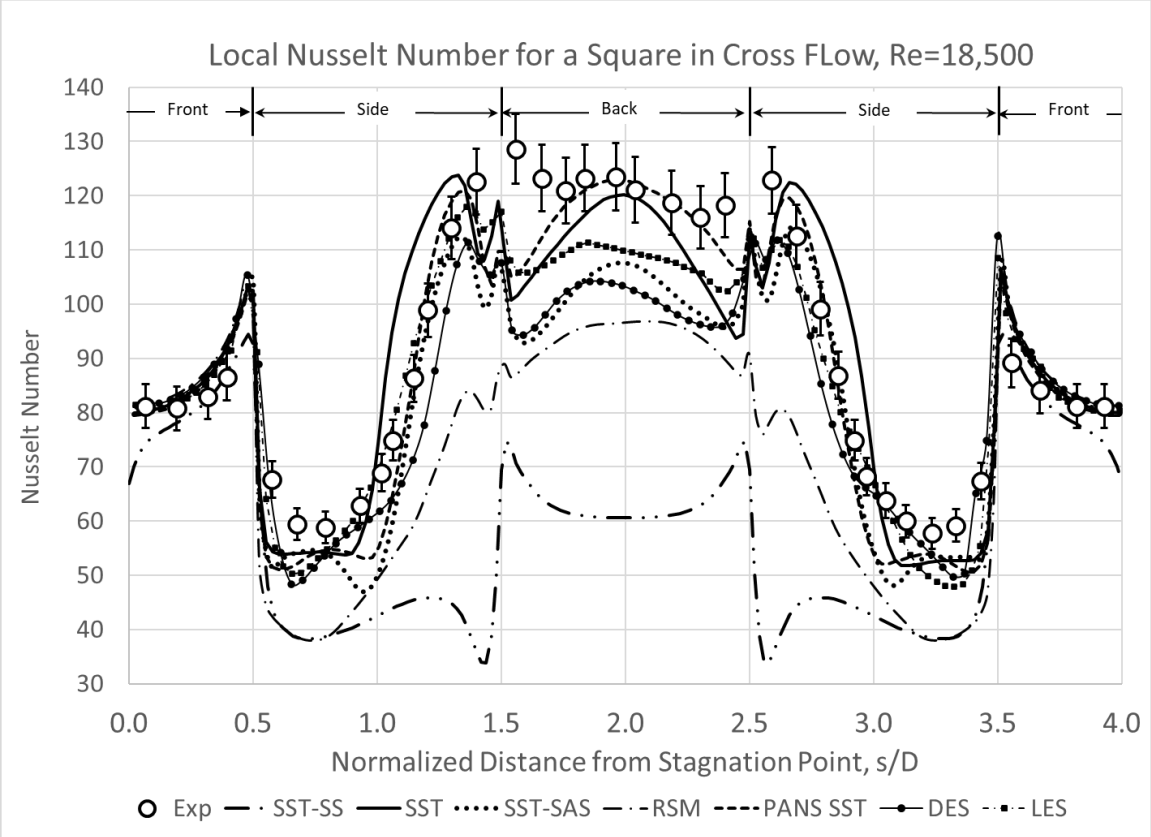

Figure 5-15 CFD and experimental [81] results for the local Nusselt number for square in cross flow

The results are also summarized by each side of the square along with the percentage error relative to the experimental correlation in Table 5-3 SRANS SST model significantly unpredicts the heat transfer on the rear surface of the square. In contrast, most of the unsteady models predicted the overall mean Nusselt number reasonably well (< 15% error) except for the Reynolds Stress model. This model underpredicted the overall Nusselt number by 23%. Most of the error in the prediction occurred in the separated areas. All the models provided very good accuracy on the upstream face indicating the inlet boundary conditions were sufficiently accurate to match the wind tunnel conditions of the experiment. In contrast, the model results were all lower than the

experimental value on the rear face the and they showed a significant variation from each other.

Table 5-3 Result of CFD model for the square in cross flow compared to experimental data

	Nusselt Number by Side				Error			
Model	**All**	**Front**	**Sides**	**Back**	**All**	**Front**	**Sides**	**Back**
Exp.	97.9	87.0	91.6	121.0	+/-5.0%	+/-5.0%	+/-5.0%	+/-5.0%
SRANS SST	58.0	80.4	43.6	64.0	-40.8%	-7.7%	-52.4%	-47.1%
SST	90.6	86.6	82.9	110.2	-7.5%	-0.5%	-9.6%	-8.9%
SAS	83.8	86.7	73.8	101.1	-14.4%	-0.4%	-19.5%	-16.5%
RSM	75.4	88.0	58.0	97.5	-23.0%	1.1%	-36.7%	-19.4%
PANS	88.5	85.9	76.1	115.8	-9.6%	-1.3%	-16.9%	-4.3%
DES	84.3	87.6	74.9	99.9	-13.9%	0.7%	-18.3%	-17.4%
LES	87.4	86.1	76.0	111.4	-10.8%	-1.1%	-17.1%	-8.0%

As with the staggered tube bank, the CFD velocity and Reynolds stress data is plotted alongside the experimental data in Figure 5-16 through Figure 5-19. The locations for the profiles shown in these figures are provided in Figure 3-7. Table 5-4 lists drag (C_d) drag root mean square (C_d') and lift root mean square (C_l') coefficients, Strouhal numbers as well as the size of the recirculation bubble (l_R) for each case. This is measured from the center of the square and is normalized by the length of the square sides. The l_R value is found by recording where the time averaged x-velocity is zero and the flow recirculates back towards the rear face of the square, indicating the size of the recirculation zone. The drag and lift coefficients were calculated using the mean velocity found as the flow passes the center of the square rather than the inlet velocity to account for the blockage factor in the wind tunnel. Results from a few published CFD studies also performed on this data are provided in this table as well.

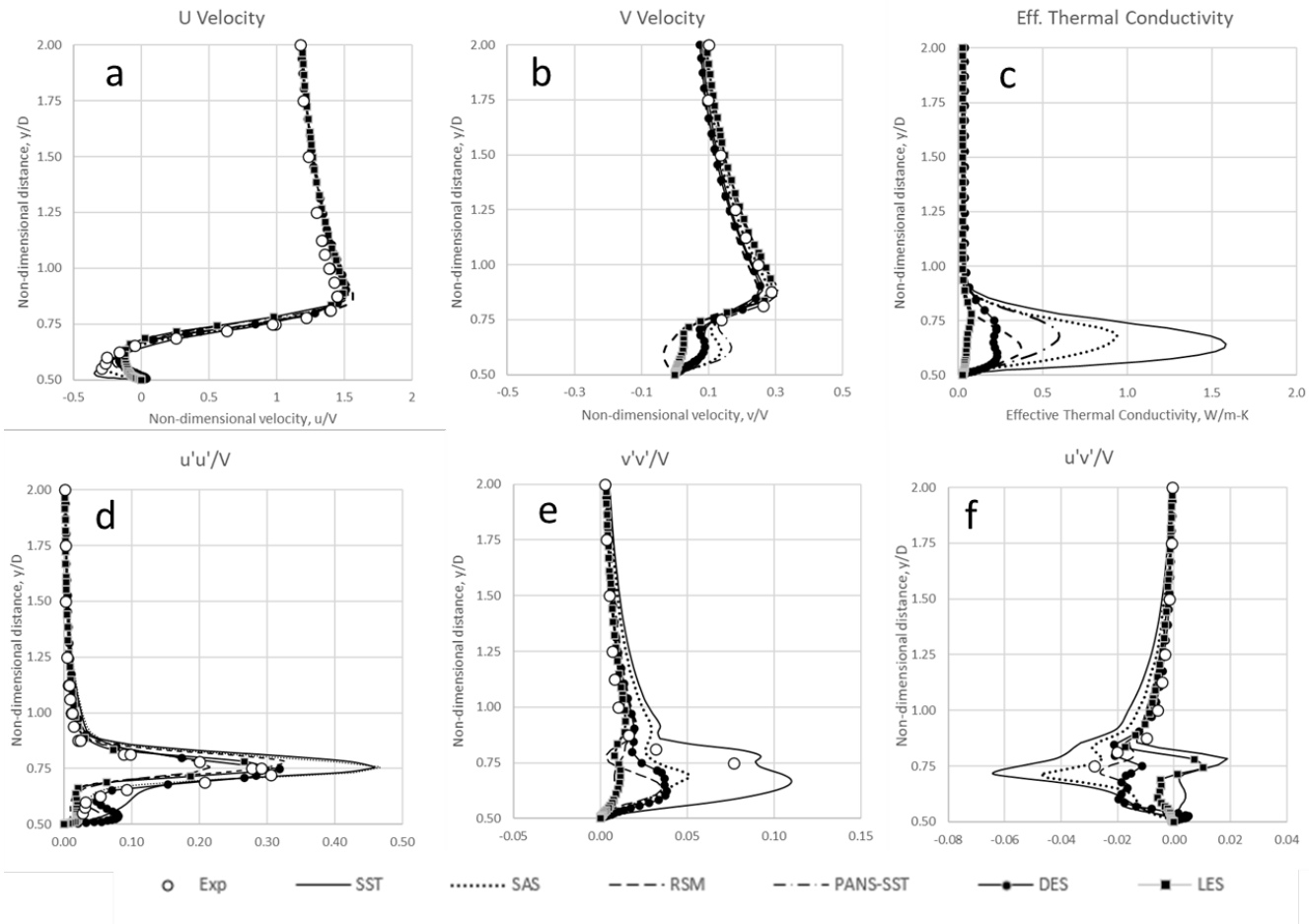

Figure 5-16 Velocity and Reynolds stress profiles for square in cross flow at x/D=0.0; u-velocity(a), v-velocity (b), effective thermal conductivity (c), normalized Reynolds stress $\overline{u'u'}/V^2$ (d), $\overline{v'v'}/V^2$ (e), and $\overline{u'v'}/V^2$ (f)

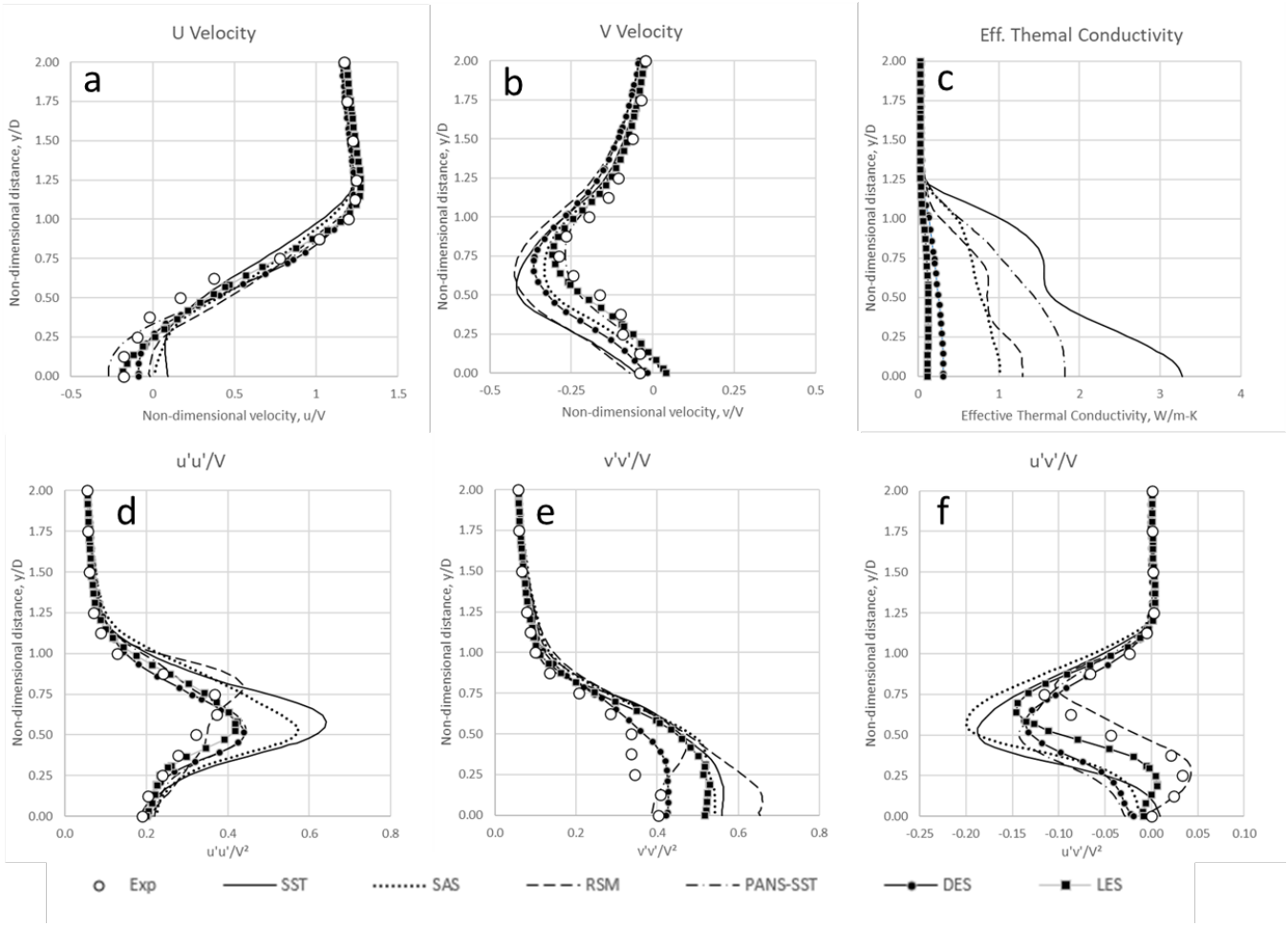

Figure 5-17 Velocity and Reynolds stress profiles for square in cross flow at x/D=1.0; u-velocity(a), v-velocity (b), effective thermal conductivity (c), normalized Reynolds stresses $\overline{u'u'}$/V² (d), $\overline{v'v'}$/V² (e), and $\overline{u'v'}$/V² (f)

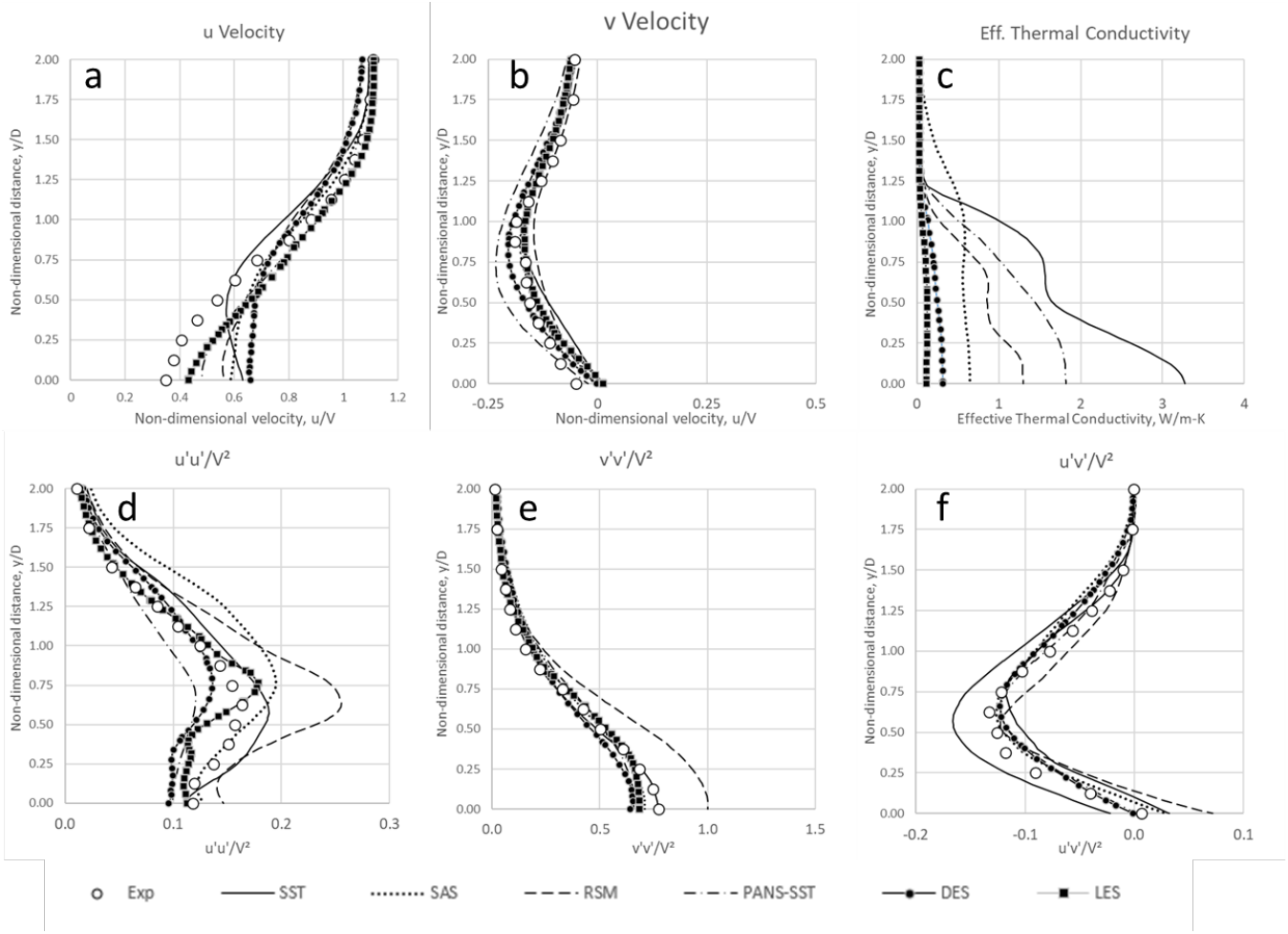

Figure 5-18 Velocity and Reynolds stress profiles for square in cross flow at x/D=2.0; u-velocity(a), v-velocity (b), effective thermal conductivity (c), normalized Reynolds stresses $\overline{u'u'}/V^2$ (d), $\overline{v'v'}/V^2$ (e), and $\overline{u'v'}/V^2$ (f)

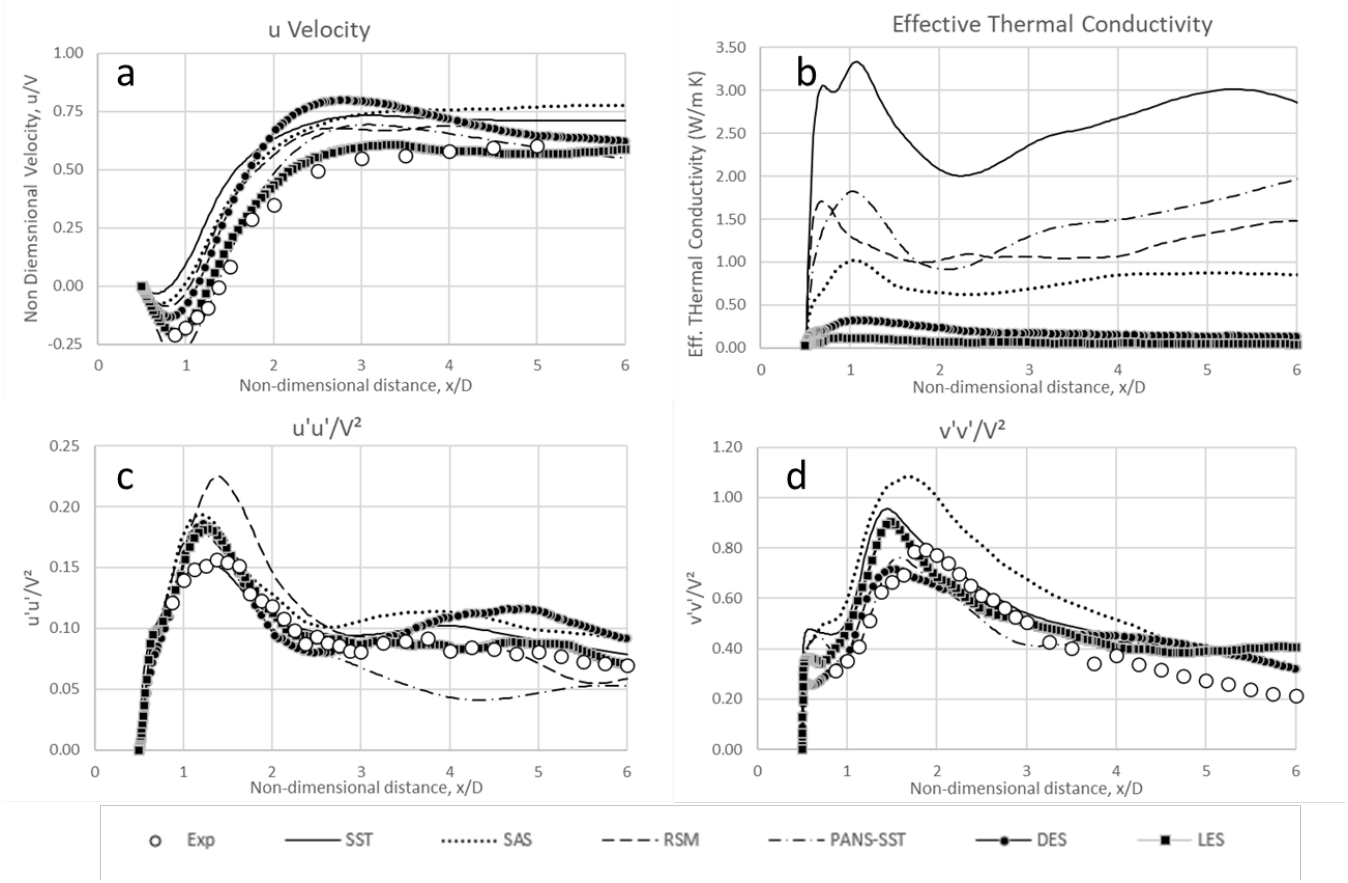

Figure 5-19 Velocity and Reynolds stress profiles for square in cross flow at y/D=0; u-velocity(a), v-velocity (b), effective thermal conductivity (c), normalized Reynolds stresses $\overline{u'u'}/V^2$ (d), $\overline{v'v'}/V^2$ (e), and $\overline{u'v'}/V^2$ (f)

Table 5-4 Square in cross flow results for Strouhal number, drag and lift coefficients and size of recirculation bubble

	Model	Re	Time Step (μs)	Mesh	St	C_d	C_d'	C_l'	l_R
Present Study	SST	18,500	50	C	0.132	2.085	0.260	1.508	0.820
	SST-SAS	18,500	50	C	0.130	2.082	0.310	1.262	0.977
	RSM	18,500	50	C	0.136	2.070	0.379	1.212	1.045
	PANS-SST	18,500	50	C	0.133	2.110	0.425	1.304	1.354
	DES	18,500	20	D	0.140	2.070	0.379	1.212	1.127
	LES	18,500	7.5	E	0.132	2.015	0.247	1.196	1.263
Exp	Lyn	21,400			0.132 +/- 0.004	2.1			1.38
	Lee, 1975					2.05	0.16-0.23		
	Vickery 1966					2.05	0.1-0.2	0.68-1.32	
Previous Study	Ranjan, PANS SST				0.129	1.97			1.3
	Rodi et al., 1997, LES				0.13	2.2	0.14	1.01	1.32

The drag and coefficients for the square in cross flow showed very good results relative to the experimental data. There is more variance in the root mean square of the drag and lift coefficients, C_d' and C_l'

Figure 5-20 shows the instantaneous turbulent viscosity ratio for the six models. The contour plots use the same scale to demonstrate the relative levels of modeled turbulence. The ratio of resolved-to-total turbulent kinetic energy at y/D = 0 downstream of the square is provided in Figure 5-21. The instantaneous vorticity magnitude is shown in Figure 5-22. This figure demonstrates how the model is capturing the near wall eddies as well as the creation of the von Karman vortex sheet. The increased levels of the resolved turbulence are evident in the SST-SAS, DES and LES models as these models resolve smaller scale eddies within the vortex sheet.

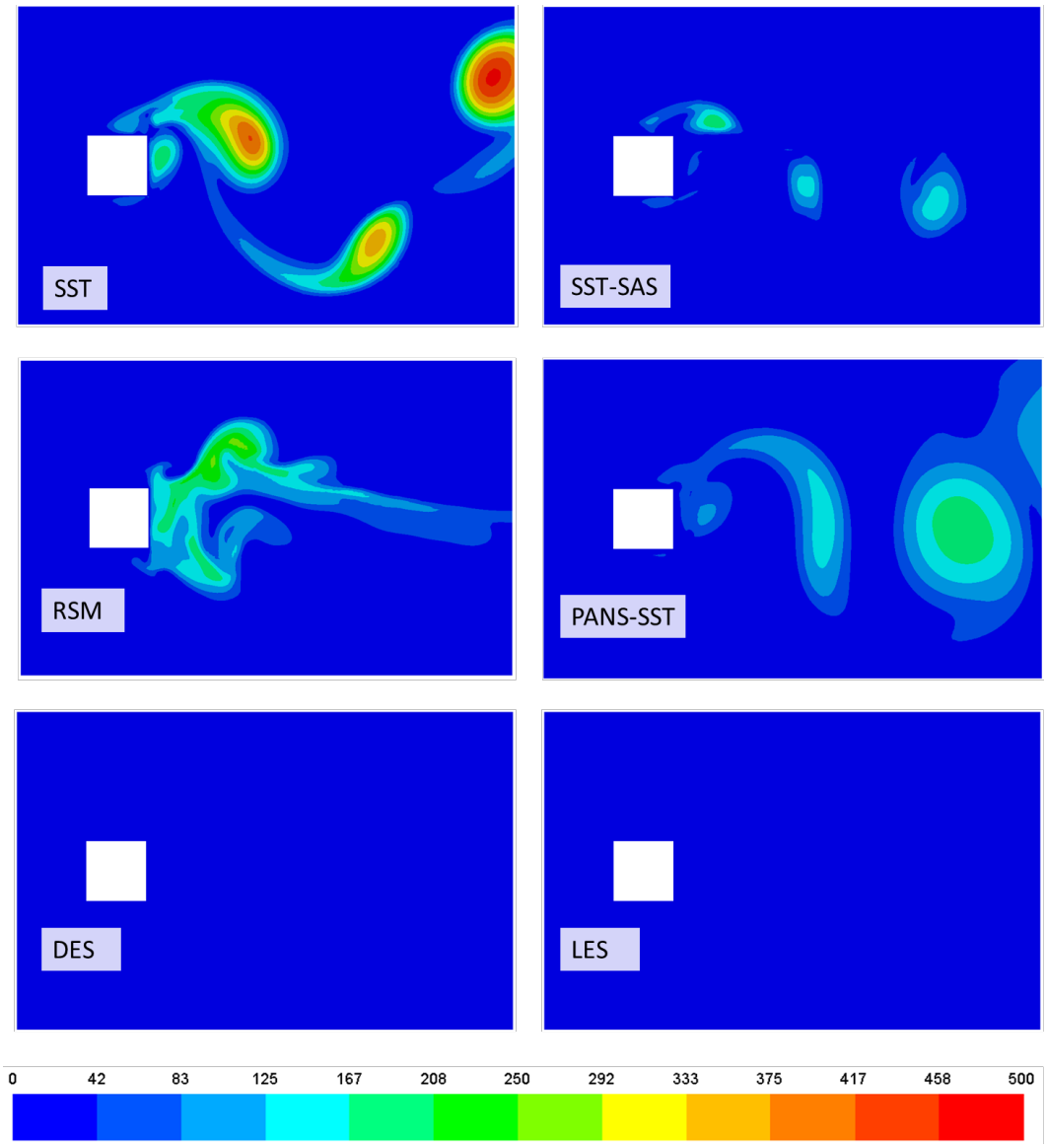

Figure 5-20 Instantaneous turbulent viscosity ratio (turbulent viscosity/ molecular viscosity) for square in cross flow for the size models

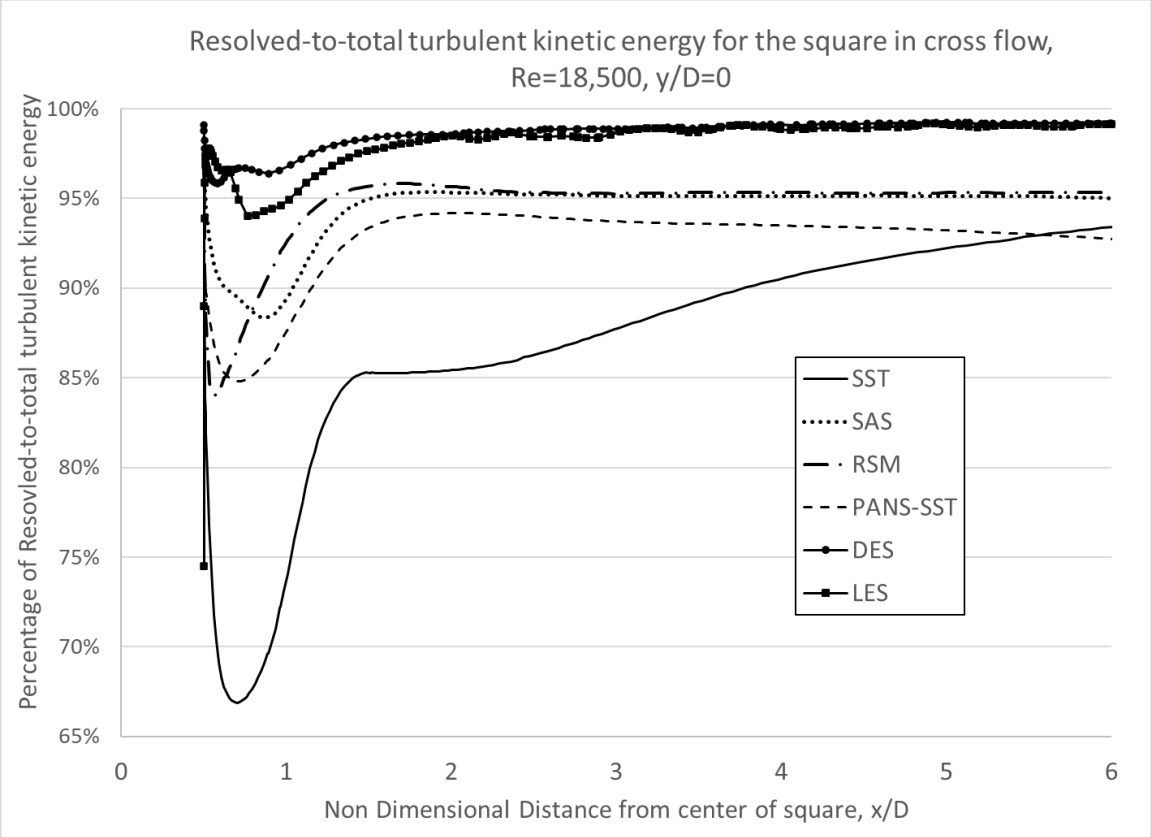

Figure 5-21 Ratio of resolved-to-total turbulence for the square in cross flow at y/D=0, downstream of the square

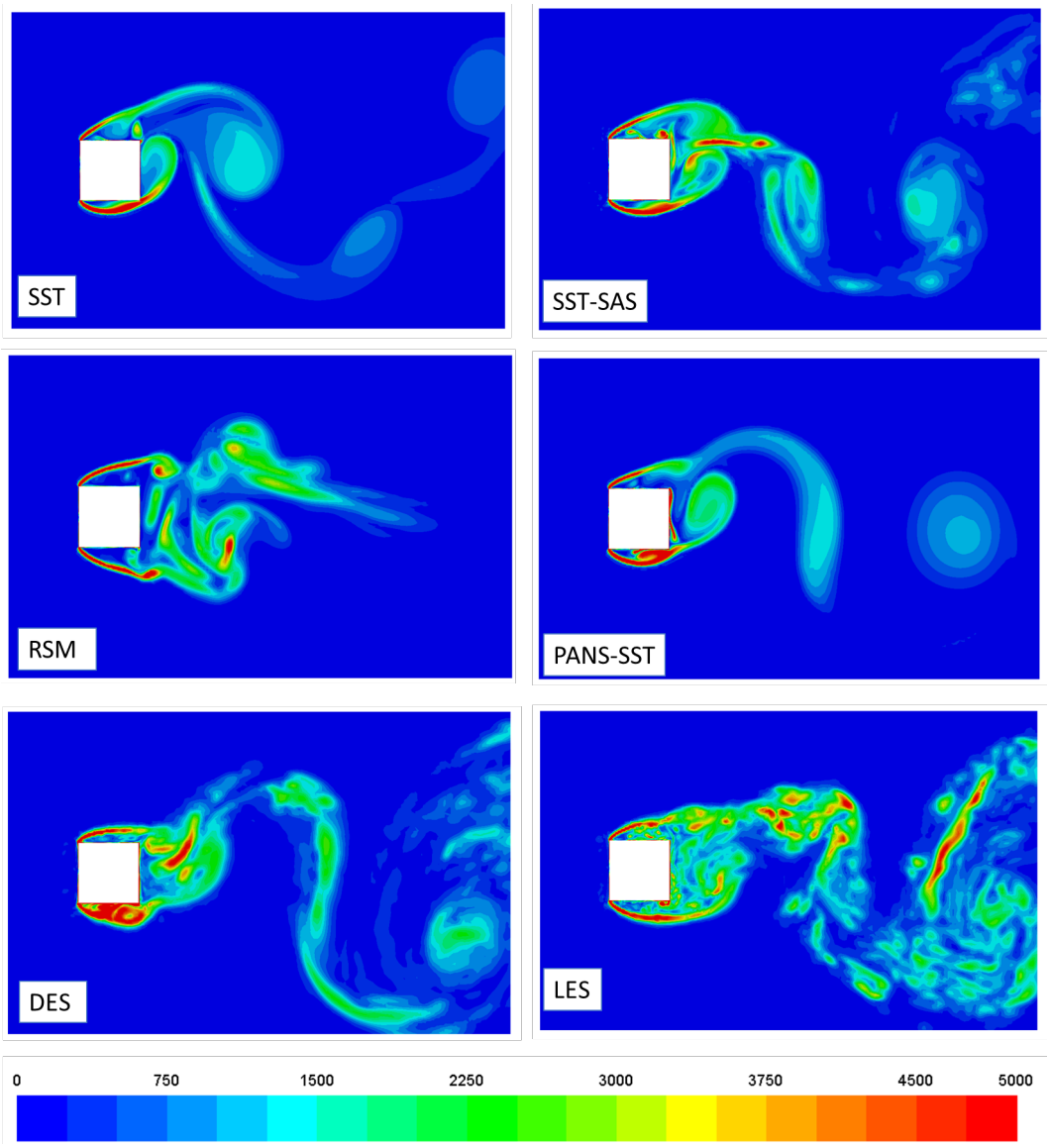

Figure 5-22 Vorticity magnitude for the square in cross flow for the six models

5.2.1 Assessment frequency domain analysis and degree or resolved turbulence for the square in cross flow

The frequency domain plots from the velocity traces downstream of the square are provided in Figure 5-23. This Fourier transform is performed with velocity magnitude

data take from a point at x/D=3, on the y/D=0 line. The experimental Strouhal number for this flow configuration is 0.132 +/- 0.004 [80]. From an inlet velocity of 9.7082 m/s the expected vortex shedding frequency is 43.03 Hz. Some of the models (RSM, PANS-SST, DES and LES) and showed a peak response in the frequency domain at twice the shedding frequency. In this case the half harmonic was used to determine the Strouhal number. The Strouhal number of all but one of the models is within the experimental margin of error as shown in Table 5-4. The exception is the DES model which has a Strouhal number of 0.140.

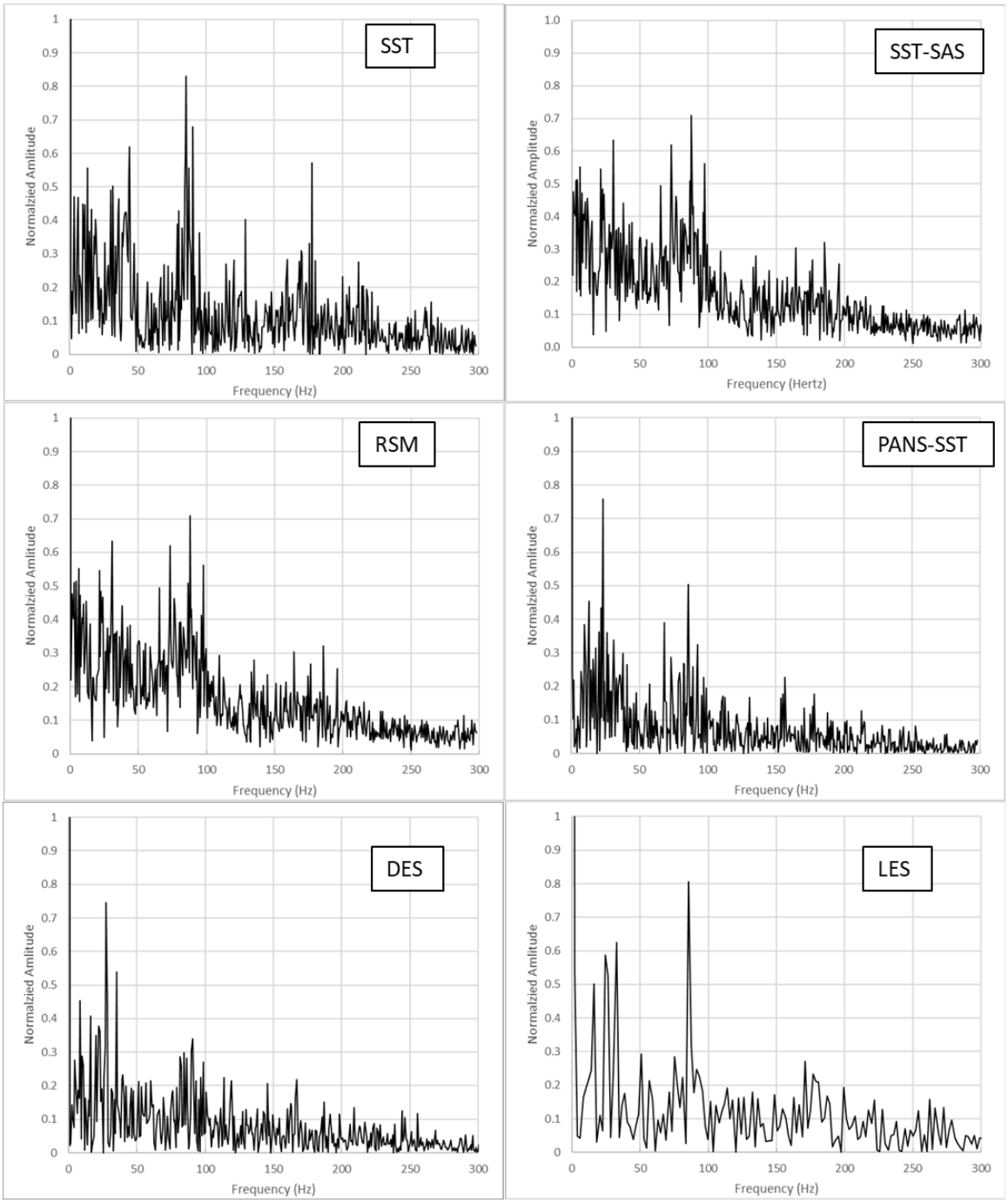

Figure 5-23 Frequency domain analysis of velocity trace from CFD models for square in cross flow

5.2.2 Heat transfer and flow profiles for the square in cross flow

5.2.2.1 SST model

The steady SST model showed very poor results for this case. The overall mean Nusselt number was 58, relative to the experimental value of 97.9 as shown in Table 5-3. In addition, the steady SST profile showed large deviations along the sides and rear of the square with errors of ~50%. The difference between the accuracy of the steady and unsteady SST model is significantly larger for the square in cross flow than the staggered tube bank. This may be because the more confined space of the staggered tube bank limits the separated areas where the steady solution will be more challenged.

The URANS SST model showed a good overall match to the experimental Nusselt number data with a mean error of -7.5%. However, inspection of the local values in Figure 5-15 shows local variance relative to the data. The mean error on the sides is 9.6% lower and the mean error on the rear is 8.9% lower. In addition, the overall shape of the curve does not match the data well. The profile at the rear face for the SST model shows a significant concave downward profile while the experimental data is this area is nearly flat. This indicates that the SST model is not resolving the smaller turbulent scales in the separated region that would be expected to create a more even profile. The SST model under predicted the non-dimensional length of the time averaged separation bubble behind the square with the CFD result being 0.820 relative to an experimental value of 1.38. This would be expected to also correlate to a lower local Nusselt number because the smaller recirculation bubble would also see a lower velocity impinging on the rear

surface. This was not found for this case, however. Rather, the higher effective thermal conductivity as shown Figure 5-19b compensates for the lower velocities as described by Equation (53).

The velocity and Reynolds stress profiles matches provided in Figure 5-16 through Figure 5-19 show the SST model is less accurate in a number of areas. Despite these local short comings, the SST model is remarkably effective at finding the overall Nusselt number.

5.2.2.2 SST-SAS model

As discussed in section 2.2.2, the SST-SAS model is modification to the SST model that adjusts the local production of the specific dissipation in areas of flow separation, among others. The resulting increase in resolved turbulence is expected to improve the accuracy of the model. Separated regions of the square would then provide an excellent opportunity to demonstrate this capability. Review of the data shows that this was true in one area on the sides between s/D=1.0 to s/D=1.3. However, the results were actually worse on the rear portion of the square. The overall mean Nusselt number was 14.4% less than the experimental data compared to the -7.5% for the SST results. In the rear section, the average Nusselt number was 16.5% below the experiment while the SST model was 8.9% below.

The normalized size of the recirculation bubble is 0.977, which is a modest improvement over the SST model. This small increase in the impinging velocity on the rear surface

would be expected to result in a small increase in the heat transfer. However, the effective thermal conductivity in this area is roughly a third of that found for the SST model as shown in Figure 5-19b. Adjustments to the turbulent Prandtl number could have been made from the typical 0.85 value but this was not attempted as it was not the focus of the present study.

The degree of resolved turbulence immediately behind the square for the SST-SAS model is ~90% while the SST model is ~70%. The increase in the degree of resolved turbulence does not yield an increase in the accuracy of the heat transfer solution. Potential improvements for the SST-SAS model to address this issue is discussed in Chapter 6.

5.2.2.3 Reynolds Stress Model

The RSM solution found significantly lower Nusselt values in all but the front facing portion of the square. This model also showed the worst overall match of all the unsteady models considered here. The overall Nusselt number was 75.4 compared to the expected value of 97.9. The worst result occurred on the sides of the square where the model under predicted the data by 36.7%. The instantaneous vorticity plot shown in Figure 5-22 for the RSM model shows a very different flow pattern than the other models. While the von Karman vortex sheet is created, it is only apparent further downstream. Nearer the rear and sides of the square a more dramatic flow separation that has a less oscillatory nature is found. This flow pattern looks similar to a steady state solution which would suggests that a smaller time step would enable better results. However, when the time step was halved, the flow pattern and local Nusselt numbers

were the found to be same. (For the smaller time step case, the CFL number was less than one in all areas except the leading corners of the square.)

The reduced heat transfer for this model shown in Figure 5-15 is due to the separated flow with limited surface impingement. This conclusion is also supported by the smaller size of the recirculation bubble of 1.045 than the experimental value of 1.38.

5.2.2.4 PANS-SST model

The PANS-SST model showed a good improvement over the SST model. The overall mean Nusselt number dropped very slightly from 90.6 for the SST model to 88.5 for the PANS-SST while the experimental correlation was 97.9. The largest benefit of the SST modification was the improved match on back half of the square sides, between s/D=1.0 to s/D=1.3 where the local Nusselt number was within error bars of the experimental data. On the rear face, the Nusselt number was 115.8 while the baseline SST model was 110.2. This is relative to an experimental value of 121.0. Overall, the PANS modification did enable a better match to experimental data over the SST model.

The PANS-SST solution required four updates to the f_k parameters to settle on a stable field to generate the final solution. This was more than the seven required for the staggered tube bank. The final f_k field is shown in Figure 5-24.

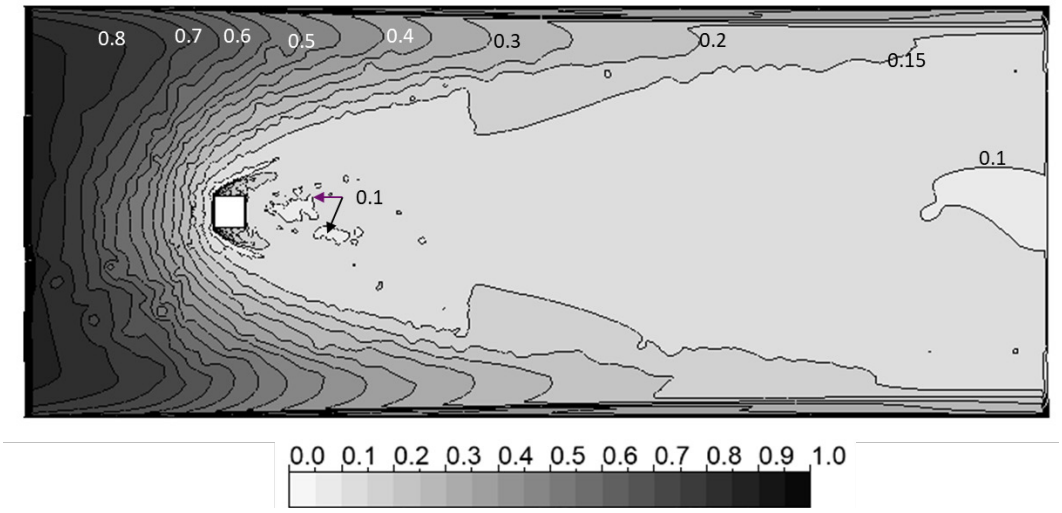

Figure 5-24 Ratio of unresolved-to-total (f_k)turbulent kinetic energy for the PANS-SST model

This plot shows that the majority of the region downstream of the square has a high degree of resolved turbulence while the steady regions at the inlet were mostly modeled. The PANS approach also provided an improvement in the velocity and the Reynolds stress profiles. The normalized size of the recirculation bubble for this model was the closet of all the other models with a sight over prediction of just 2%.

5.2.2.5 DES model

For the DES model, the overall mean Nusselt number was 88.5, or 13.9% below the experimental correlation. On the sides and rear the profile shape matched the local data well but there was a significant downward shift in the model results. On the sides and rear of the square, the DES model was ~18% below the data. Reviewing the profile data in Figure 5-16 through Figure 5-19, good matches are found for the flow data. Like the LES model, DES showed a very high degree of resolved as shown in Figure 5-21. Unlike the staggered tube bank, the degree or resolved turbulence was very high throughout the

flow field. As such adjustments to the turbulent Prandtl number is unlikely to provide much improvement to the Nusselt number results.

5.2.2.6 LES model

The overall mean Nusselt number for the LES model was -10.8% below the experimental value and the error for the sides was -17.1%. While other models reported better mean Nusselt number values for a side, the LES results showed the best match for the shape of the experimental data. The mean error on the rear of the square as -8.0% which on average is below the PANS-SST value of -4.3% but the LES solution provided a flatter profile that the other models and better match to the experimental data in this way. The LES data also closely matched the side portions between s/D=1.0 and s/D=1.4 similar to the PANS-SST result. The profiles for the u- and v-velocity data matched the LES results very well and the size normalized side of the recirculation bubble was 1.263 which is only slightly smaller than the experimental value of 1.38. The wall resolution for this case was as follows: $y+ \sim 1$, $x+ < 11$ and $z+ < 16$.

The Wall Adapting Local Eddy-Viscosity (WALE) model [60] was also attempted for this case but the results were less accurate than the Dynamic Smagorinsky model and it was not used as part of this study.

5.3 Summary of results

The Reynolds number for both cases considered in this study are similar but the flow regimes are quite different. The turbulence in the staggered tube bank is more evenly

distributed throughout the flow space than the square in cross flow. Another difference between the two cases is that the close spacing of the staggered tubes limits the degree of flow separation. In contrast the flow moving around the square pushes the fluid away to create a much larger wake.

The six models all predicted similar Nusselt number profiles for the tube bank. There is some variance but not the same extent as the square. The rear face of the square demonstrated the largest variation between the models. Considering both cases together, the PANS-SST model was the most accurate but the LES model provided the best match for the profile shape, albeit at consistently lower value.

The failure of all but the LES solution to capture the previously discussed bump at 140° from the stagnation point has a significant impact on the accuracy of the models in this area. The SST-SAS and PANS-SST models may have showed increased accuracy in this area if the mesh was locally refined to allow the solution to capture the near wall eddy.

The challenge for the selecting a turbulence model for a new problem is to know which approach will provide the most accurate results with the available computer resources. While a turbulence model can be developed to address specific flow conditions, this study has shown that a particular problem may not actually show the expected improvement. Despite this, some conclusions can be drawing from the results of the two cases studied here. These conclusions have already been presented in the text but are include in Table 5-5 for clarity.

Table 5-5 Summary of strengths and weaknesses for the six turbulence models

Model	Strengths	Weakness
SST	Good overall mean Nusselt number accuracy.	Local Nusselt number profile varied from data.
SAS-SST	Resolved more turbulence.	Does not improve SST model for these cases.
RSM	Good mean and local Nusselt number accuracy for staggered tube bank.	Poor accuracy for square in cross flow.
PANS-SST	Good improvement over the baseline SST model, particularly with respect to local Nusselt number profile.	Updates to f_k field require more computer time along with additional intervention of the user.
DES	Good matching of local Nusselt number profile.	Underprediction of mean Nusselt number.
LES	Best match to local Nusselt number profile.	Underprediction of mean Nusselt number but better than DES.

5.4 Evaluation of Accuracy relative to Computational cost

The model error relative to the experimental value for the two cases is provided in Figure 5-25 Figure 5-26. The absolute values of the errors are presented to facilitate a better interpretation of the results. The computer run times are normalized to the time required for the URANS-SST solution. This provides a convenient basis to evaluate each model.

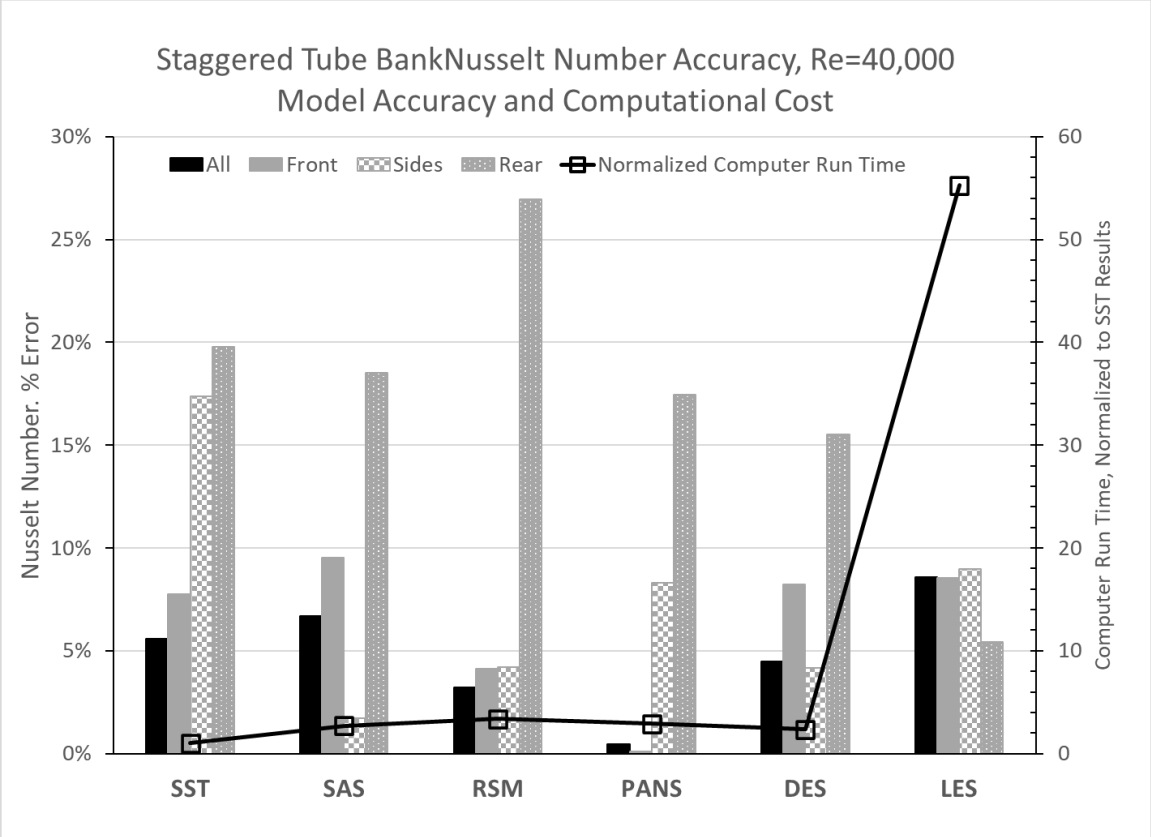

Figure 5-25 Accuracy of absolute value mean Nusselt number error relative to computational cost for staggered tube bank

The accuracy of the experimental data should also be considered when evaluating this data. The overall accuracy of the staggered tube bank mean Nusselt number is +/- 3.5% with the front, side and back accuracy being +/-3.0%, 3.2% and 5.0% respectively. For the square in cross flow the overall and local accuracy is +/- 5%

With the staggered tube bank, the PANS-SST and the RSM models provide overall mean Nusselt number results that are within the experimental error while the SST and DES are slightly outside it. The good LES profile match is not represented in this chart but the large computational cost is clearly evident relative to the other models. The DES model had a reasonable run time due to the relatively limited number of time steps required but

the only significant improvement was in the side region relative to the SST results. Overall, the SST model provides a good balance of cost relative to accuracy and the SAS-SST and PANS-SST showed good improvement for about ~3 times the computational cost.

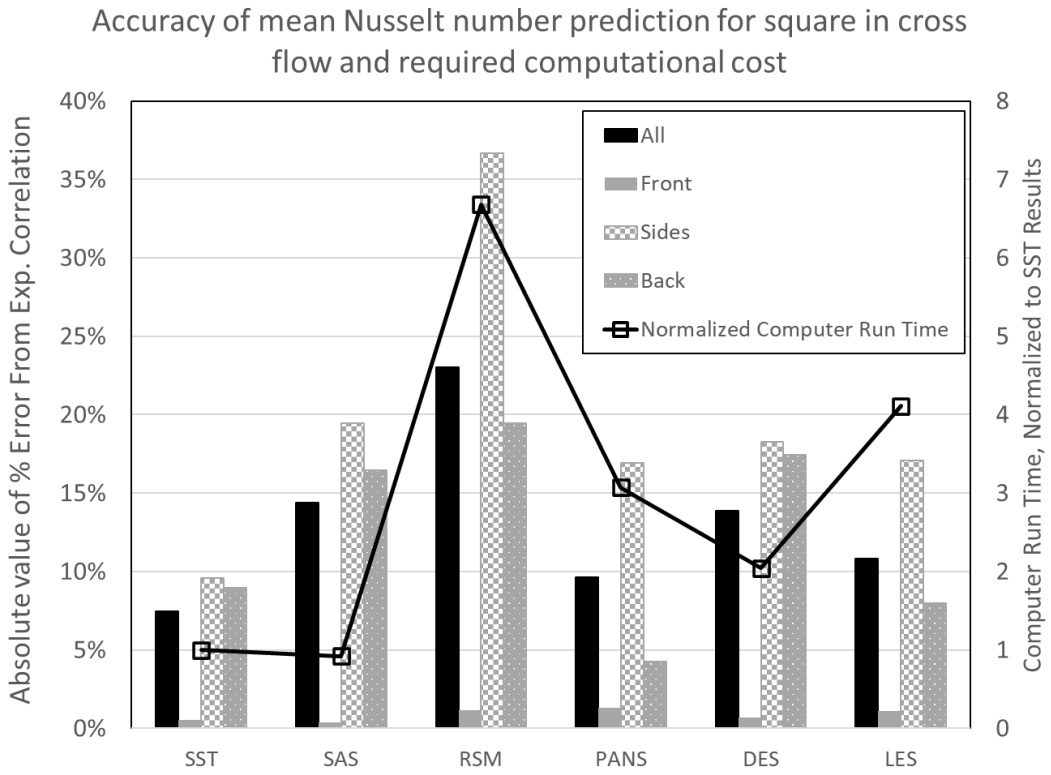

Figure 5-26 Accuracy of absolute value mean Nusselt number error relative to computational cost for square in cross flow

For the square in cross flow case, the SST model again provided a good balance of accuracy relative to computational cost. This model did show some variance to the experimental results but the overall mean values were quite good. The PANS-SST model showed a noticeable improvement for the local Nusselt numbers at the rear of the square as well as a portion of the square sides. The most challenged model for this case was the

RSM model where the time required to reach stable mean values was nearly twice that of LES. While this indicates that the more random aspects of the turbulence are resolved, the benefits in accuracy is not found.

The SAS-SST model, which was developed to improve on the accuracy of flow conditions found in these two cases, actually saw a decrease in the accuracy in the separated areas. Since the computational costs were comparable to the SST model, it would be very useful to investigate ways to improve the accuracy of the SAS approach. This is the top of the next chapter of this study.

6 IMPROVEMENT OF SCALE ADAPTIVE SIMULATION MODEL FOR SST

The PANS model provides excellent results relative to the other models, particularly for the grid size and computer resources used. However, this model would be difficult to implement in commercial CFD software due to the sequence of steps required gain a final solution. The SAS model on the other hand is quite straight forward to use and is already available in ANSYS Fluent. Unfortunately, the present work has shown that the SAS model is not particularly effective for the two cases evaluated here. In fact, the SAS model is generally worse than the SST model it was intended to improve. This is particularly true on the rear face of the square in cross flow.

This section presents a novel improvement to the SAS model intended to increase the accuracy of the square in cross flow and staggered tube bank results already presented.

6.1 Model basis and derivation

The SAS model is presented in a number of papers authored by Florian R. Menter with other contributors [10, 11, 89-91]. This section will summarize the development of this model based on the references listed.

Two equation turbulence models use two transport equations to model the two independent scales[10]. The first equation is typically the turbulent kinetic energy, k and the second can vary depending on the type of model. The k equation can be modeled

directly by developing terms to represent the convection, production, destruction and diffusion of k. The development of the second equation for the dissipation, ε, or the specific dissipation, ω, however is typically derived by analogy of the k equation and the terms are created by making order of magnitude arguments [10]. This is because the specific terms of these transport equations cannot be derived directly.

The development of the Scale Adaptive Simulation is based on work by Rotta [46, 92] to derive an exact transport equation for kL as the second scale determining equation. (kL is the product of the turbulent kinetic energy k and L is the integral turbulent length scale.) The derivation of the kL transport equation is first made for a simple shear flow (linear velocity gradient) which creates homogenous turbulence. This derivation will be summarized in brief here with particular attention paid the subsequent improvement of this model presented later in this chapter. This model is later generalized to fully 3-D flow and transformed into the transport equation for specific dissipation for the SST-SAS model.

This kL term is defined as the integral of the two-point correlation tensor as shown in equation (54) and (55).

$$kL = \frac{3}{16}\int_{-\infty}^{\infty} R_{ii}(\vec{x}, r_y)dr_y, \tag{54}$$

The correlation tensor is defined as product of the random component from two velocity probes separated by a displacement vector r_y. This is shown graphically in Figure 6-1. The two-point correlation tensor is defined as

$$R_{ii} = \overline{u'_\iota(\vec{x})u'_\iota(\vec{x}, +r_y)} \tag{55}$$

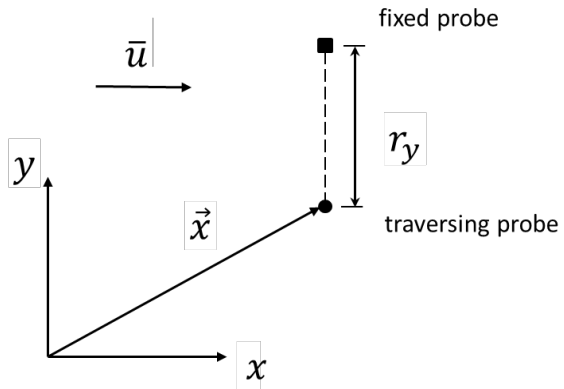

Figure 6-1 Two-point correlation measurement

The curve for the correlation tensor for a simple shear flow is shown in Figure 6-2.

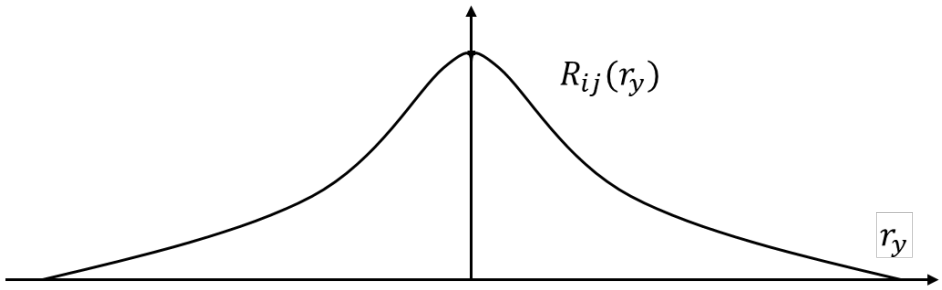

Figure 6-2 Correlation Tensor for turbulent flows

The correlation tensor will result in the value of 1 then r_y is diminishingly small because the transient components of the velocity vector will be identical. At a sufficient distance apart, the correlation tensor of the two probes will be 0. Integrating the expression yields a flow parameter that is defined as $\Psi = kL$.

Deriving the transport equation (56) for Ψ [10] yields a set of terms that can be defined explicitly without resorting to scaling arguments or analogies with the k equation [10].

$$\underbrace{\frac{\partial \Psi}{\partial t}+\bar{u}_j\frac{\partial \Psi}{\partial x_j}+\frac{3}{16}\int_{-\infty}^{\infty}\left[\frac{\partial \bar{u}(\vec{x}+r_y)}{\partial x}-\frac{\partial \bar{u}(\vec{x})}{\partial x}\right]R_{ii}dr_y=}_{\text{Convection}}$$

$$\underbrace{-\frac{3}{16}\frac{\partial \bar{u}(\vec{x})}{\partial y}\int_{-\infty}^{\infty}R_{21}dr_y-\frac{3}{16}\int_{-\infty}^{\infty}\frac{\partial \bar{u}(\vec{x}+r_y)}{\partial y}R_{12}dr_y}_{\text{Production}}$$

$$\underbrace{+\frac{3}{16}\int_{-\infty}^{\infty}\frac{\partial}{\partial r_k}\left(R_{(ik)i}-R_{i(ik)}\right)dr_y+\nu\frac{3}{8}\int_{-\infty}^{\infty}\frac{\partial^2 R_{ii}}{\partial r_k \partial r_k}dr_y}_{\text{Destruction}}$$

$$\underbrace{-\frac{\partial}{\partial y}\left\{\frac{3}{16}\int_{-\infty}^{\infty}\left[R_{(ik)i}-\frac{1}{\rho}\left(\overline{p'v'}+\overline{v'p'}\right)\right]dr_y-\nu\frac{\partial \Psi}{\partial y}\right\}}_{\text{Diffusion}} \tag{56}$$

The production term is of particular interest, both for the unique nature of this derivation but also for the planned improvement for the Scale Adaptive approach. The second part of the production term, $-\frac{3}{16}\frac{\partial \bar{u}(\vec{x})}{\partial y}\int_{-\infty}^{\infty}\frac{\partial \bar{u}(\vec{x},+r_y)}{\partial y}R_{12}dr_y$, can be expanded with a Taylor series as shown in Equation (57)

$$\frac{\partial \bar{u}(\vec{x}+r_y)}{\partial y}=\frac{\partial \bar{u}(\vec{x})}{\partial y}+\frac{\partial^2 \bar{u}(\vec{x})}{\partial y^2}r_y+\frac{1}{2}\frac{\partial^3 \bar{u}(\vec{x})}{\partial y^3}r_y^2+\cdots \tag{57}$$

With this expansion the production term can be re-written as

$$\frac{\partial u(\vec{x}+r_y)}{\partial y}\int_{-\infty}^{\infty} R_{12}dr_y \rightarrow$$

$$\frac{\partial \bar{u}(\vec{x})}{\partial y}\int_{-\infty}^{\infty} R_{12}dr_y + \frac{\partial^2 \bar{u}(\vec{x})}{\partial y^2}\int_{-\infty}^{\infty} R_{12}r_y dr_y + \frac{1}{2}\frac{\partial^3 \bar{u}(\vec{x})}{\partial^2}\int_{-\infty}^{\infty} R_{12}r_y^2 dr_y + \cdots \quad (58)$$

Equation (58) shows a second and third order term for the production of Ψ from the Taylor expansion. In the original derivation of this transport equation for homogenous turbulence, it was concluded by Rotta that the second order term could be eliminated. For the case of homogeneous turbulence, the function R_{12} is symmetric and the product of $R_{12}r_y$ is asymmetric. The integral is then zero as the $-r_y$ and $+r_y$ contributions cancel each other [10].

Further work develops some coefficients, along with the models for the remaining terms to develop the kL transport equation [10].

$$\frac{\partial \Psi}{\partial t} + u_j\frac{\partial \Psi}{\partial x_j} = -\overline{u'v'}\left(\zeta_1 L\frac{\partial \bar{u}}{\partial y} + \zeta_2 L^3\frac{\partial^3 \bar{u}}{\partial y^3}\right) - \zeta_1 k^{3/2} + \frac{\partial}{\partial y}\left(\frac{\upsilon_t}{\sigma_\Psi}\frac{\partial \Psi}{\partial y}\right) \quad (59)$$

This transport equation is similar to other dissipation (ϵ), and specific dissipation (ω) models except for the inclusion of the third derivative in the production term of kL.

The $L^3\frac{\partial^3 \bar{u}}{\partial y^3}$ term is problematic however for a few reasons. The first is that the third derivative does not represent a physical process of the modeled turbulence. The second is that the model does not adequately model the boundary layer in the logarithmic layer because the sign of the source term is incorrect. This results in the third derivative term

acting a source, rather sink in this region. These issues led researchers in the abandon this model in favor of other more promising methods, like the $k-\varepsilon$ model [10].

A recent re-evaluation of this model by Menter et. al. was used to develop the SAS model. This is done by first reconsidering the assumption that the third derivative rather than the second is appropriate to use in the production term. While it is true that the integral of the $R_{12}r_y$ is zero for homogenous turbulence, homogenous turbulence occurs only when constant or zero shear exists. In this case the $\frac{\partial^2 \bar{u}(\vec{x})}{\partial y^2}$ and $\frac{\partial^3 \bar{u}(\vec{x})}{\partial^2 y^3}$ are themselves zero and so attempts to evaluate the integral are not relevant.

If however, the expansion of the $\frac{\partial \bar{u}(\vec{x}+r_y)}{\partial y}\int_{-\infty}^{\infty} R_{12}dr_y$ term is considered for inhomogeneous flow (Figure 6-3), the second order term is non-zero and the higher order terms can be neglected.

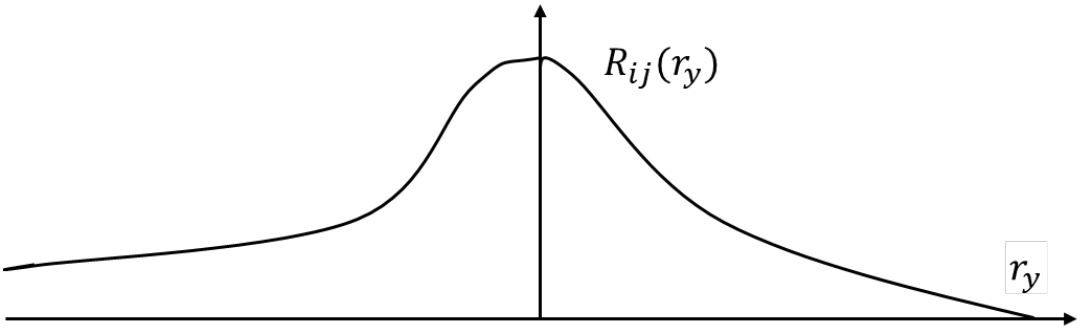

Figure 6-3 Correlation tensor of inhomogenous flow

This alternate approach creates the second order production term where this term is zero under homogeneous flow and non-zero under inhomogeneous flow. This is shown in Equation (60)

$$-\frac{3}{16}\frac{\partial^2\bar{u}(\vec{x})}{\partial y^2}\int_{-\infty}^{\infty}R_{12}r_y dr_y = -const\cdot\overline{u'v'}L^2\left(\frac{1}{\kappa}\frac{\partial^2\bar{u}/\partial y^2}{\partial\bar{u}/\partial y}\cdot L\right) \tag{60}$$

The second order term can then be written as shown in equation (61) and the von Karman length scale is defined in equation (62). P_k is defined as $-\overline{u'v'}\frac{\partial\bar{u}}{\partial y}$

$$-\frac{3}{16}\frac{\partial^2\bar{u}(\vec{x})}{\partial y^2}\int_{-\infty}^{\infty}R_{12}r_y dr_y = -const\cdot P_k\frac{\Psi}{k}\left(\frac{L}{L_{vk}}\right)^2 \tag{61}$$

$$L_{vk} = \kappa\left|\frac{\partial\bar{u}/\partial y}{\partial^2\bar{u}/\partial y^2}\right| \tag{62}$$

With this alternate derivation of the production term, the issue of the incorrect sign in the logarithmic region of the boundary layer is resolved as is its non-physical representation of the physics [10]. The resulting transport equation of Ψ is provided in equation (63).

$$\frac{\partial\Psi}{\partial t}+\bar{u}_j\frac{\partial\Psi}{\partial x_j} = \frac{\Psi}{k}P_k\left(\tilde{\zeta}_1-\tilde{\zeta}_2\left(\frac{L}{L_{vk}}\right)^2\right)-\tilde{\zeta}_3k^{3/2}+\frac{\partial}{\partial y}\left(\frac{\upsilon_t}{\sigma_\Psi}\frac{\partial\Psi}{\partial y}\right) \tag{63}$$

The unique aspect of this model relative to other scale resolving transport equations is the presence of the second velocity derivative in the production term. This term will be activated in locations where second order variation, i.e. local accelerations or deceleration in flow field occurs. As such it is well suited to model unsteady flow where flow separations occur. Elsewhere, the term will be zero.

In the subsequent development of the model, it was deemed appropriate to use this same approach to derive a transport equation for $\sqrt{k}L$, rather than kL. "This change is mainly motivated by practical considerations and a slightly superior performance." [91]

The complete k-$\sqrt{k}L$, generalized for full three-dimensional flow and $\Phi = \sqrt{k}L$ is written as:

$$\frac{\partial(\rho k)}{\partial t} + \bar{u}\frac{\partial(\rho k)}{\partial x_j} = P_k - C_\mu^{3/4} \cdot \rho \frac{k^2}{\Phi} + \frac{\partial}{\partial x_j}\left(\frac{\mu_t}{\sigma_k}\frac{\partial \Phi}{\partial x_j}\right) \tag{64}$$

$$\frac{\partial(\rho\Phi)}{\partial t} + \bar{u}_j\frac{\partial(\rho u_j \Phi)}{\partial x_j} = \frac{\Phi}{k}P_k\left(\zeta_1 - \zeta_2\left(\frac{L}{L_{vk}}\right)^2\right) - \zeta_3\rho k + \frac{\partial}{\partial x_j}\left(\frac{\mu_t}{\sigma_\Phi}\frac{\partial \Phi}{\partial x_j}\right) \tag{65}$$

$$\mu_t = C_\mu^{1/4}\rho\Phi;\ L = \frac{\Phi}{\sqrt{k}}$$

$$L_{vk} = \kappa\left|\frac{U'}{U''}\right|;\ U'' = \sqrt{\frac{\partial^2\bar{u}_i}{\partial^2 x_k}\frac{\partial^2\bar{u}_i}{\partial^2 x_j}};$$

$$U' = S = \sqrt{2S_{ij}S_{ij}};\ S_{ij} = \frac{1}{2}\left(\frac{\partial\bar{u}_i}{\partial x_j} + \frac{\partial\bar{u}_j}{\partial x_i}\right)$$

The von Karman length scale L_{vk} is found from the quotient of the magnitude of the first and second derivative of the velocity field.

This model is referred by the Menter [10] as the KSKL model (K Square root KL) and is a complete model. However, the SAS approach has been further developed to become a modification of the SST model. By transforming the variables and calculating

coefficients, the model can be more directly based on an existing and well tested model while still benefitting from the inclusion of the von Karman length scale is the second equation.

The Φ transport equation can be recast [93] as one for specific dissipation by with $\Phi = C_{\mu}^{-\frac{1}{4}} \frac{k}{\omega}$. This allows the incorporation of the SAS modification into the $k-\omega$ model. With the inclusion of the blending functions, transport equation becomes

$$\frac{\partial(\rho\omega)}{\partial t} + \frac{\partial\left(\rho\bar{u}_j\omega\right)}{\partial x_j} = \alpha\rho S^2 + \tilde{\zeta}_2\kappa\rho S^2\left(\frac{L}{L_{vk}}\right)^2 - \frac{2\rho}{\sigma_\Phi}\frac{k}{\omega^2}\frac{\partial\omega}{\partial x_j}\frac{\partial\omega}{\partial x_j} - \rho\beta\omega^2 + 2(1-F_1)\rho\frac{1}{\sigma_{\omega,2}}\frac{\partial k}{\partial x_j}\frac{\partial\omega}{\partial x_j} + \frac{\partial}{\partial x_j}\left(\mu + \sigma_\omega\mu_t\frac{\partial\omega}{\partial x_j}\right) \tag{66}$$

The SAS terms added to the base SST model can then be grouped as the "Q_{SAS} term" as shown in (67).

$$Q_{SAS} = \kappa\rho S^2\left(\frac{L}{L_{vk}}\right)^2 - \frac{2\rho}{\sigma_\Phi}\frac{k}{\omega^2}\frac{\partial\omega}{\partial x_j}\frac{\partial\omega}{\partial x_j} \tag{67}$$

Some additional modifications are required to the Q_{SAS} term to resolve some final issues. It is important that in areas where the SAS terms is not activated, the model will revert back to the standard SST model. Therefore, a max() function is applied to the Q_{SAS} term to ensure that this term does not become negative. In this case the specific dissipation equation will revert back to the baseline SST model. The second term of the Q_{SAS}

equation becomes a significant contribution in areas where there are significant gradients in the specific dissipation. This typically occurs inside boundary layers. The Q_{SAS} term is then modified to include the gradient of the k field as well through the use of a max() function. This again is included to ensure the performance of the base SST model is preserved and results in the following equation.

$$Q_{SAS} = F_{SAS}\rho max\left[\kappa\eta_2 S^2\left(\frac{L}{L_{vk}}\right)^2 - \frac{2\rho}{\sigma_\Phi}k \cdot \max\left(\frac{1}{\omega^2}\frac{\partial\omega}{\partial x_j}\frac{\partial\omega}{\partial x_j}, \frac{1}{k^2}\frac{\partial k}{\partial x_j}\frac{\partial k}{\partial x_j}\right), 0\right] \quad (68)$$

The F_{SAS} terms is included in the earlier version of the model but is later dropped. When this later portion of the model was first presented [93] a few F_{SAS} terms were attempted, ranging from 1.0 to 1.5 and the value of 1.25 was selected. In later versions [10] the value of 1.0 is used and the F_{SAS} variable is dropped from the expression because of improvements to the calculation of the von Karman length scale which is presented next.

The remaining issue with the SST-SAS model as presented thus far is to ensure proper damping on the higher end of the turbulence spectrum [94] To achieve this, the von Karman length scale is modified to ensure that the smallest scales are dissipated appropriately. This calibration is achieved by calibrating the model coefficients to ensure that the turbulent energy cascade of the model follows the -5/3 slope rule [8]. This approach is often referred to the high wave number damping limiter.

$$L_{vk} = \max\left(\kappa\left(\frac{U'}{U''}\right)^2, C_s\sqrt{\frac{\kappa\eta_2}{\beta/C_\mu - \alpha}}\Delta\right); \Delta = \sqrt[3]{Cell\ Volume} \quad (69)$$

The β and α terms are from the SST model and are calculated with the standard F1 blending function for this model. The full model along with the coefficients used were presented earlier (Sections 2.2.1 and 2.2.2) and will not be restated here.

6.2 Review of recently published work

The Scale Adaptive Simulation [10] has been used in a wide variety of research applications. The SST-SAS model and other variants have been used to evaluate its effectiveness for bluff body flows and has been compared to DES and other turbulence models.

SAS and DES models were used to simulate a NACA0021 airfoil at a high angle of attack as well as a circular cylinder in cross flow[95]. This paper used the same SST-SAS model used in the present study. It was found that the mean flow variables can be predicted well with the SST-SAS model although the turbulence was overpredicted relative to the experimental data in the recirculation bubble. The size of the separation bubble was smaller as a result. This is consistent with the results of the square in cross flow.

SST-SAS and SST-DES models were used to study an AS239 airfoil at a maximum lift condition [96]. The SST-SAS model showed good or better results than DES for pressure coefficients and velocity profiles while avoiding grid induced separation.

The cooling of the trailing edge of a gas turbine blade was modeled with SST-SAS among other URANS methods and compared to experimental data [97]. This study also

compared the URANS SST and SST-SAS models used in the present study relative to PIV experimental measurements. It was found that the SST-SAS model showed a significantly improved prediction of the cooling effectiveness for the SST model. However, the shedding frequency for both models was high relative to the experimental data.

The same square in cross flow case used in this study [80] was also investigated [98] with the KSKL model along with other CFD models. One aspect of this study was to calibrate a coefficient, C_s, to adjust the high wave number damping of the modified von Karman length scale as shown in Equation (70). This is not the same equation used in the SST-SAS model used in the present study and the C_s coefficient does not play the same role in the equation.

$$L_{vk} = \max\left(\kappa \frac{U'}{U''}, C_s \Delta\right) \tag{70}$$

This author used a C_s value of 0.262 based on a study of decaying isotropic turbulence (DIT). It was found that best results were found with the 0.262 value for flow profiles, as well as global quantities like drag and lift coefficients. One conclusion of this study is that a calculation of the C_s coefficient should be based on a calculation from field variables because they found the results to be sensitive to this input. In the present SST-SAS model the C_s coefficient is in fact calculated from field variables as found in equation (69). In the present study, the effective C_s values found from this equation were

0.25 near the wall and 0.19 away from the wall which is close to the previously stated 0.262 value.

6.3 Improvement to the Scale Adaptive Simulation Model

6.3.1 Rationalization for improvement

Review of SST and SST-SAS model results show that the SAS modification does improve that accuracy in some areas of the two cases but makes it worse in others. For the staggered bank (

Figure 6-4 and Table 6-1) the Nusselt number for the front of the tube drops from 330.1 to 274.3 relative to an experimental value of 306.3, effectively over correcting from the higher prediction of the SST model. Along the sides of the center tube, the accuracy is significantly improved with much of the SST-SAS results near or within the margin of error for the experimental data. In the rear portion, the SST-SAS model shows a modest improvement in the local Nusselt number prediction although both model results are approximately 20% lower than the experimental value. For the square in cross flow (Figure 6-5 and Table 6-1) the front of the square Nusselt number results are the same because the Q_{SAS} term is not sufficiently activated to impact the solution. Along the sides, the SST-SAS model shows generally the same results for the first portion of the side (s/D = 0.5 to 1.0) but a significant improvement relative to the SST model along the second portion, from (s/D = 1.0 to 1.3.) On the rear face, the SST model under predicts the mean local Nusselt number and the shape of the CFD results shows a curved profile

while the experimental data is generally flat. In comparison, the SAS model shows a slightly less curved profile but is noticeably lower, further away from the experimental data. The mean Nusselt value for the experimental data on the rear surface is 121.0 relative to 110.2 for the SST and 101.1 for the SST-SAS model. Overall, the mean and local Nusselt numbers are not significantly improved over the SST model and in some areas, are made worse by the SAS modification. This is particularly true at the front of the tube and rear of the square stagnation points when the SAS term is fully activated.

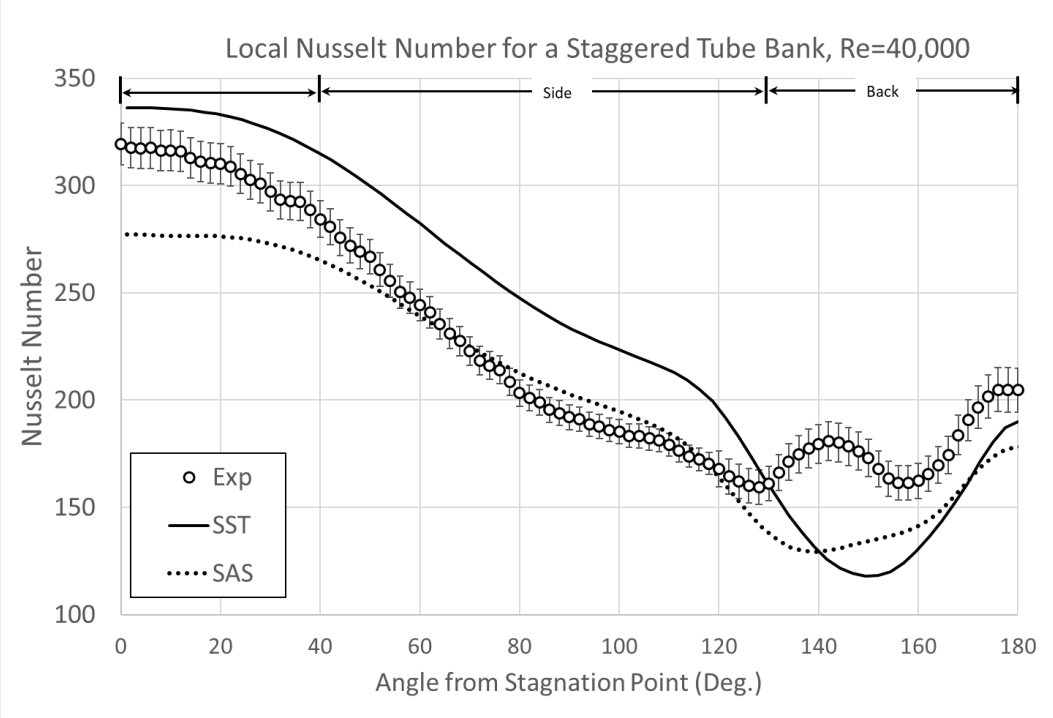

Figure 6-4 Local Nusselt number for staggered tube bank

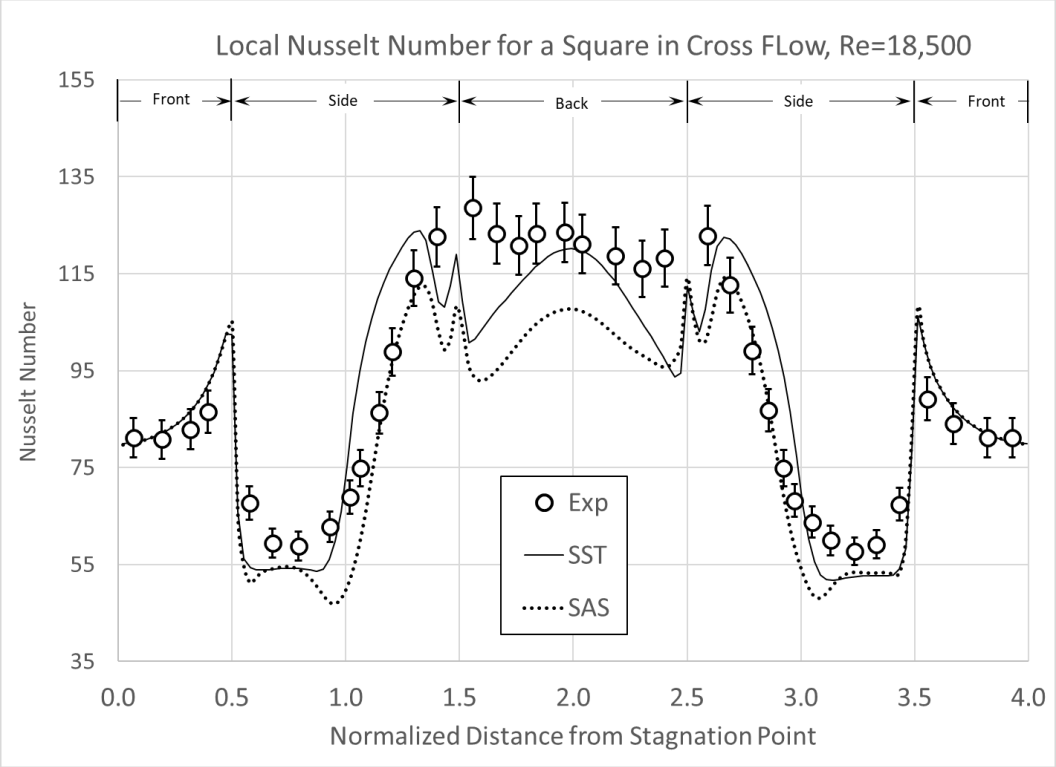

Figure 6-5 Local Nusselt number for square in cross flow

Table 6-1 Mean Nusselt Number results for SST and SAS models

	Staggered Tube Bank				**Square in Cross flow**			
	All	**Front**	**Side**	**Back**	**All**	**Front**	**Side**	**Back**
Experiment	222.4	306.3	207.5	178.8	97.9	87.0	91.6	121.0
SST	234.9	330.1	243.6	143.5	90.6	86.6	82.9	110.2
SAS	207.6	277.1	211.1	145.7	83.6	86.4	73.8	101.1

Reviewing some of the local velocity data at the downstream centerline for both cases (Figure 6-6), the SST-SAS model provides an improved prediction to the x velocity component for the staggered tube bank. With the square in cross flow, the SST model is found to severely under predict the size of the separation bubble with an l_R value of 0.820 relative to an experimental value of 1.38 while the SST-SAS model is an improved 0.977.

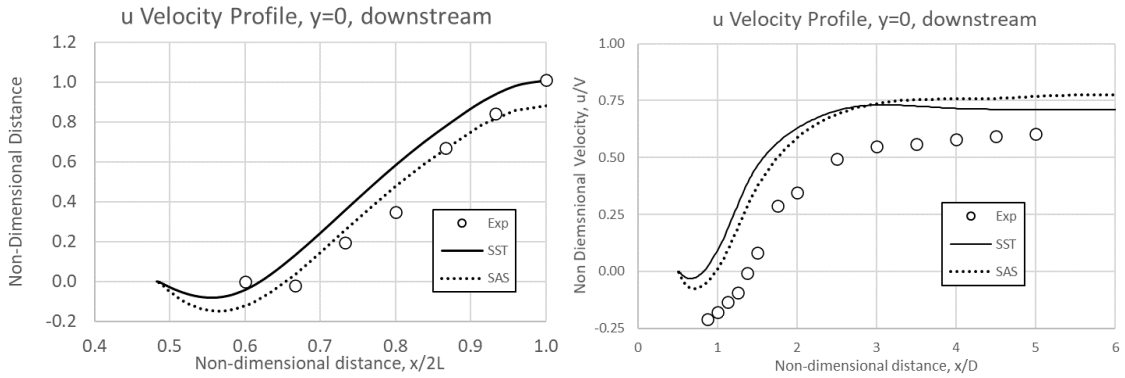

Figure 6-6 Time averaged Velocity profiles for staggered tube bank and square in crossflow for SST and SST-SAS models on y=0 axis, downstream of object

6.3.2 Evaluation of SST-SAS model parameters

To understand the local impact of the Q_{SAS} term modification to the specific dissipation equation, the two constituent parts were evaluated for both cases. Time averaged profiles from the CFD solution were found to determine when the Q_{SAS} term is activated. This allows a detailed understanding of how the SAS modification is behaving for the two cases considered in this study. The Q_{SAS} term contains two main components: a production term and a gradient term as shown in Equation (71).

$$Q_{SAS} = \max\left[\underbrace{\rho\eta_2\kappa S^2\left(\frac{L}{L_{\nu\kappa}}\right)^2}_{\text{Production}} - \underbrace{C\frac{2\rho k}{\sigma_\Phi}\max\left(\frac{1}{\omega^2}\frac{\partial\omega}{\partial x_j}\frac{\partial\omega}{\partial x_j}, \frac{1}{k^2}\frac{\partial k}{\partial x_j}\frac{\partial k}{\partial x_j}\right)}_{\text{Gradient}}, 0\right] \tag{71}$$

These two terms, along with the Q_{SAS} term itself are provided for the staggered tube bank in Figure 6-7 and Figure 6-8 . This data includes a contour plot and profiles from selected locations. The production and gradient terms are temporally and spatially

averaged (in the z-direction) prior to the application of the max() function. Because the max () function introduces a non-linearity, the curves and contour plots will not always show the Q_{SAS} term as a simple subtraction of production term from the gradient term. As a result, the data may appear counterintuitive in some areas.

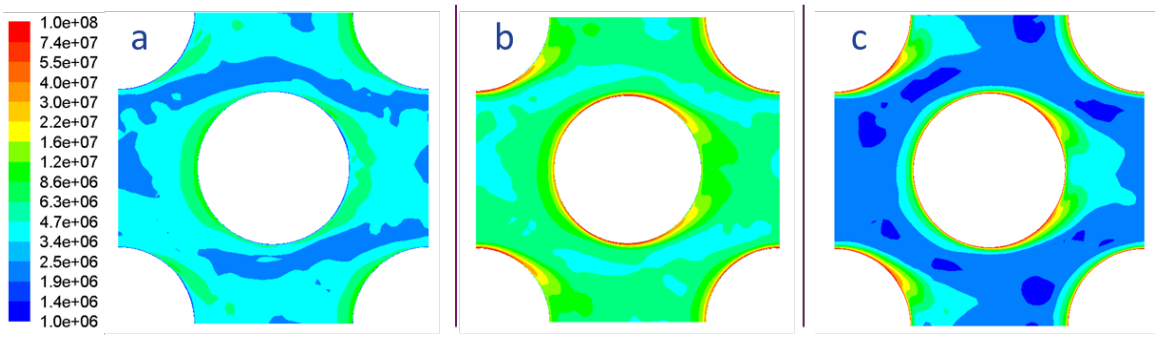

Figure 6-7 Staggered tube bank Q_{SAS} terms for the specific dissipation equation; Q_{SAS}(a) production term (b), and gradient term (c)

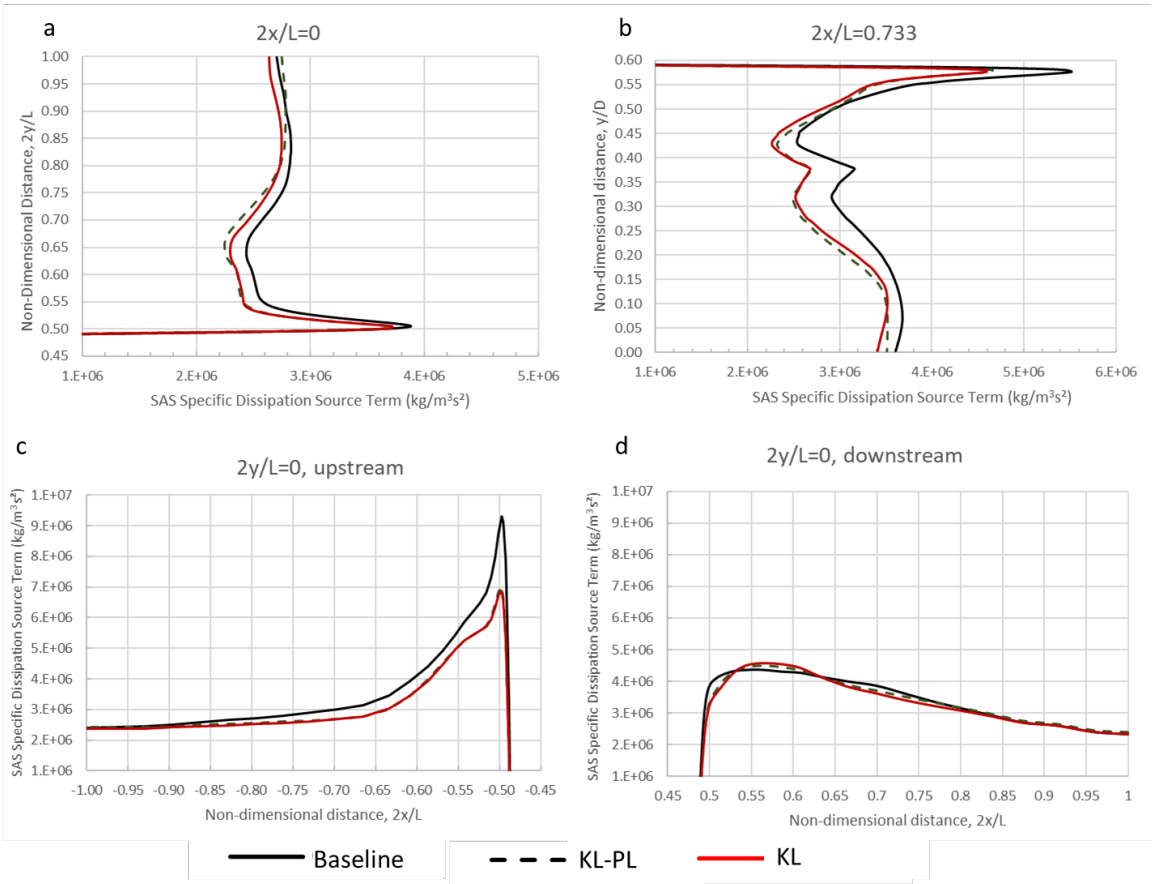

Figure 6-8 Staggered tube bank local distribution of Q_{SAS} terms for the specific dissipation equation; x=0.5 (a), x=0.733 (b),y=0, upstream (c), y=0, downstream (d)

The Q_{SAS} term is generally the same order of magnitude throughout the flow space. The gradient term, while lowering the overall Q_{SAS} value in general, becomes particularly dominant near the wall (a normalized distance < 0.05), and reduces the Q_{SAS} term in this area. This behavior of the gradient term is due to the change in the second derivative terms at the boundary.

The same data from the SST-SAS model for the square in crossflow are provided in Figure 6-9 and Figure 6-10. Insets are provided in Figure 6-9 to provide better detail near the square. These results look significantly different than the staggered tube bank as the

Q_{SAS} term is only activated in the wake region of the square. On the impinging surface, there is some activation of the Q_{SAS} term but it is low enough that is does not significantly impact the solution. This is evidenced by the fact that the SST and SST-SAS model show nearly identical results for the Nusselt number on the upstream impinging surface.

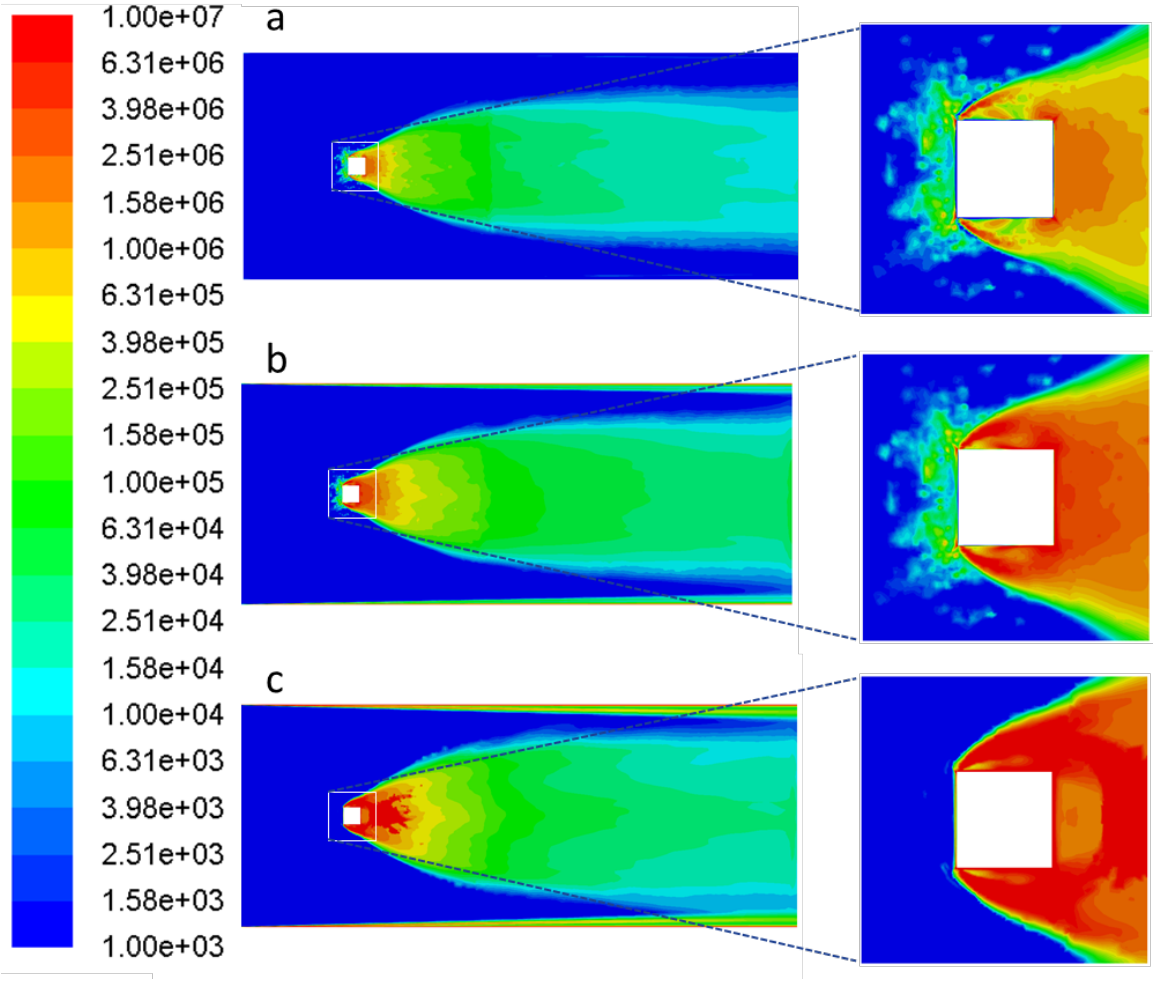

Figure 6-9 Square in cross flow Q_{SAS} terms for the specific dissipation equation; Q_{SAS}(a) production term (b), and gradient term

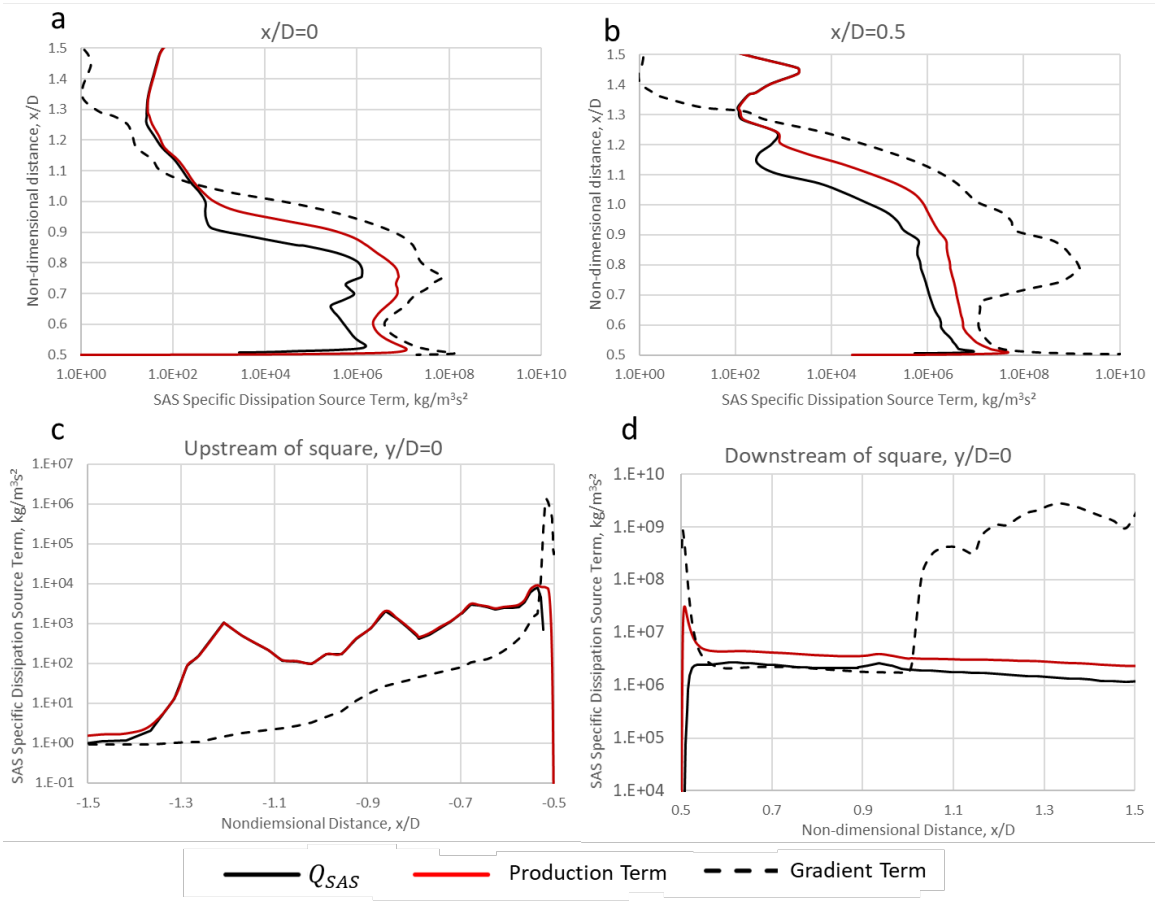

Figure 6-10 Square in cross local distribution of Q_{SAS} terms for the specific dissipation equation: x=0 (a), x=0.5 (b), y=0, upstream of square (c), y=0, downstream of square (d)

The profiles of the Q_{SAS} terms are provided at the square midline, x/D=0 (Figure 6-10a), and at the rear edge of the square at x/D=0.5 (Figure 6-10b). The Q_{SAS} terms at y/D=0 are provided in Figure 6-10c and Figure 6-10d for upstream and downstream of the square, respectively. Outside the detached boundary layer, the production term dominates as the gradient term is a few orders of magnitude smaller. Within the recirculation zone, the gradient term becomes more dominant and reduces the overall Q_{SAS} term. At the center line on the impinging face of the square, the production term dominates until very near the surface due to the small boundary layer in this area as

shown in Figure 6-10d. Overall, the Q_{SAS} term in this area is two orders of magnitude smaller than the sides and rear of the square and the local Nusselt numbers are not noticeably impacted.

On the downstream y/D=0 profile, there are three zones of significance to consider. Near the wall ($0.50 < x/D < 0.55$), the gradient term dominates and significantly reduces the overall Q_{SAS} term as was found in the staggered tube bank. In the next region, slightly away from the wall and to the extending end of the time averaged separation bubble ($0.55 < x/D < 0.95$), the gradient terms is reduced and the Q_{SAS} term is slight larger by about half an order of magnitude (3x). After that, the gradient term again dominates and reduces the Q_{SAS} term.

In summary, the two cases present different conditions to test improvements of the SST model with the Q_{SAS} term modifier. In the staggered tube bank, the Q_{SAS} terms is generally activate throughout the flow space. For the square it is only significant in the separated regions and wake areas.

6.3.3 Schemes to improve the accuracy of the SST-SAS model for the present cases

There a number of observations that can be made for the SST and SST-SAS results for the staggered tube bank and the square in cross flow. These include:

1. The SST-SAS shows decreased accuracy relative the SST model on the upstream impinging face of the staggered tube bank and the rear face of the square in cross flow.
2. In both of these locations the SST-SAS model over corrects the SST solution.
3. The SST-SAS model shows an improvement on the side face of both objects.

One conclusion from these observations is that the accuracy of the local Nusselt numbers might be improved by reducing the impact of the SAS modifications at locations where the SST-SAS model provides worse results than the SST model. By dialing-back the Q_{SAS} term in this area it is hoped that the accuracy would be improved while not losing the improvements in accuracy along the sides of the object.

Reviewing the SST-SAS specific dissipation transport equation, the production term can be written without the modification for the gradient terms as

$$P_\omega = \alpha\rho S^2 + \eta_2\kappa\rho S^2\left(\frac{L}{L_{vk}}\right)^2 \tag{72}$$

The production of the specific dissipation can also be rewritten in terms of the production to the turbulent kinetic energy based on the relation $P_k = \mu_t S^2$

$$P_\omega = \alpha\rho\left(\frac{P_k}{\mu_t}\right) + \eta_2\kappa\rho\left(\frac{P_k}{\mu_t}\right)\left(\frac{L}{L_{vk}}\right)^2 \tag{73}$$

As noted in item 1 in the list above, the accuracy of the SST-SAS model is noticeably poorer at stagnation points on the object where the Q_{SAS} term is activated. Rewriting

Equation (72) to include the P_k term in equation (73) allows the use of alternate expressions for P_k to limit excessive production at stagnation points that have been developed previously.

There are two well-known methods to modify P_k. These are the Kato-Launder modification [45], shown in Equation (74) and production limiter [44] shown in Equation (75) . These modifications can be used separately or together as show in Equation (76). Both modifications have been used together for the SST and the PANS-SST models used in this study. In addition, they have been used for the non-Q_{SAS} terms of the SST-SAS model. A value for C_{lim} of 10 is typically used.

$$\tilde{P}_k = \mu_t \Omega S \tag{74}$$

$$\tilde{P}_k = \min(\mu_t S^2, C_{lim}\beta^* k\omega) \tag{75}$$

$$\tilde{P}_k = \min(\mu_t \Omega S, C_{lim}\beta^* k\omega) \tag{76}$$

These modifications have been shown to prevent the excessive turbulence production (and heat transfer) at a stagnation point. Reviewing Equation (73), it is clear that a reasonable approach for reducing the Q_{SAS} term at stagnations points would be to introduce the Kato Launder and production limiter into the Q_{SAS} term as shown in Equation (77).

$$Q_{SAS} = \max\left[\rho\eta_2\kappa\left(\frac{\tilde{P}_k}{\mu_t}\right)\left(\frac{L}{L_{\nu\kappa}}\right)^2 - C\frac{2\rho k}{\sigma_\Phi}\max\left(\frac{1}{\omega^2}\frac{\partial\omega}{\partial x_j}\frac{\partial\omega}{\partial x_j}, \frac{1}{k^2}\frac{\partial k}{\partial x_j}\frac{\partial k}{\partial x_j}\right), 0\right] \quad (77)$$

This would be an improvement of the SST-SAS model that is dependent on field variables and does not modify the model coefficients. The intent of the modification is to improve the accuracy of the SST-SAS model where separated flow has occurred and the flow is impinging on a surface. This condition was found on the upstream surface of the tube in the staggered tube bank as well as the rear of the square in cross flow.

6.3.4 Results of improvement

Both geometric cases were run with the Kato-Launder modification and the Kato-Launder modification with the production limiter. These will be referred to as the KL and KL-PL modifications, respectively. A modest improvement is found with the KL modification on the rear face of the square in cross flow as shown in Figure 6-12. A smaller improvement is found near the rear of the tube in the staggered tube bank as shown in Figure 6-11 for the KL-PL variant. The mean Nusselt number results by side of the object are provided for the two proposed modifications in Table 6-2 for the staggered tube bank and in Table 6-3 for the square in cross flow.

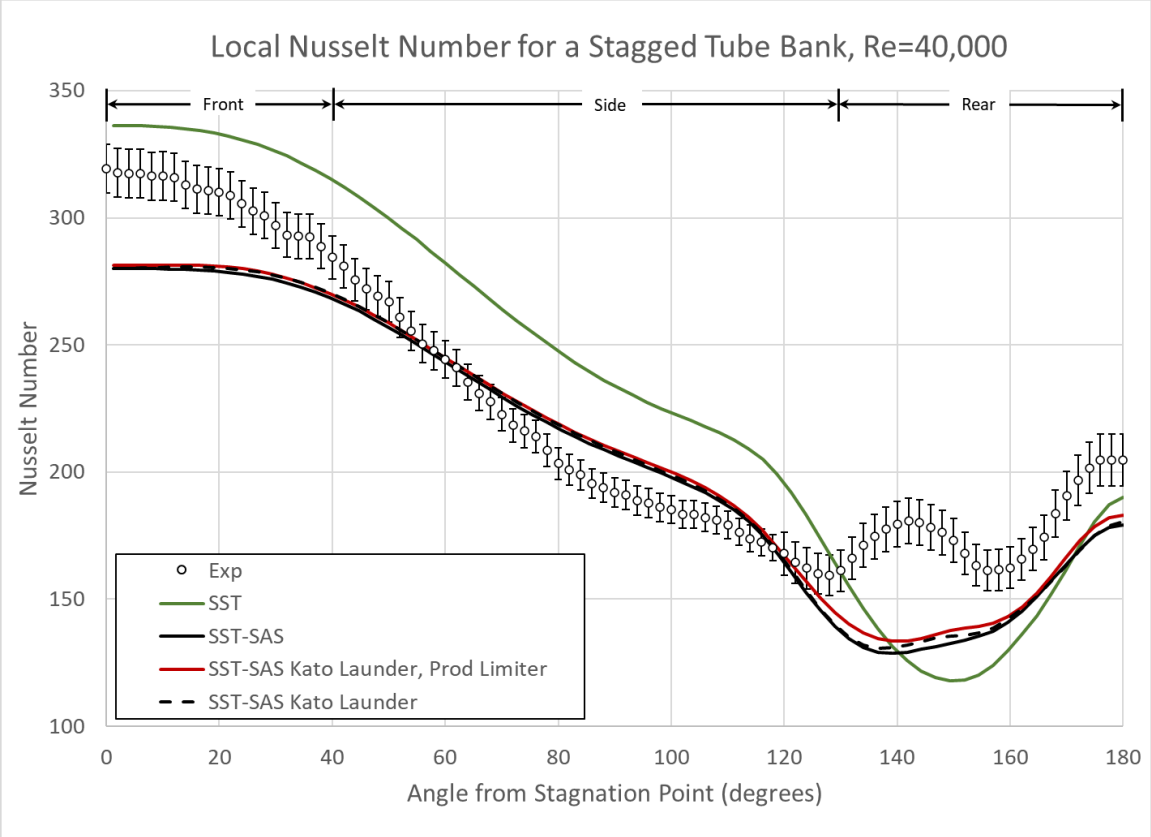

Figure 6-11 Impact of improvements to the SST-SAS model due to addition of Kato-Launder and production limiters and Q_{SAS} term.

Table 6-2 Local Nusselt Number statistics of improved SAS variants

	Nusselt Number				% Error from experiment			
Model	**All**	**Front**	**Sides**	**Back**	**All**	**Front**	**Sides**	**Back**
Exp/ error	222.4	306.3	207.5	178.8	+/- 3%	+/- 3%	+/- 3%	+/- 5%
SST	234.9	330.1	243.6	143.5	5.6%	7.8%	17%	-20%
SST-SAS	207.6	277.1	211.1	145.7	-6.7%	-9.5%	1.7%	-19%
SST-SAS-KL	208.8	278.3	212.3	146.9	-6.1%	-9.1%	2.3%	-18%
SST-SAS-KL-PL	210.1	278.8	213.3	149.5	-5.6%	-9.0%	2.8%	-16%

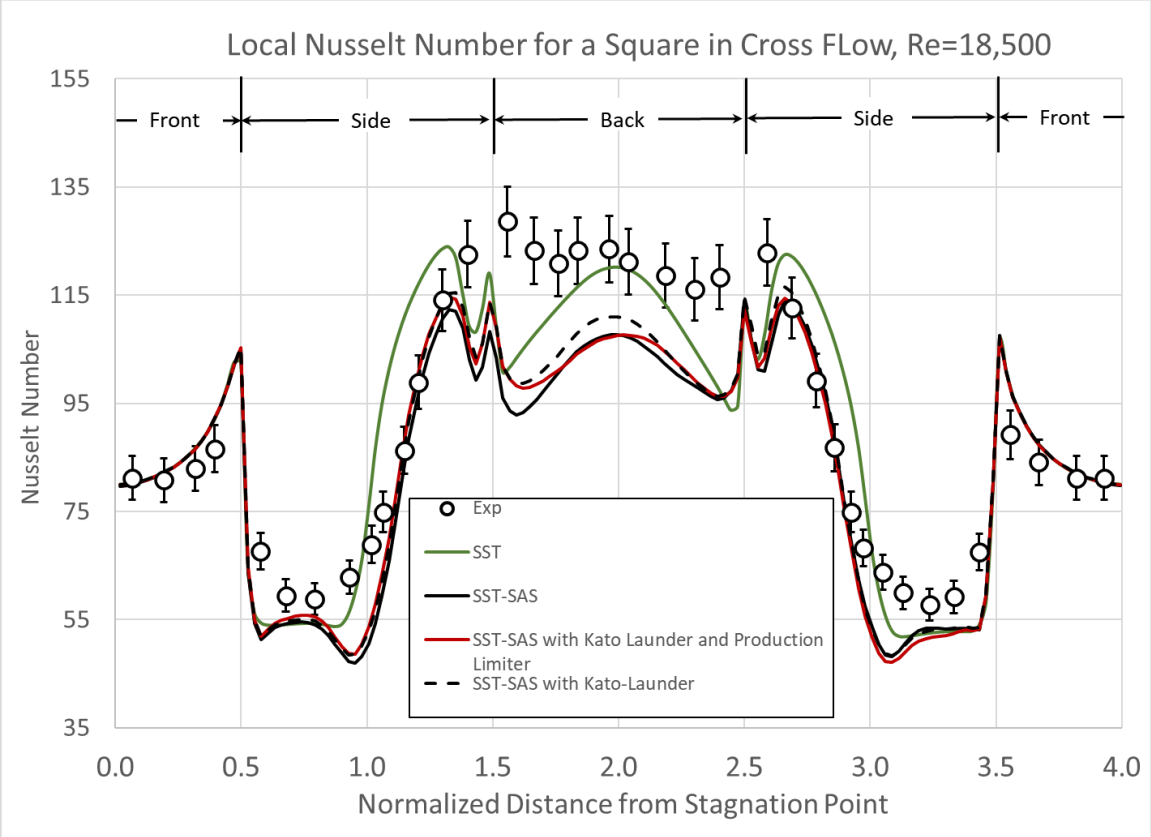

Figure 6-12 Results of baseline models and improved SST-SAS model for Local Nusselt number for the square in cross flow

Table 6-3 Mean results of baseline models and improved SST-SAS model for square in cross flow

	Nusselt Number				Error			
Case	**All**	**Front**	**Sides**	**Back**	**All**	**Front**	**Sides**	**Back**
Experiment	97.9	87.0	91.6	121.0	5.0%	5.0%	5.0%	5.0%
SST	90.6	86.6	82.9	110.2	-7.5%	-0.5%	-9.6%	-8.9%
SST-SAS	83.8	86.7	73.8	101.1	-14.4%	-0.4%	-19.5%	-16.5%
SST-SAS-KL	85.3	86.8	75.2	104.1	-12.9%	-0.3%	-17.9%	-14.0%
SST-SAS-KL-PL	84.6	86.7	74.6	102.5	-13.6%	-0.4%	-18.6%	-15.3%

For the staggered tube bank the local Nusselt numbers for the KL-PL modification showed the most notable improvement near 140° from the stagnation point. Elsewhere the results are similar to the baseline SST-SAS model in shape. Reviewing the overall

mean Nusselt number values in the summary table, the change from the improvement is on the order of ~1% or less except for the rear. On the rear portion of the tube the KL-PL modification showed an increase in the mean Nusselt number from 145.7 to 149.5, a 3.4% percent improvement in the accuracy in this area relative to the experimental data. The KL modification also saw an improvement but the change was only 2%. Overall, to the mean and local Nusselt number changes were not significant.

For the square in cross flow, the impact is not dramatic but they are more significant than the results from the staggered tube bank. Notably, the KL modification did have a modest impact on the local Nusselt numbers at the rear of the square. Specifically, the mean Nusselt number increased from 101.1 for the baseline SST-SAS model to 104.1 for the KL variation. The experimental value in this location is 121.0. The KL variation shows a small improvement on the sides, decreasing the mean error for those surfaces from -19.5% to -17.9, a change of 1.6%. One unfortunate result from this analysis is that while the Kato-Launder modification alone showed a benefit on the rear surface of the square, the improvement (however small) for the staggered tube bank was found for the combined Kato-Launder and production limiter case. This lessens the value of this improvement.

Another observation from the results on the rear face of the square in cross flow is that none of the changes shows a positive impact of the shape of the profile on the rear face. The same downward profile is found for all cases while the experimental data is

essentially flat. Finally, neither of the modifications had a negative impact on the accuracy of the Nusselt numbers relative to the baseline SST-SAS model.

The Q_{SAS} profiles for the staggered tube bank and square in cross flow are shown in Figure 6-13 and Figure 6-14 for the three model variations. When reviewing this data, it is important to bear in mind that the values plotted are the source terms for the specific dissipation transport equation. As such, convection and diffusion will spread the Q_{SAS} production beyond the local area. While the Q_{SAS} term was reduced in the expected areas, the reduction was too small to significantly impact the solution results as already discussed.

On the upstream face of the staggered tube bank at 2y/L=0, (Figure 6-13c), the sides at 2x/L=0 and (Figure 6-13a) and at 2x/L=0.733 (Figure 6-13b), both the KL and KL-PL provide a reduction in the Q_{SAS} term. In the rear section (Figure 6-13d), the profiles are the same as the baseline model.

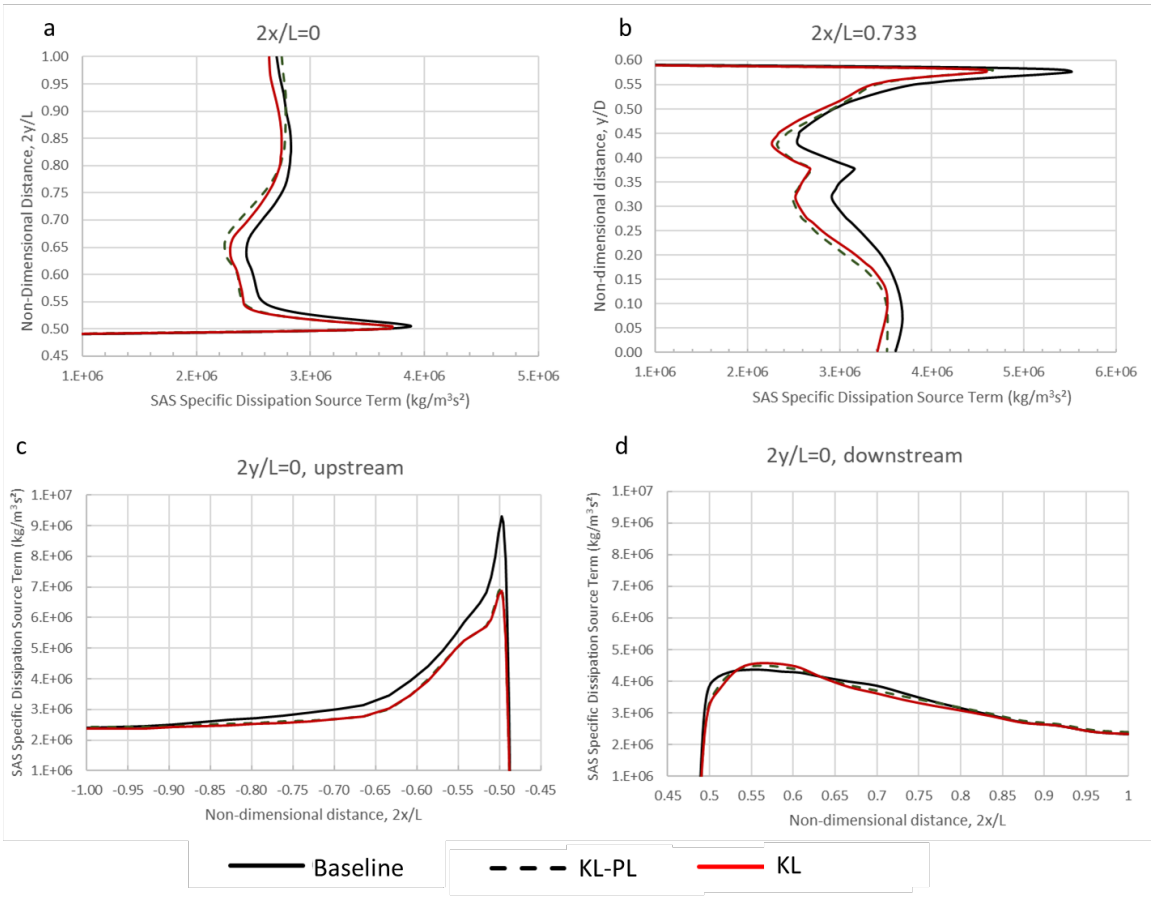

Figure 6-13 Impact of alternate production methods on Q_{SAS} term for staggered tube bank at 2x/L=0 (a), 2x/L=0.733, 2y/L=0 upstream (c), 2y/L=0 downstream (d)

The reduction in the Q_{SAS} term does generally occur on the front face of the tube where the SAS modification over corrects the SST model. As such, it would be expected to improve the accuracy of the local Nusselt number. However, the magnitude for the reduction is apparently too small to impact the Nusselt number results in this area as shown in Figure 6-11.

The Q_{SAS} terms for the square in cross flow are similar to the staggered tube bank in that there are only small changes to this term for the KL and KL-PL variants. The Q_{SAS} term is two orders of magnitude lower upstream of the square along the y/D=0 line (c) than at

the other locations. At x/D = 0 (Figure 6-14a)and x/D = 0.5 (Figure 6-14b) both the KL and KL-PL variants are actually larger the than the baseline Q_{SAS} value. At y/D = 0 (Figure 6-14d) on the downstream side of the square, KL variants is slightly lower than the baseline and the KL-PL case.

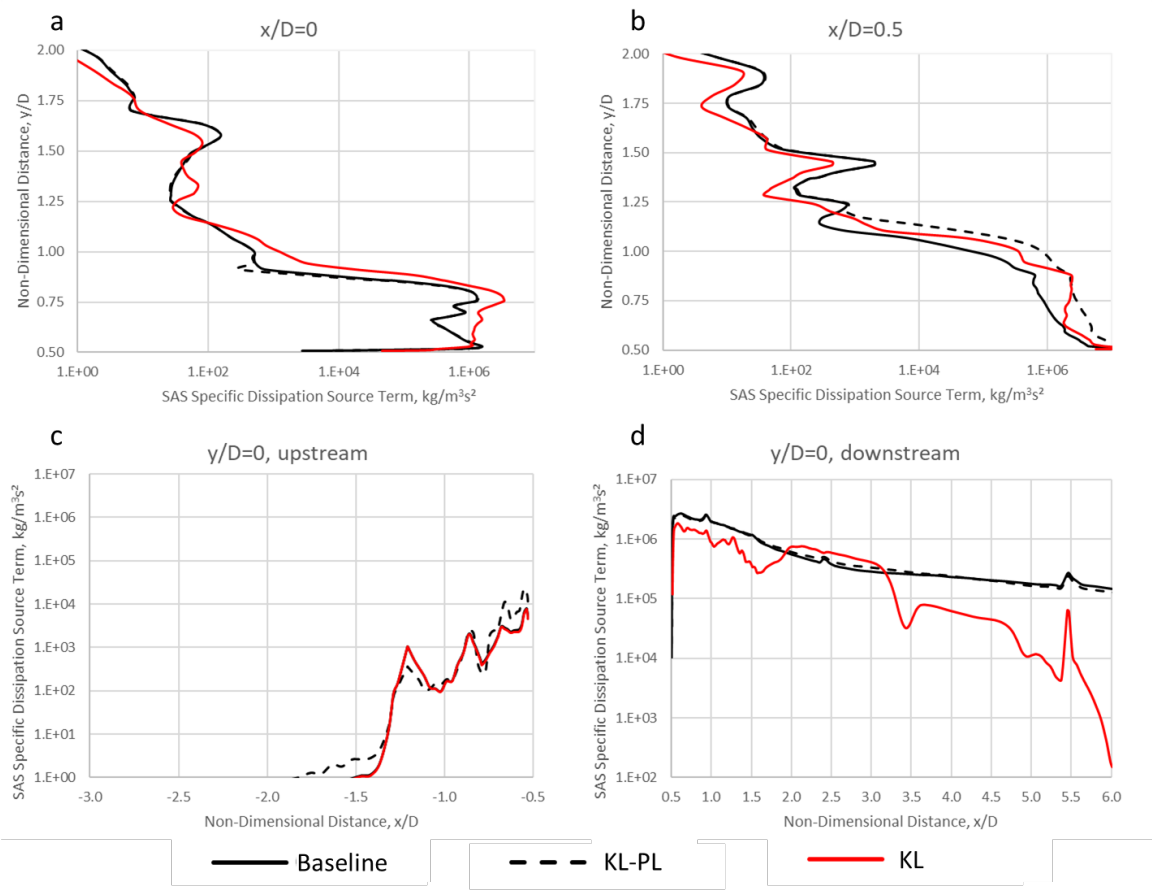

Figure 6-14 Impact of alternate production terms on Q_{SAS} terms for square in cross flow at x/D=0 (a), x/D=0.5 (b), y/D= 0 upstream (c), y/D=0, downstream (d)

A sample of the velocity, effective thermal conductivity and Reynolds stresses for these cases for the staggered tube bank and the square in cross flow are shown in Figure 6-15 through Figure 6-18. Review of the profiles does not show much variation in the profiles for the three SAS models.

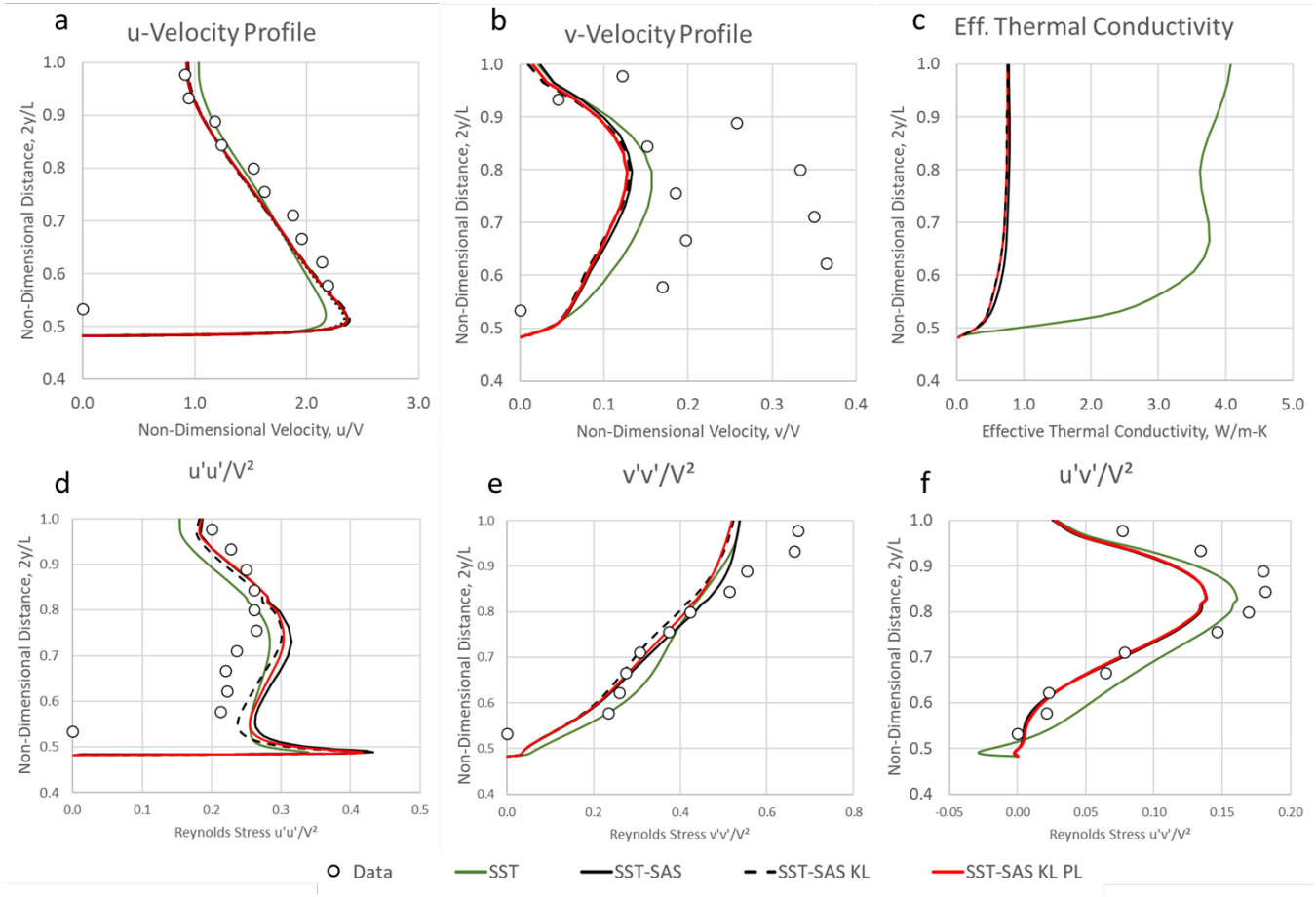

Figure 6-15 Profiles at x=0 in staggered tube bank for SAS improvement with Kato-Launder and Kato-Launder/ Production Limiter; non dimensional u-velocity (a), non-dimensional v-velocity (b), effective thermal conductivity (c) Reynolds stresses $\overline{u'u'}/V^2$ (d), $\overline{v'v'}/V^2$ (e), $\overline{u'v'}/V^2$ (f)

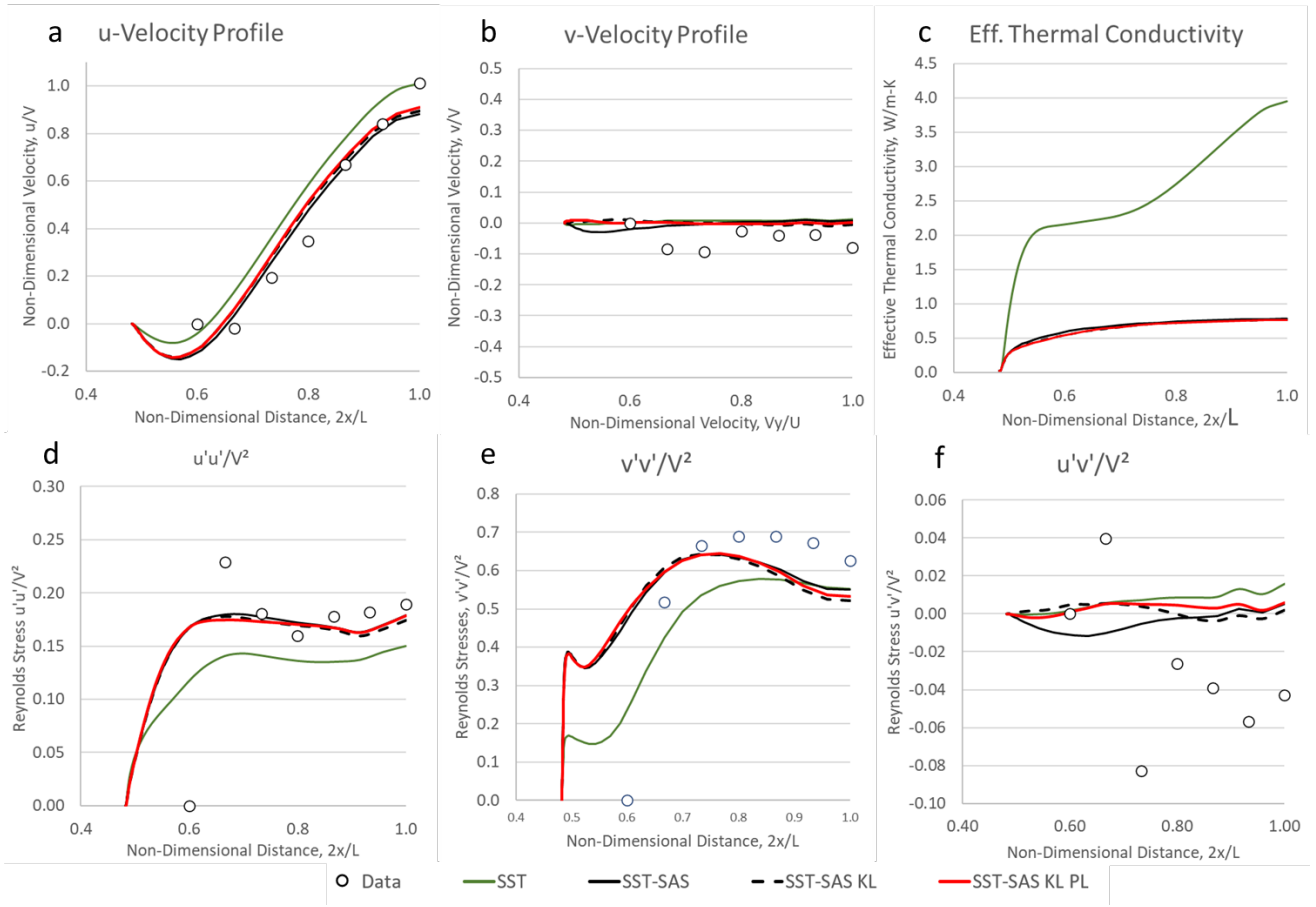

Figure 6-16 Profiles at y=0 in staggered tube bank for SAS improvement with Kato-Launder and Kato-Launder/ Production Limiter; non dimensional u-velocity (a), non-dimensional v-velocity (b), effective thermal conductivity (c) Reynolds stresses $\overline{u'u'}/V^2$ (d), $\overline{v'v'}/V^2$ (e), $\overline{u'v'}/V^2$ (f)

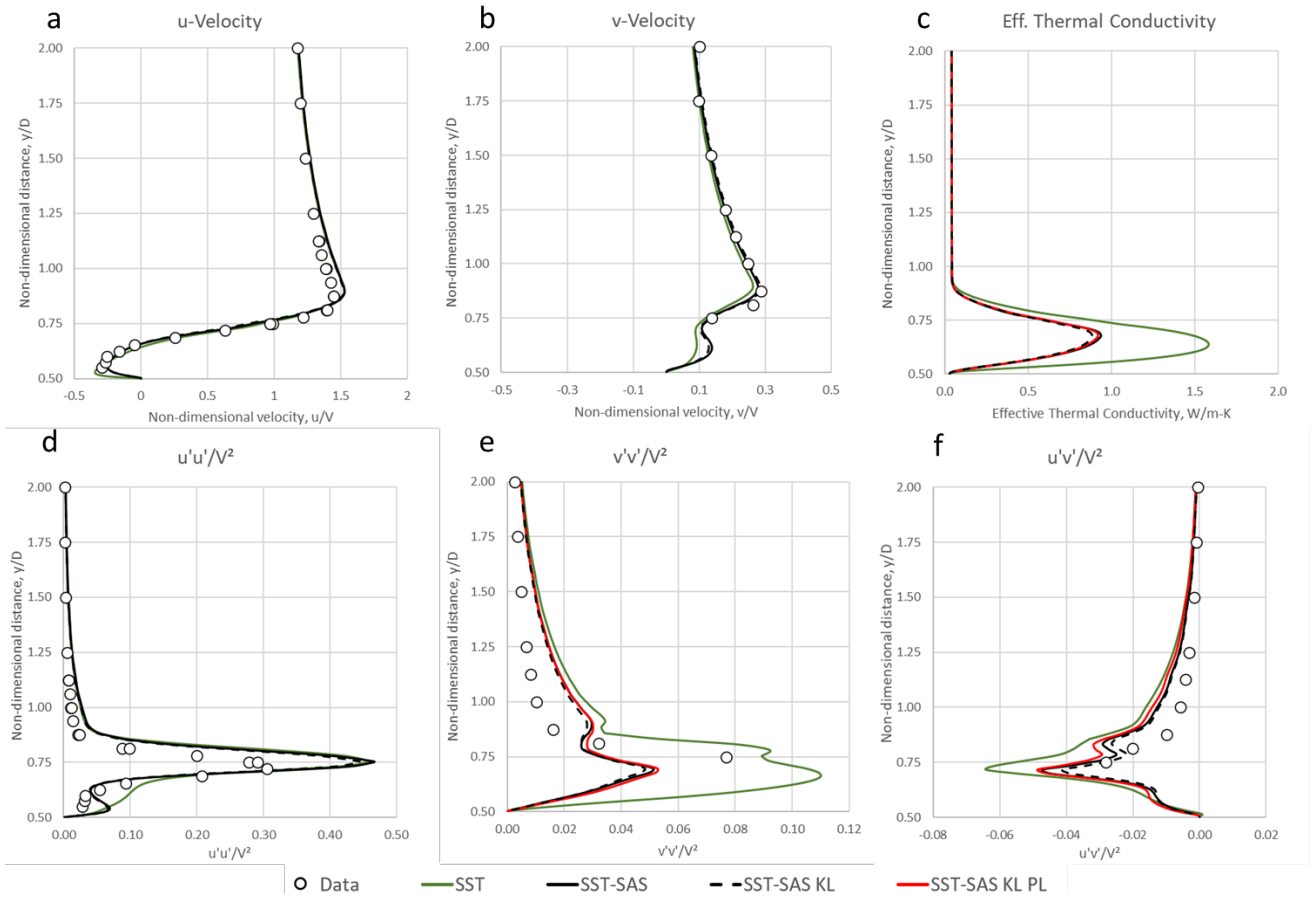

Figure 6-17 Profiles at x=0 for Velocity, effective thermal conductivity and Reynolds stresses for square in cross flow for SAS improvement with Kato-Launder and Kato-Launder/ Production Limiter Modification; u-velocity(a), v-velocity (b), effective thermal conductivity (c), normalized Reynolds stresses $\overline{u'u'}$/V² (d), $\overline{v'v'}$/V² (e), and $\overline{u'v'}$/V² (f)

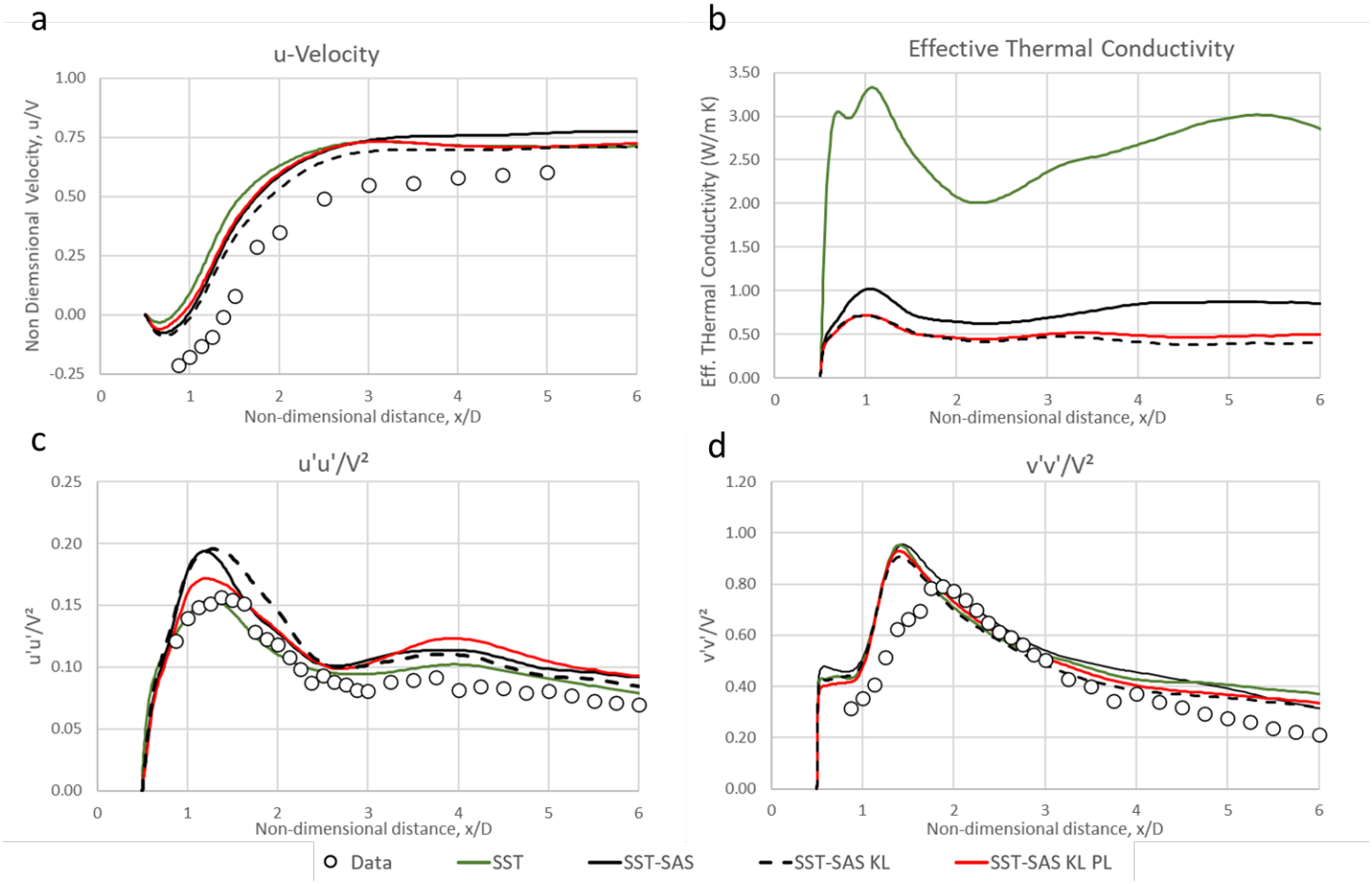

Figure 6-18 Profiles at y=0 for Velocity, effective thermal conductivity and Reynolds stresses for square in cross flow for SAS improvement with Kato-Launder and Kato-Launder/ Production Limiter Modification; u-velocity(a), effective thermal conductivity (b), normalized Reynolds stresses $\overline{u'u'}$/V² (c), $\overline{v'v'}$/V² (d)

The only variation of significance is the reduction of the effective thermal conductivity for both the KL and KL-PL modifications behind that square as shown in Figure 6-18b. This reduction would indicate an increase is the resolved turbulent energy in this area despite the fact that the Q_{SAS} terms was reduced in this area. The reason for this change is not readily apparent. The slight changes in the Reynolds stresses downstream of the square shown in Figure 6-18c and Figure 6-18d are not considered to be significant.

6.4 Conclusions for attempted improvement to the SST-SAS model

In this study, the SAS modification of the SST turbulence model was found to increase the accuracy of the CFD prediction relative to the experimental value is some areas while causing an increase in the errors in others. The specification locations where the SST-SAS model was less accurate than the SST model are at the stagnation points in the front face of the tube and the rear of the square in cross flow. The novel improvement of the SAS model presented here was intended to reduce the Q_{SAS} term in areas where it is activated by using existing methods to reduce the production term at the stagnation point. While the reduction of the local Q_{SAS} values was found, the modifications showed limited improvement for the cases considered in this study.

Despite the limited success found in this study, further modifications the SAS terms may enable the KL-PL or KL modification be more effective. Alternate approaches to improving this model might include adjusting the model coefficients, including the F_{SAS} term used in the earlier version of the model that more directly controlled the magnitude

of the SAS modification. Adjustments limits to the von Karman length scale as shown in Equation (69) could also be considered. Namely, an alternate definition of this length scale could be pursued in the near wall region to provide better heat transfer performance while not deviating significantly correct high wave number damping.

One benefit from this work is to document an approach that did not work to guide future researchers to pursue more fruitful improvements to the Scale Adaptive Simulation method.

7 CONCLUSION

The first part of this study evaluated six CFD models against two sets of experimental data available in the literature. It was found that the more sophisticated models did not necessarily provide better results. In particular, the level of resolved turbulence did not correlate directly to the accuracy of the mean and local Nusselt numbers. It is clear that the degree of resolved turbulence determined by the model must also work effectively with the turbulent viscosity model. For the industrial user, this comparative study shows that while significant gains are available by simple transitioning from a SRANS to a URANS solution, there can be significant variability in the models.

The SST-SAS and PANS-SST both attempt to reduce the modeled turbulence by increasing the local specific dissipation. Despite the elegance of the baseline SST-SAS model, it does not provide an overall improvement compared the baseline SST model. The PANS-SST model was cumbersome to implement but was found to provide an excellent improvement over the SST model.

The attempt to improve the SST-SAS model was only marginally successful. While the results for the staggered tube bank and square in crossflow did show an opportunity for improvement, the benefits of the modification were marginal. Regardless, these results may provide future researchers an opportunity to find complementary changes to these improvements that will make them more effective.

8 REFERENCE LIST

[1] Wilcox, D. C., 2006, Turbulence modeling for CFD, DCW industries La Canada, CA.
[2] Launder, B. E., and Spalding, D. B., 1974, "Numerical Computations for Turbulent Flows," Computer Methods in Applied Mechanics and Engineering, 3(2), pp. 269-289.
[3] Orszag, S. A., Yakhot, V., Flannery, W. S., Boysan, F., Choudhury, D., Maruszewski, J., and Patel, B., "Renormalization group modeling and turbulence simulations," Proc. Proceedings of the International Conference on Near- Wall Turbulent Flows, Mar 15 - 17 1993, Publ by Elsevier Science Publishers B.V., pp. 1031-1031.
[4] Menter, F., Kuntz, M., and Langtry, R., 2003, "Ten years of industrial experience with the SST turbulence model," Turbulence, heat and mass transfer, 4(1).
[5] Lodefier, K., 2004, "Transition modelling with the k-omega; turbulence model and an intermittency transport equation," Journal of thermal science, 13(3), pp. 220-225.
[6] Walters, D. K., and Cokljat, D., 2008, "A three-equation eddy-viscosity model for reynolds-averaged navier-stokes simulations of transitional flow," Journal of Fluids Engineering, Transactions of the ASME, 130(12), pp. 1214011-12140114.
[7] Sagaut, P., 2006, Large eddy simulation for incompressible flows: an introduction, Springer Science & Business Media.
[8] Pope, S. B., 2000, "Turbulent flows, Cambridge Univ," Press, Cambridge.
[9] Girimaji, S. S., "Partially-averaged navier-stokes model for turbulence: A reynolds-averaged navier-stokes to direct numerical simulation bridging method," American Society of Mechanical Engineers, pp. 413-421.
[10] Menter, F. R., and Egorov, Y., 2010, "The scale-adaptive simulation method for unsteady turbulent flow predictions. part 1: Theory and model description," Flow, Turbulence and Combustion, 85(1), pp. 113-138.
[11] Egorov, Y., Menter, F. R., Lechner, R., and Cokljat, D., 2010, "The scale-adaptive simulation method for unsteady turbulent flow predictions. part 2: Application to complex flows," Flow, Turbulence and Combustion, 85(1), pp. 139-165.
[12] Hanjalic, K., 2005, "Will RANS Survive LES? A View of Perspectives," Journal of Fluids Engineering, 127(5), pp. 831-839.
[13] Commission, I. E., 2004, "Rotating Electrial Machines," IEC, Geneva, Switzerland.
[14] Hettegger, M., Reinbacher-Kostinger, A., and Biro, O., "Characterizing the convective wall heat transfer on convoluted shapes in the end-region of an induction machine," Proc. 2012 20th International Conference on Electrical Machines, ICEM 2012, September 2, 2012 - September 5, 2012, IEEE Computer Society, pp. 1219-1226.
[15] Hettegger, M., Streibl, B., Biro, O., and Neudorfer, H., "Characterizing the heat transfer on the end-windings of an electrical machine for transient simulations," Proc. 15th IEEE Mediterranean Electrotechnical Conference, MELECON 2010, April 25, 2010 - April 28, 2010, Institute of Electrical and Electronics Engineers Inc., pp. 581-586.
[16] Hettegger, M., Streibl, B., Biro, O., and Neudorfer, H., "Identifying the heat transfer coefficients on the end-windings of an electrical machine by measurements and

simulations," Proc. 19th International Conference on Electrical Machines, ICEM 2010, September 6, 2010 - September 8, 2010, IEEE Computer Society.
[17] Hettegger, M., Streibl, B., Biro, O., and Neudorfer, H., "Measurements and simulations of the convective heat transfer coefficients on the end windings of an electrical machine," Institute of Electrical and Electronics Engineers Inc., pp. 2299-2308.
[18] Hettegger, M., Streibl, B., Biro, O., and Neudorfer, H., "Measurements and simulations of the heat transfer on end windings of an induction machine," Emerald Group Publishing Ltd., pp. 1727-1736.
[19] Luke, G. E., 1923, "The cooling of electric machines," American Institute of Electrical Engineers -- Journal, 42(12), pp. 1278-1288.
[20] Micallef, C., 2006, "End Winding Cooling in Electric Machines."
[21] Schleussinger, A., Weickenannt, A., and Arndt, A., 2005, "Heat Transfer Measurements on Crossing Banks of Nonciruclar Bars in Cross Flow," 6th World Conference on Experimental Heat Transfer , Fluid Mechanics and Thermodynamics.
[22] Administration, U. S. E. I., 2013, "International Engergy Statistics," Department website and data base.
[23] Anacona, D., and McVeigh, J., 2001, "Wind Turbine - Materials and Mancufacturing Fact Sheet," US Department of Energy, Office of Industrial Technologies.
[24] Zukauskas, A., Ulinskas, R., and Daunoras, P., 1985, "Influence of surface roughness on the heat transfer and drag of tube banks in crossflow," Heat and Technology, 3(2), pp. 1-46.
[25] Zukauskas, A., and Ulinskas, R., 1988, Heat transfer in tube banks in crossflow.
[26] Zhukauskas, A. A., Ulinskas, R. V., and Martsinauskas, K. F., 1977, "Influence of the geometry of the tube bundle on the local heat transfer rate in the critical region of streamline flow," International Chemical Engineering, 17(4), pp. 744-751.
[27] Zdravistch, F., 1995, "Numerical laminar and turbulent fluid flow and heat transfer predictions in tube banks," International Journal of Numerical Methods for Heat & Fluid Flow, 5(8), pp. 717-733.
[28] Pierson, O. L., 1937, "Experimental Investigation of the Influence of Tube Arrangement on Convection Heat Transfer and Flow Resistance in Cross Flow of Gases Over Tube Banks," American Society of Mechanical Engineers -- Transactions, 59(7), pp. 563-572.
[29] Ishigai, S., and Nishikawa, E., 1975, "Experimental study of structure of gas flow in tube banks with tube axes normal to flow - 2. On the structure of gas flow in single-column, single-row, and double-rows tube banks," Bulletin of the JSME, 18(119), pp. 528-535.
[30] Aiba, S., Tsuchida, H., and Ota, T., 1983, "Heat transfer around a tube in a staggered tube bank," Heat Transfer - Japanese Research, 12(1), pp. 1-18.
[31] Wilson, B. M., Smith, B. L., and Spall, R. E., 2012, "Examples of unsteady CFD validation system response quantities in a cylinder array," Nuclear Engineering and Design, 243, pp. 153-167.

[32] Paul, S. S., Ormiston, S. J., and Tachie, M. F., 2008, "Experimental and numerical investigation of turbulent cross-flow in a staggered tube bundle," International Journal of Heat and Fluid Flow, 29(2), pp. 387-414.
[33] Li, X., Wu, X., and He, S., 2014, "Numerical investigation of the turbulent cross flow and heat transfer in a wall bounded tube bundle," International Journal of Thermal Sciences, 75, pp. 127-139.
[34] Konstantinidis, E., Balabani, S., and Yianneskis, M., 2002, "A study of vortex shedding in a staggered tube array for steady and pulsating cross-flow," Journal of Fluids Engineering, Transactions of the ASME, 124(3), pp. 737-746.
[35] Johnson, R. W., 2005, Validation Studies for Numerical Simulations of Flow Phenomena Expected in the Lower Plenum of a Prismatic VHTR Reference Design, Idaho National Laboratory.
[36] Shaukatullah, H., Gaynes, M. A., and White, L. H., "Thermal enhancement of surface mount electronic packages with heat sinks," Proc. Electronic Components and Technology Conference, 1993. Proceedings., 43rd, pp. 256-263.
[37] Han, J.-C., Dutta, S., and Ekkad, S., 2012, Gas turbine heat transfer and cooling technology, CRC Press.
[38] Bejan, A., 1984, Convection heat transfer, John wiley & sons.
[39] John D Anderson, J., Computational Fluid Dynamics: The Basics wtih Applications, McGraw-Hill, New York.
[40] Tennekes, H., Lumley, J. L., and Lumley, J., 1972, A first course in turbulence, MIT press.
[41] Kays, W. M., Crawford, M. E., and Weigand, B., 2012, Convective heat and mass transfer, Tata McGraw-Hill Education.
[42] Lilly, D. K., 1992, "A proposed modification of the Germano subgrid-scale closure method," Physics of Fluids A: Fluid Dynamics (1989-1993), 4(3), pp. 633-635.
[43] Menter, F. R., 1993, "Zonal two equation k-turbulence models for aerodynamic flows," AIAA paper, 2906, p. 1993.
[44] Menter, F. R., 1994, "Two-equation eddy-viscosity turbulence models for engineering applications," AIAA journal, 32(8), pp. 1598-1605.
[45] Launder, B. E., and Kato, M., "Modelling flow-induced oscillations in turbulent flow around a square cylinder," Proc. Proceedings of the Fluids Engineering Conference, June 20, 1993 - June 24, 1993, Publ by ASME, pp. 189-199.
[46] Rotta, J., 1968, "Über eine methode zur Berechnung turbulenter Scherströmungen," Aerodynamische Versuchanstalt Göttingen, Rep, 69, p. A14.
[47] Launder, B. E., Reece, G. J., and Rodi, W., 1975, "Progress in the development of a reynolds-stress turbulence closure," Journal of Fluid Mechanics, 68(pt 3), pp. 537-566.
[48] Ansys, I., 2015, "ANSYS FLUENT Theory Guide," ANSYS, Inc., Canonsburg, PA.
[49] Launder, B. E., 1989, "Second-moment closure and its use in modelling turbulent industrial flows," International Journal for Numerical Methods in Fluids, 9(8), pp. 963-985.
[50] Davidson, P. A., 2004, Turbulence: an introduction for scientists and engineers, Oxford University Press.

[51] Girimaji, S., "Partially-averaged navier stokes model for turbulence: Implementation and validation
43rd AIAA Aerospace Sciences Meeting and Exhibit - Meeting Papers," pp. 12887-12900.
[52] Ranjan, P., and Dewan, A., 2010, "Partially Averaged Navier Stokes simulation of turbulent heat transfer from a square cylinder," International Journal of Heat and Mass Transfer, 89, pp. 251-266.
[53] Jeong, E., 2010, "Partially averaged Navier–Stokes (PANS) method for turbulence simulations—Flow past a square cylinder," Journal of fluids engineering, 132(12), p. 121203.
[54] Davidson, L., 2014, "The PANS k- model in a zonal hybrid RANS-LES formulation," International Journal of Heat and Fluid Flow, 46, pp. 112-126.
[55] Minelli, G., Krajnović, S., and Basara, B., 2017, "LES and PANS of Turbulent Flow Through a Staggered Tube Bundle," (58059), p. V01BT12A009.
[56] Foroutan, H., and Yavuzkurt, S., 2014, "A partially-averaged Navier-Stokes model for the simulation of turbulent swirling flow with vortex breakdown," International Journal of Heat and Fluid Flow, 50, pp. 402-416.
[57] Sagaut, P., Deck, S., and Terracol, M., 2013, Multiscale and multiresolution approaches in turbulence: LES, DES and hybrid RANS/LES methods: applications and guidelines, World Scientific.
[58] Gritskevich, M. S., Garbaruk, A. V., Schutze, J., and Menter, F. R., 2012, "Development of DDES and IDDES formulations for the k- shear stress transport model," Flow, Turbulence and Combustion, 88(3), pp. 431-449.
[59] Nichols, R. H., 2010, "Turbulence models and their application to complex flows," University of Alabama at Birmingham, Revision, 4, p. 89.
[60] Nicoud, F., and Ducros, F., 1999, "Subgrid-scale stress modelling based on the square of the velocity gradient tensor," Flow, Turbulence and Combustion, 62(3), pp. 183-200.
[61] Martin, H., 2002, "The generalized Lévêque equation and its practical use for the prediction of heat and mass transfer rates from pressure drop," Chemical Engineering Science, 57(16), pp. 3217-3223.
[62] Scholten, J. W., and Murray, D. B., 1998, "Heat transfer and velocity fluctuations in a staggered tube array," International Journal of Heat and Fluid Flow, 19(3), pp. 233-244.
[63] Dittus, W., and Boelter, L. M. K., 1930, "Heat transfer in automobile radiators of the tubular type," University of California -- Publications in Engineering, 2(13), pp. 443-461.
[64] Gaddis, E. S., and Gnielinski, V., 1985, "Pressure drop in cross flow across tube bundles," Journal Name: Int. Chem. Eng.; (United States); Journal Volume: 25:1, pp. Medium: X; Size: Pages: 1-15.
[65] Meyer, K. E., "Local heat transfer from a tube in a staggered tube bundle," Proc. Proceedings of the Second Baltic Heat Transfer Conference, August 21, 1995 - August 23, 1995, Computational Mechanics Publ, pp. 289-298.
[66] Kelemenis, C. I., and Turner, J. T., "Simultaneous measurement of velocity and temperature fluctuations in a cross-flow tube bundle," Proc. Fifth International

Conference on Laser Anemometry, August 23, 1993 - August 27, 1993, Publ by Society of Photo-Optical Instrumentation Engineers, pp. 649-656.
[67] Buyruk, E., 1999, "Heat transfer and flow structures around circular cylinders in cross-flow," Turkish journal of engineering & environmental sciences, 23(5), pp. 299-315.
[68] Meyer, K. E., 1994, "Experimental and Numerical Investigation of Turbulent Flow and Transfer in Staggered Tube Bundles," Technical University of Denmark (DTU), Kgs. Lyngby, Denmark.
[69] Simonin, O., and Barcouda, M., "Measurements and prediction of turbulent flow entering a staggered tube bundle," Proc. 4th International Symposium on Applications of Laser Anemometry to Fluid Mechanics, Lisbon, Portugal, paper.
[70] European Research Community on Flow, T. a. C., 1995, "ERCOFTAC Classic Collection Database," http://cfd.mace.manchester.ac.uk/cgi-bin/cfddb/ezdb.cgi?ercdb+search+retrieve+&&&*%%%%dm=Line.
[71] Ridluan, A., and Tokuhiro, A., "SRANS and URANS CFD simulations of turbulent VHTR lower plenum flow," Proc. ASME International Mechanical Engineering Congress and Exposition, IMECE 2007, November 11, 2007 - November 15, 2007, American Society of Mechanical Engineers, pp. 375-382.
[72] Ridluan, A., and Tokuhiro, A., 2008, "Benchmark simulation of turbulent flow through a staggered tube bundle to support CFD as a reactor design tool. Part I: SRANS CFD simulation," Journal of Nuclear Science and Technology, 45(12), pp. 1293-1304.
[73] Ridluan, A., and Tokuhiro, A., 2008, "Benchmark simulation of turbulent flow through a staggered tube bundle to support CFD as a reactor design tool. Part II: URANS CFD simulation," Journal of Nuclear Science and Technology, 45(12), pp. 1305-1315.
[74] Moulinec, C., Pourquié†, M. J. B. M., Boersma‡, B. J., Buchal¶, T., and Nieuwstadt‖, F. T. M., 2004, "Direct Numerical Simulation on a Cartesian Mesh of the Flow through a Tube Bundle," International Journal of Computational Fluid Dynamics, 18(1), pp. 1-14.
[75] Benhamadouche, S., and Laurence, D., 2003, "LES, coarse LES, and transient RANS comparisons on the flow across a tube bundle," International Journal of Heat and Fluid Flow, 24(4), pp. 470-479.
[76] Rollet-Miet, P., Laurence, D., and Ferziger, J., 1999, "LES and RANS of turbulent flow in tube bundles," International Journal of Heat and Fluid Flow, 20(3), pp. 241-254.
[77] Ramezanpour, A., Mirzaee, I., Rahmani, R., and Shirvani, H., 2006, "Numerical study of staggered tube bundle in turbulent cross flow for an optimum arrangement," International Journal of Heat Exchangers, 7(1), pp. 37-56.
[78] Ramezanpour, A., Rahmani, R., Shirvani, H., and Mirzaee, I., "Three dimensional numerical modelling of staggered tube bundle turbulent crossflow in duct," Proc. 2005 ASME Summer Heat Transfer Conference, HT 2005, July 17, 2005 - July 22, 2005, American Society of Mechanical Engineers, pp. 609-617.
[79] Giedt, W. H., 1949, "Investigation of variation of point unit heat-transfer coefficient around cylinder normal to air stream," American Society of Mechanical Engineers -- Transactions, 71(4), pp. 375-381.

[80] Lyn, D. A., Einav, S., Rodi, W., and Park, J. H., 1995, "Laser-Doppler velocimetry study of ensemble-averaged characteristics of the turbulent near wake of a square cylinder," Journal of Fluid Mechanics, 304, pp. 285-319.
[81] Igarashi, T., 1985, "Heat transfer form a square prism to an air stream," International Journal of Heat and Mass Transfer, 28(1), pp. 175-181.
[82] Song, C.-S., and Park, S.-O., 2009, "Numerical simulation of flow past a square cylinder using Partially-Averaged Navier-Stokes model," Journal of Wind Engineering and Industrial Aerodynamics, 97(1), pp. 37-47.
[83] aus der Wiesche, S., 2007, "Large-eddy simulation study of an air flow past a heated square cylinder," Heat and Mass Transfer, 43(6), pp. 515-525.
[84] Chatterjee, D., Biswas, G., and Amiroudine, S., 2010, "Numerical simulation of flow past row of square cylinders for various separation ratios," Computers & Fluids, 39(1), pp. 49-59.
[85] Igarashi, T., 1986, "Local heat transfer from a square prism to an airstream," International Journal of Heat and Mass Transfer, 29(5), pp. 777-784.
[86] Igarashi, T., and Mayumi, Y., 2001, "Fluid flow and heat transfer around a rectangular cylinder with small inclined angle (the case of a width/height ratio of a section of 5)," International Journal of Heat and Fluid Flow, 22(3), pp. 279-286.
[87] Ansys, I., 2015, "ANSYS FLUENT UDF Manual," ANSYS, Inc., Canonsburg, PA.
[88] Hussain, A. F., 1983, "Coherent structures—reality and myth," The Physics of fluids, 26(10), pp. 2816-2850.
[89] Menter, F. R., 2012, "Best Practices: Scale-Resolving Simulations in ANSYS CFD."
[90] Menter, F., Kuntz, M., and Bender, R., "A scale-adaptive simulation model for turbulent flow predictions," Proc. 41st aerospace sciences meeting and exhibit, p. 767.
[91] Menter, F. R., Egorov, Y., and Rusch, D., "Steady and unsteady flow modelling using the k−√ kL model," Proc. Ichmt Digital Library Online, Begel House Inc.
[92] Rotta, J., 1972, "Turbulent flows (Turbulente Stromungen)," Stuttgart: Teubner-Verlag.
[93] Menter, F. R., and Egorov, Y., "A scale-adaptive simulation model using two-equation models," Proc. 43rd AIAA Aerospace Sciences Meeting and Exhibit, January 10, 2005 - January 13, 2005, American Institute of Aeronautics and Astronautics Inc., pp. 271-283.
[94] Egorov, Y., and Menter, F., "Development and Application of SST-SAS Turbulence Model in the DESIDER Project," Springer Berlin Heidelberg, pp. 261-270.
[95] Weilin, Z., 2016, "Comparative assessment of SAS and DES turbulence modeling for massively separated flows," Acta mechanica Sinica = 力学学报(英文版), 32(1).
[96] Wang, X., and Li, D., 2014, "Behavior of SST-SAS for mild airfoil trailing-edge separation," Xibei Gongye Daxue Xuebao/Journal of Northwestern Polytechnical University, 32(3), pp. 337-340.
[97] Ravelli, S., and Barigozzi, G., 2014, "Application of unsteady computational fluid dynamics methods to trailing edge cutback film cooling," Journal of Turbomachinery, 136(12).

[98] Aminian, J., 2018, "Scale adaptive simulation of vortex structures past a square cylinder," Journal of Hydrodynamics, 30(4), pp. 657-671.
[99] Patankar, S., 1980, Numerical heat transfer and fluid flow, CRC press.

A. IMPLEMENTATION OF TURBULENCE MODELS IN FLUENT

Custom turbulence models can be implemented in to the commercial CFD software Fluent through the use of User Define Functions (UDFs) [87]. The parameters of the turbulence model (k and ω for example) are scalars that behave in a fluid as any chemical species would.

For a generic scalar, ϕ, the transport equation can be written as:

$$\frac{\partial(\rho\phi)}{\partial t} + \frac{\partial(\rho u_j \phi)}{\partial x_j} = S_\phi + \frac{\partial}{\partial x_j}\left(D_\phi \frac{\partial \phi}{\partial x_j}\right) \tag{78}$$

Fluent will handle the transient, convection and diffusion terms automatically. The user supplies the source term, S_ϕ and the diffusion coefficient, D_ϕ which are supplied to the code through subroutines in the C programming language. The first derivative of the source term relative to the scalar $\left(\frac{S_\phi}{\partial\phi}\right)$ is provided as well. If the source term is non-linear relative to ϕ, as is common for equations for k and ω, special care must be taken to prevent divergence of the solution [99], [30].

The number of scalars used for the model is selected from the interface and the user must keep track of the scalar number when performing calculations. For all the models created in the resent study, Scalar 0 was the turbulent kinetic energy, k and Scalar 1 was the specific dissipation, ω.

For the source term, a function is written under the function call:

DEFINE_SOURCE(Source_Identifier, c, t, dS, eqn)

The "Source_Identifier" is the label given to a source UDF and it will appear in the Fluent interface under that name when the code is compiled. The variable "c" is all the cells of the domain and "t" is a data structure type that allows access to all the cells in a domain. "dS" is the first derivative of the source term relative to the scalar parameter. Finally, the value for the source term itself is returned by the function. No looping is required to calculate the values as the function is called for each cell in the domain. In the user interface, the source term for each scalar is selected under the Cell Zone Conditions option. The scalar values for the are addressed as C_UDSI(c, t, TKE) where TKE was defined as 0 and C_UDSI(c, t, OMG) where OMG is defined a 1. Other parameters are available including the fluid density, C_R(c, t) or the local turbulent viscosity, C_MU_T(c, t).

The diffusion coefficient D_ϕ is defined with

DEFINE_DIFFUSIVITY(ScalarEquation, c, t, ScalarNumber)

and is selected under the materials definition in the interface.

Initial conditions as well as flow inlet conditions can be set directly for k and ω. The wall boundary condition is set directly to zero for k (Equation (23) while an equation for

the ω (Equation (22) is selected in the Graphical User Interface (GUI) with the function DEFINE_PROFILE. This equation is also provided in the source code.

Limits are required on k and ω to prevent errant values from causing divergence. The limits for these values are $10^{-8} < k < 100$ and $100 < \omega < 10^{8}$. The limits are applied at the end of every iteration with DEFINE_ADJUST which can be selected in the GUI. It was found however that divergence still occurred from time to time so these limits were also included into every function, i.e. source and diffusion coefficients functions. The resulting the solution became very stable.

Source code for Fluent UDFs

```
Source Code for Fluent UDF

#include "udf.h"
#include "mem.h"
/* #include "math.h" */
#include "sg_udms.h"
#include "global.h"
#include "sg.h"

/* User-defined constants */
#define ALPHA  0.55555555555555555
#define ALPHA_INF 0.52
#define A_1 0.31
#define ALPHA_STAR 1.0
#define BETA  0.075
#define BETA_I 0.0708
#define SIGMA  0.5
#define BETA_STAR_INF 0.09
#define BETA_STAR 0.09
#define R_BETA 8.0
#define SIGMAStart  0.5
#define SIGMA_D0  0.125
#define VONKARMON_K 0.41
#define VONKARMON_K_SQ  0.1681
#define BETA_I1  0.075
#define BETA_I2  0.0828
#define C_MU 0.09
#define SIGMA_K1  1.176
#define SIGMA_OMEGA1  2.0
```

```
#define SIGMA_K2  1.0
#define CLIM 10
#define SIGMA_OMEGA2 1.168
#define ETA_2 3.51
#define SIGMA_PHI 0.666666667
#define C_SAS 2.0
#define C_S_SAS 0.11
#define MIN_TKE 1E-8
#define MAX_TKE   100
#define MIN_OMG 1E+2
#define MAX_OMG 1E+8
/*#define F_OMEGA 1.0 */
#define WDD_UDM 10
/*#define MIN(a,b) (((a)<(b))?(a):(b)) */

/* User-defined scalars */
enum

  {
   TKE,
   OMG,
   N_REQUIRED_UDS
 };

void cpySVartoUDM(Domain *domain, Svar sv, int udm)
{
  size_t realsize = sizeof(real);
  real  *svpointr = NULL;
  real  *udmpoint = NULL;
  Thread  *thread = NULL;
  Domain  *supdom = DOMAIN_SUPER_DOMAIN(domain);
  if (NULLP(supdom))
    {
      supdom = domain;
    }

  if (n_udm <= udm)
    {
      Error("cpySVartoUDM(): too few User Defined Memory Locations.\n"
            "Location %d was requested, but there are only %d
allocated.\n",
                        udm,                                  n_udm);
    }

  thread_loop_c(thread, domain)
    {
      Thread *supthr = THREAD_SUPER_THREAD(thread);
      if (NULLP(supthr))
        {
          supthr = thread;
        }

      if (NNULLP(svpointr = THREAD_STORAGE(thread, sv)) &&
```

```
          (NNULLP(THREAD_STORAGE(supthr, SV_UDM_I)) ?
           NNULLP(udmpoint = T_STORAGE_R_XV(supthr, SV_UDM_I, udm)) :
FALSE))
        {
          int numbytes = realsize * thread->nelements;
          memcpy(udmpoint, svpointr, numbytes);
        }
    }
}

DEFINE_INIT(wall_dist,domain)  /* use this for new cases */
{
#if !RP_HOST
/* works in serial or node processes */
/* solution data is not on host process anyway */
      Alloc_Storage_Vars(domain,SV_RTMP_0,SV_NULL);
      Calc_Cell_Wall_Distance_New(domain,SV_RTMP_0);
      cpySVartoUDM(domain,SV_RTMP_0,WDD_UDM);
      Free_Storage_Vars(domain,SV_RTMP_0, SV_NULL);
      cpySVartoUDM(domain,1,3);
#endif
}

DEFINE_ON_DEMAND(StoreCellWallDistance)
{
#if !RP_HOST
      Domain *d = Get_Domain(1);
      Alloc_Storage_Vars(d,SV_RTMP_0,SV_NULL);
      Calc_Cell_Wall_Distance_New(d,SV_RTMP_0);
      cpySVartoUDM(d,SV_RTMP_0,WDD_UDM);
      Free_Storage_Vars(d,SV_RTMP_0,SV_NULL);
#endif
}
/* *************************Diffusivity term of TKE and
OMG*******************************/
DEFINE_DIFFUSIVITY(kw_diff,c,t,eqn)
{
 double diff; /* define the diffusion coeffcient  */
 double D_w_plus, Phi_1_part1, Phi_1_part2, Phi_1, F1, Sigma_k,
Sigma_omega, walldist;
 double Phi_1_4, f_k, f_omega;

 /*  BSL k-w diffusion equations   */

C_UDSI(c, t, TKE) = MAX(C_UDSI(c, t, TKE), MIN_TKE);
C_UDSI(c, t, TKE) = MIN(C_UDSI(c, t, TKE), MAX_TKE);
C_UDSI(c, t, OMG) = MAX(C_UDSI(c, t, OMG), MIN_OMG);
C_UDSI(c, t, OMG) = MIN(C_UDSI(c, t, OMG), MAX_OMG);

f_k =  C_UDMI(c, t, 3);
/* f_omega = 1.0/f_k; */

f_omega = 1.0;
```

```
 walldist = C_UDMI(c, t, WDD_UDM);

 if (NULL == T_STORAGE_R_NV(t,SV_UDSI_G(TKE)) ||
     NULL == T_STORAGE_R_NV(t,SV_UDSI_G(OMG)))
    {
  *&  /* Message("Can't calculate diffusivity just yet...\n"); */
    diff = C_MU_T(c, t);
      return diff;
      }

      D_w_plus = MAX(2.0*C_R(c, t)/(SIGMA_OMEGA2*C_UDSI(c, t,
OMG))*NV_DOT(C_UDSI_G(c, t, TKE), C_UDSI_G(c, t, OMG)), 1.0E-10);

      Phi_1_part1 = MAX(pow(C_UDSI(c, t, TKE), 0.5)/(0.09*C_UDSI(c, t,
OMG)*walldist), 500.0*C_MU_L(c, t)/(C_R(c,
t)*walldist*walldist*C_UDSI(c, t, OMG)));

      Phi_1_part2 = 4.0*C_R(c, t)*C_UDSI(c, t,
TKE)/(SIGMA_OMEGA2*D_w_plus*walldist*walldist);

      Phi_1 = MIN(Phi_1_part1, Phi_1_part2);

      Phi_1_4 = pow(Phi_1, 4.0);

      F1 = tanh(Phi_1_4);

      C_UDMI(c, t, 1) = F1;

      Sigma_k = 1.0/(F1/SIGMA_K1 + (1.0 - F1)/SIGMA_K2);

      Sigma_omega = 1.0/(F1/SIGMA_OMEGA1 + (1.0 - F1)/SIGMA_OMEGA2);

     switch (eqn)
             {
              case TKE:
                       diff=C_MU_L(c,t) +
(f_omega/f_k)*(C_MU_T(c,t)/Sigma_k);  /* EQN 4.66 Fluent Theory Guide
*/
                       break;
              case OMG:
                       diff=C_MU_L(c,t) +
(f_omega/f_k)*(C_MU_T(c,t)/Sigma_omega);  /* EQN 4.66 Fluent Theory
Guide */
                       break;
              default:
                       diff=C_MU_T(c,t)+C_MU_L(c,t);
             }
         return diff;
 }

 /* *************************Effecitve Diffusitity TKE and
OMG*******************************/
```

```
DEFINE_TURBULENT_VISCOSITY(user_mu_t,c,t)
 {
       double mu_t, Phi_2, F2, walldist;
       double Term1, Term2;

       walldist = C_UDMI(c, t, WDD_UDM);

      C_UDSI(c, t, TKE) = MAX(C_UDSI(c, t, TKE), MIN_TKE);
      C_UDSI(c, t, TKE) = MIN(C_UDSI(c, t, TKE), MAX_TKE);
      C_UDSI(c, t, OMG) = MAX(C_UDSI(c, t, OMG), MIN_OMG);
      C_UDSI(c, t, OMG) = MIN(C_UDSI(c, t, OMG), MAX_OMG);

       Term1 = 2.0*pow(C_UDSI(c, t, TKE), 0.5)/(0.09*C_UDSI(c, t,
OMG)*walldist);
       Term2 = 500.0*C_MU_L(c, t)/(C_R(c,
t)*walldist*walldist*C_UDSI(c, t, OMG));


       Phi_2 = MAX(Term1, Term2);

       F2 = tanh(Phi_2*Phi_2);

       C_UDMI(c, t, 2) = F2;

/*     DUDY = C_DUDX(c, t);
       DVDX = C_DVDX(c, t);
       DUDX = C_DUDX(c, t);
       DVDY = C_DVDY(c, t);

       Vorticity[0][0] =  0.0;
       Vorticity[0][1] =  0.5*(DUDY - DVDX);
       Vorticity[1][0] =  0.5*(DVDX - DUDY);
     Vorticity[1][1] =  0.0;

       VorticityMag = pow(2*(Vorticity[0][1]*Vorticity[0][1] +
Vorticity[1][0]*Vorticity[1][0]), 0.5);  */

/*     mu_t = C_R(c, t)*C_K(c, t)/C_O(c, t)*(1.0/MAX(1.0/ALPHA_STAR,
Strainrate_Mag(c, t)*F2/(A_1*C_O(c, t))));  */



/*    C_UDMI(c, t, 4) =  Strainrate_Mag(c, t)*F2/(A_1*C_UDSI(c, t,
OMG));
      C_UDMI(c, t, 5) =  VorticityMag*F2/(A_1*C_UDSI(c, t, OMG));  */

       mu_t = C_R(c, t)*C_UDSI(c, t, TKE)/C_UDSI(c, t,
OMG)*(1.0/MAX(1.0/ALPHA_STAR, Strainrate_Mag(c, t)*F2/(A_1*C_UDSI(c, t,
OMG))));

      return mu_t;

 }
```

```
/* ********************************Source term of
TKE***********************************/

DEFINE_SOURCE(k_source,c,t,dS,eqn)
{
double P_k, Y_k, Beta_Star, Beta_Star_i, dPk_dk, dYk_dk;
double P_k_Tilda, StrainMag, StrainMagSquared, F_2;
double S_p;

      C_UDSI(c, t, TKE) = MAX(C_UDSI(c, t, TKE), MIN_TKE);
      C_UDSI(c, t, TKE) = MIN(C_UDSI(c, t, TKE), MAX_TKE);
      C_UDSI(c, t, OMG) = MAX(C_UDSI(c, t, OMG), MIN_OMG);
      C_UDSI(c, t, OMG) = MIN(C_UDSI(c, t, OMG), MAX_OMG);

      StrainMag = Strainrate_Mag(c,t);

      StrainMagSquared = SQR(Strainrate_Mag(c,t));

      F_2 = C_UDMI(c, t, 2);

/*    Re_t = C_R(c, t)*C_UDSI(c, t, TKE)/(C_MU_L(c, t)*C_UDSI(c, t,
OMG)); */

      P_k = C_MU_T(c,t)*StrainMagSquared;

      Beta_Star_i = BETA_STAR_INF;  /* No correction for low turbulence
EQN 4.81 Fluent Theory Guide */

      Beta_Star = Beta_Star_i;      /* No correction for compressible
flow EQN 4.81 Fluent Theory Guide */

/*    Beta_I_star = BETA_STAR_INF*(4.0/15.0 + pow(Re_t/R_BETA,
4.0))/(1.0 + pow(Re_t/R_BETA, 4.0));  */

    Y_k = C_R(c, t)*Beta_Star*C_UDSI(c, t, OMG)*C_UDSI(c, t, TKE);  /*
EQN 4.77 Fluent Theory Guide */
    Y_k = C_R(c, t)*Beta_Star*C_O(c, t)*C_UDSI(c, t, TKE);  /* EQN 4.77
Fluent Theory Guide */

      P_k_Tilda = MIN(P_k, 10*Y_k);  /*  Production limit for
stagnation regions
                                                    from Menter,
Kuntz, and Langtry "Ten Years of Industrial Experience with the SST
Turbulence Model */

      dPk_dk = 0.0;  /*  Linearized Derivative for P_k Portion */

      dYk_dk =  Y_k/C_UDSI(c, t, TKE); /* Linearized Derivative for S_k
Portion */

    S_p = -dYk_dk;

/*    if(k_lim/C_UDSI(c, t, TKE) > 10.0) dS[eqn] = 20.0*dS[eqn];  */
```

```
/*    C_UDMI(c, t, 4) = k_lim;
      C_UDMI(c, t, 5) = dPk_dk - dYk_dk;  */

      dS[eqn] = S_p;

return P_k_Tilda - Y_k;
}

/* ********************************Source term of TKE - Production
Limiter and Kato Launder ***********************************/
DEFINE_SOURCE(KL_k_source,c,t,dS,eqn)
{
double P_k, Y_k, Re_t, Beta_Star, Beta_Star_i, dPk_dk, dYk_dk;
double P_k_Tilda, StrainMag, F_2;
double Vort21, Vort12, Vort31, Vort13, Vort32, Vort23, VortMag;
double S_p;

      C_UDSI(c, t, TKE) = MAX(C_UDSI(c, t, TKE), MIN_TKE);
      C_UDSI(c, t, TKE) = MIN(C_UDSI(c, t, TKE), MAX_TKE);
      C_UDSI(c, t, OMG) = MAX(C_UDSI(c, t, OMG), MIN_OMG);
      C_UDSI(c, t, OMG) = MIN(C_UDSI(c, t, OMG), MAX_OMG);

      StrainMag = Strainrate_Mag(c,t);

      Vort21 = 0.5*(C_DVDX(c, t) - C_DUDY(c, t));
      Vort12 = -Vort21;

      Vort31 = 0.5*(C_DWDX(c, t) - C_DUDZ(c, t));
      Vort13 = -Vort31;

      Vort32 = 0.5*(C_DWDY(c, t) - C_DVDZ(c, t));
      Vort23 = -Vort32;

      VortMag = pow(2*(Vort21*Vort21 + Vort12*Vort12 + Vort31*Vort31 +
Vort13*Vort13 + Vort23*Vort23 + Vort32*Vort32), 0.5);

      /* C_UDMI(c, t, 7) = VortMag;  */

      F_2 = C_UDMI(c, t, 2);

      Re_t = C_R(c, t)*C_UDSI(c, t, TKE)/(C_MU_L(c, t)*C_UDSI(c, t,
OMG));

      P_k = C_MU_T(c,t)*StrainMag*VortMag;

      Beta_Star_i = BETA_STAR_INF;  /* No correction for low turbulence
EQN 4.81 Fluent Theory Guide */

      Beta_Star = Beta_Star_i;      /* No correction for compressible
flow EQN 4.81 Fluent Theory Guide */
```

```
       Y_k = C_R(c, t)*Beta_Star*C_UDSI(c, t, OMG)*C_UDSI(c, t, TKE);
/* EQN 4.77 Fluent Theory Guide */

      P_k_Tilda = MIN(P_k, CLIM*Y_k);  /*  Production limit for
stagnation regions
                                                    from Menter,
Kuntz, and Langtry "Ten Years of Industrial Experience with the SST
Turbulence Model */

      dPk_dk = 0.0;  /*  Linearized Derivative for P_k Portion */

      dYk_dk =  MAX(0, Y_k/C_UDSI(c, t, TKE));  /* Linearized
Derivative for S_k Portion, prevents negative source derivative */

       S_p = -dYk_dk;

         S_p = MIN(S_p, 0);

      dS[eqn] = S_p;

return P_k_Tilda - Y_k;
}


/*********************************Source term of
OMG*********************************/
DEFINE_SOURCE(OMG_source, c, t, dS, eqn)
 {
 double P_k, alpha, P_w, Y_w, Y_k, beta;
  double Beta_i, D_w, alpha_inf, F1;
  double alpha_inf1, alpha_inf2, alpha_star;
  double P_k_Tilda;
  double omega_lim;
  double Beta_Star, Beta_Star_i;
  double S_p, S_star, S_c, Source, relaxation, f_k, f_omega;

  C_UDSI(c, t, TKE) = MAX(C_UDSI(c, t, TKE), MIN_TKE);
  C_UDSI(c, t, TKE) = MIN(C_UDSI(c, t, TKE), MAX_TKE);
  C_UDSI(c, t, OMG) = MAX(C_UDSI(c, t, OMG), MIN_OMG);
  C_UDSI(c, t, OMG) = MIN(C_UDSI(c, t, OMG), MAX_OMG);

  f_k = C_UDMI(c, t, 3);
  /* f_omega = 1.0/f_k; */
  f_omega = 1.0;

  Beta_Star_i = BETA_STAR_INF;  /*  No correction for low turbulence
EQN 4.81 Fluent Theory Guide */

  Beta_Star = Beta_Star_i;    /* No correction for compressible flow
EQN 4.81 Fluent Theory Guide */

  P_k = C_MU_T(c,t)*SQR(Strainrate_Mag(c,t)); /* EQN 4.74 Fluent Theory
Guide */
```

```
  Y_k = C_R(c, t)*Beta_Star*C_UDSI(c, t, OMG)*C_UDSI(c, t, TKE);  /*
EQN 4.77 Fluent Theory Guide */

  P_k_Tilda = MIN(P_k, 10*Y_k);


  F1 = C_UDMI(c, t, 1);

/*  alpha_inf1 = BETA_I1/BETA_STAR_INF -
VONKARMON_K_SQ/(SIGMA_OMEGA1*pow(BETA_STAR_INF, 0.5));
  alpha_inf2 = BETA_I2/BETA_STAR_INF -
VONKARMON_K_SQ/(SIGMA_OMEGA2*pow(BETA_STAR_INF, 0.5));  */

  alpha_inf1 = 5.0/9.0;
  alpha_inf2 = 0.44;

  alpha_inf = F1*alpha_inf1 + (1.0-F1)*alpha_inf2;
  alpha_star = 1.0;   /* High Reynolds Number */

  alpha = alpha_inf;

  P_w = alpha*C_R(c, t)*P_k_Tilda/C_MU_T(c, t);     /* EQN 4.75 Fluent
Theory Guide */

  Beta_i = F1*BETA_I1 + (1.0-F1)*BETA_I2;

  beta = Beta_i;  /* No correction for compressible flow EQN 4.89
Fluent Theory Guide */

  if (NULL == T_STORAGE_R_NV(t,SV_UDSI_G(TKE)) || NULL ==
T_STORAGE_R_NV(t,SV_UDSI_G(OMG)))
        {/* Message("Can't calculate D_w just yet...\n"); */
        C_UDMI(c, t,  9) = 0.0;
      D_w = 0.0;
          }
     else
            D_w = (1.0-F1)*(f_omega/f_k)*MAX(2.0*C_R(c,
t)/(SIGMA_OMEGA2*C_UDSI(c, t, OMG))*NV_DOT(C_UDSI_G(c, t, TKE),
C_UDSI_G(c, t, OMG)), 1e-10);

/*  Y_w = (1.0/F_OMEGA - 1.0)*Beta_Star*alpha*C_R(c, t)/C_MU_T(c, t) -
                          C_R(c,
t)*beta*C_UDSI(c,t,OMG)*C_UDSI(c,t,OMG)/f_omega;   */


  Y_w =  (1.0/f_omega - 1.0)*Beta_Star*alpha*C_UDSI(c,t,OMG)*C_R(c,
t)/C_MU_T(c, t) +
             C_R(c, t)*beta*C_UDSI(c,t,OMG)*C_UDSI(c,t,OMG)/f_omega;

  Source = P_w - Y_w + D_w;
```

```
  S_p = -(D_w + 2.0*Y_w)/C_UDSI(c, t, OMG);

  S_c = P_w - 3.0*Y_w + 2.0*D_w;

  omega_lim = -S_c/S_p;

  S_star = P_w - Y_w + D_w;

  dS[eqn] = -S_star/(omega_lim - C_UDSI(c, t, OMG));


/*  dS[eqn] = -(D_w + 2.0*Y_w)/C_UDSI(c, t, OMG);  */

 relaxation = 1.0;

 C_UDMI(c, t, 8) = S_p;
/* C_UDMI(c, t, 9) = Source;  */

 dS[eqn] = S_p;

 return Source;
 }
 /**********************************Source term of OMG for Kato Launder
and Production Limited ***********************************/
 DEFINE_SOURCE(KL_OMG_source, c, t, dS, eqn)
  {
  double P_k, alpha, P_w, Y_w, Y_k, beta;
   double alpha_inf, F1, Beta_i, D_w;
   double alpha_inf1, alpha_inf2, alpha_star;
   double P_k_Tilda;
   double Beta_Star, Beta_Star_i;
   double S_p, Source, f_k, f_omega;
   double Vort21, Vort12, Vort31, Vort13, Vort32, Vort23, VortMag,
StrainMag;

      C_UDSI(c, t, TKE) = MAX(C_UDSI(c, t, TKE), MIN_TKE);
      C_UDSI(c, t, TKE) = MIN(C_UDSI(c, t, TKE), MAX_TKE);
      C_UDSI(c, t, OMG) = MAX(C_UDSI(c, t, OMG), MIN_OMG);
      C_UDSI(c, t, OMG) = MIN(C_UDSI(c, t, OMG), MAX_OMG);

      StrainMag = Strainrate_Mag(c,t);

      Vort21 = 0.5*(C_DVDX(c, t) - C_DUDY(c, t));
      Vort12 = -Vort21;

      Vort31 = 0.5*(C_DWDX(c, t) - C_DUDZ(c, t));
      Vort13 = -Vort31;

      Vort32 = 0.5*(C_DWDY(c, t) - C_DVDZ(c, t));
      Vort23 = -Vort32;
```

```
      VortMag = pow(2*(Vort21*Vort21 + Vort12*Vort12 + Vort31*Vort31 +
Vort13*Vort13 + Vort23*Vort23 + Vort32*Vort32), 0.5);

      P_k = C_MU_T(c,t)*StrainMag*VortMag;

      /* P_k = C_MU_T(c,t)*SQR(Strainrate_Mag(c,t));  EQN 4.74 Fluent
Theory Guide */

   f_k = C_UDMI(c, t, 3);
   /*  f_omega = 1.0/f_k; */
   f_omega = 1.0;

   Beta_Star_i = BETA_STAR_INF;  /*  No correction for low turbulence
EQN 4.81 Fluent Theory Guide */

   Beta_Star = Beta_Star_i;   /* No correction for compressible flow
EQN 4.81 Fluent Theory Guide */



   Y_k = C_R(c, t)*BETA_STAR_INF*C_UDSI(c, t, OMG)*C_UDSI(c, t, TKE);
/* EQN 4.77 Fluent Theory Guide */

   P_k_Tilda = MIN(P_k, CLIM*Y_k);


   F1 = C_UDMI(c, t, 1);

 /*  alpha_inf1 = BETA_I1/BETA_STAR_INF -
VONKARMON_K_SQ/(SIGMA_OMEGA1*pow(BETA_STAR_INF, 0.5));
   alpha_inf2 = BETA_I2/BETA_STAR_INF -
VONKARMON_K_SQ/(SIGMA_OMEGA2*pow(BETA_STAR_INF, 0.5));  */

   alpha_inf1 = 5.0/9.0;
   alpha_inf2 = 0.44;

   alpha_inf = F1*alpha_inf1 + (1.0-F1)*alpha_inf2;
   alpha_star = 1.0;   /* High Reynolds Number */

   alpha = alpha_inf;

   P_w = alpha*C_R(c, t)*P_k_Tilda/C_MU_T(c, t);          /* EQN 4.75
Fluent Theory Guide */

   Beta_i = F1*BETA_I1 + (1.0-F1)*BETA_I2;

   beta = Beta_i;  /* No correction for compressible flow EQN 4.89
Fluent Theory Guide */

   Y_w =  (1.0/f_omega -
1.0)*Beta_Star*alpha*C_UDSI(c,t,OMG)*C_UDSI(c,t,TKE)*C_R(c,
t)/C_MU_T(c, t) +
            C_R(c, t)*beta*C_UDSI(c,t,OMG)*C_UDSI(c,t,OMG)/f_omega;
```

```
   if (NULL == T_STORAGE_R_NV(t,SV_UDSI_G(TKE)) || NULL ==
T_STORAGE_R_NV(t,SV_UDSI_G(OMG)))
         {/* Message("Can't calculate D_w just yet...\n"); */
         C_UDMI(c, t,  9) = 0.0;
            D_w = 0.0;
          }
      else
            D_w = (1.0-F1)*MAX((f_omega/f_k)*2.0*SIGMA_OMEGA2*C_R(c,
t)/(C_UDSI(c, t, OMG))*NV_DOT(C_UDSI_G(c, t, TKE), C_UDSI_G(c, t,
OMG)), 1e-10);

   Source = P_w - Y_w + D_w;

    S_p = MIN(0, -(D_w + 2.0*Y_w)/C_UDSI(c, t, OMG));

    S_p = MIN(S_p, 0);

/*    C_UDMI(c, t, 5) = Source;

      C_UDMI(c, t, 6) = S_p;  */

    dS[eqn] = S_p;

  return Source;
 }
 /**********************************Source term of OMG for SAS with
Kato Launder and Production Limited
**********************************/
 /**********************************Source term Modified for SAS Model
**********************************/
 DEFINE_SOURCE(SAS_KL_OMG_source, c, t, dS, eqn)
   {
   double P_k, alpha, P_w, Y_w, Y_k, beta;
    double alpha_inf, F1, Beta_i, D_w;
    double alpha_inf1, alpha_inf2, alpha_star;
    double P_k_Tilda, Alt_StrainMagSquared;
    double Beta_Star, Beta_Star_i;
    double S_p, Source, f_k, f_omega, Q_SAS, dQ_SAS_dw;
    double Vort21, Vort12, Vort31, Vort13, Vort32, Vort23, VortMag,
StrainMag;
    double d2udx2, d2udy2, d2udz2, d2vdx2, d2vdy2, d2vdz2, d2wdx2,
d2wdy2, d2wdz2;
      double Udoubleprime, coerce();
      double Q_SAS_Term1, Q_SAS_Term2, VonKarmonLengthScale,
TurbulentLengthScale;
      double CellLength, Mod_VonKarmonLengthScale, Omega_Dot, tke_Dot;
      double max_Ratio, u_terms, v_terms, w_terms;

      max_Ratio = 1000.0;

      C_UDSI(c, t, TKE) = MAX(C_UDSI(c, t, TKE), MIN_TKE);
      C_UDSI(c, t, TKE) = MIN(C_UDSI(c, t, TKE), MAX_TKE);
```

```
      C_UDSI(c, t, OMG) = MAX(C_UDSI(c, t, OMG), MIN_OMG);
      C_UDSI(c, t, OMG) = MIN(C_UDSI(c, t, OMG), MAX_OMG);

      StrainMag = Strainrate_Mag(c,t);

      Vort21 = 0.5*(C_DVDX(c, t) - C_DUDY(c, t));
      Vort12 = -Vort21;

      Vort31 = 0.5*(C_DWDX(c, t) - C_DUDZ(c, t));
      Vort13 = -Vort31;

      Vort32 = 0.5*(C_DWDY(c, t) - C_DVDZ(c, t));
      Vort23 = -Vort32;

      VortMag = pow(2*(Vort21*Vort21 + Vort12*Vort12 + Vort31*Vort31 +
Vort13*Vort13 + Vort23*Vort23 + Vort32*Vort32), 0.5);

      P_k = C_MU_T(c,t)*StrainMag*VortMag;

      /* P_k = C_MU_T(c,t)*SQR(Strainrate_Mag(c,t));  EQN 4.74 Fluent
Theory Guide */

    f_k = C_UDMI(c, t, 3);
    /*  f_omega = 1.0/f_k; */
    f_omega = 1.0;

    Beta_Star_i = BETA_STAR_INF;  /*  No correction for low turbulence
EQN 4.81 Fluent Theory Guide */

    Beta_Star = Beta_Star_i;  /* No correction for compressible flow
EQN 4.81 Fluent Theory Guide */

    Y_k = C_R(c, t)*BETA_STAR_INF*C_UDSI(c, t, OMG)*C_UDSI(c, t, TKE);
/* EQN 4.77 Fluent Theory Guide */

    P_k_Tilda = MIN(P_k, CLIM*Y_k);


    F1 = C_UDMI(c, t, 1);

  /*  alpha_inf1 = BETA_I1/BETA_STAR_INF -
VONKARMON_K_SQ/(SIGMA_OMEGA1*pow(BETA_STAR_INF, 0.5));
    alpha_inf2 = BETA_I2/BETA_STAR_INF -
VONKARMON_K_SQ/(SIGMA_OMEGA2*pow(BETA_STAR_INF, 0.5));  */

    alpha_inf1 = 5.0/9.0;
    alpha_inf2 = 0.44;

    alpha_inf = F1*alpha_inf1 + (1.0-F1)*alpha_inf2;
    alpha_star = 1.0;   /* High Reynolds Number */

    alpha = alpha_inf;
```

```
    P_w = alpha*C_R(c, t)*P_k_Tilda/C_MU_T(c, t);          /* EQN 4.75
Fluent Theory Guide */

    Beta_i = F1*BETA_I1 + (1.0-F1)*BETA_I2;

    beta = Beta_i;  /* No correction for compressible flow EQN 4.89
Fluent Theory Guide */

    Y_w =  (1.0/f_omega -
1.0)*Beta_Star*alpha*C_UDSI(c,t,OMG)*C_UDSI(c,t,TKE)*C_R(c,
t)/C_MU_T(c, t) +
             C_R(c, t)*beta*C_UDSI(c,t,OMG)*C_UDSI(c,t,OMG)/f_omega;

    if (NULL == T_STORAGE_R_NV(t,SV_UDSI_G(TKE)) || NULL ==
T_STORAGE_R_NV(t,SV_UDSI_G(OMG)))
          {/* Message("Can't calculate D_w just yet...\n"); */
          C_UDMI(c, t,  9) = 0.0;
            D_w = 0.0;
          }
       else
            D_w = (1.0-F1)*MAX((f_omega/f_k)*2.0*SIGMA_OMEGA2*C_R(c,
t)/(C_UDSI(c, t, OMG))*NV_DOT(C_UDSI_G(c, t, TKE), C_UDSI_G(c, t,
OMG)), 1e-10);

      d2udx2 = C_UDSI_G(c,t, 3)[0];
      d2udy2 = C_UDSI_G(c,t, 4)[1];
      d2udz2 = C_UDSI_G(c,t, 5)[2];

      d2vdx2 = C_UDSI_G(c,t, 6)[0];
      d2vdy2 = C_UDSI_G(c,t, 7)[1];
      d2vdz2 = C_UDSI_G(c,t, 8)[2];

      d2wdx2 = C_UDSI_G(c,t, 9)[0];
      d2wdy2 = C_UDSI_G(c,t, 10)[1];
      d2wdz2 = C_UDSI_G(c,t, 11)[2];

      u_terms = d2udx2*d2udx2 + d2udy2*d2udy2 + d2udz2*d2udz2 +
2.0*(d2udy2*d2udx2) + 2.0*(d2udx2*d2udz2) + 2.0*(d2udy2*d2udz2);
      v_terms = d2vdx2*d2vdx2 + d2vdy2*d2vdy2 + d2vdz2*d2vdz2 +
2.0*(d2vdy2*d2vdx2) + 2.0*(d2vdx2*d2vdz2) + 2.0*(d2vdy2*d2vdz2);
      w_terms = d2wdx2*d2wdx2 + d2wdy2*d2wdy2 + d2wdz2*d2wdz2 +
2.0*(d2wdy2*d2wdx2) + 2.0*(d2wdx2*d2wdz2) + 2.0*(d2wdy2*d2wdz2);

      Udoubleprime = pow(u_terms + v_terms + w_terms, 0.5);

      StrainMag = Strainrate_Mag(c,t);

      VonKarmonLengthScale = VONKARMON_K*StrainMag/Udoubleprime;
      TurbulentLengthScale = pow(C_UDSI(c,t, 0), 0.5)/(0.5477*C_UDSI(c,
t, 1));

      CellLength = pow(C_VOLUME(c, t), 0.33333333333);
```

```
      Mod_VonKarmonLengthScale = MAX(VonKarmonLengthScale,
C_S_SAS*CellLength*pow(VONKARMON_K*ETA_2/(beta/C_MU - alpha), 0.5));

      Alt_StrainMagSquared = P_k_Tilda/C_MU_T(c, t);

      Q_SAS_Term1 = C_R(c,
t)*ETA_2*VONKARMON_K*VortMag*VortMag*pow(TurbulentLengthScale/Mod_VonKa
rmonLengthScale, 2.0);

      Omega_Dot = NV_DOT(C_UDSI_G(c, t, OMG), C_UDSI_G(c, t,
OMG))/pow(C_UDSI(c, t, OMG), 2.0);

      tke_Dot = NV_DOT(C_UDSI_G(c, t, TKE), C_UDSI_G(c, t,
TKE))/pow(C_UDSI(c, t, TKE), 2.0);

      if(Omega_Dot >= tke_Dot){

            Q_SAS_Term2 = C_SAS*(2.0*C_R(c, t)*C_UDSI(c, t,
0)/SIGMA_PHI)*Omega_Dot;
            dQ_SAS_dw = -2.0*(Q_SAS_Term1 - Q_SAS_Term2)/C_UDSI(c, t,
OMG);  }
              else {
          Q_SAS_Term2 = C_SAS*(2.0*C_R(c, t)*C_UDSI(c, t,
0)/SIGMA_PHI)*tke_Dot;
            dQ_SAS_dw = -2.0*(Q_SAS_Term1)/C_UDSI(c, t, OMG);
                  }

      Q_SAS = MAX(Q_SAS_Term1 - Q_SAS_Term2, 0.0);


      dQ_SAS_dw = -2.0*(Q_SAS)/C_UDSI(c, t, OMG);

      Source = P_w - Y_w + Q_SAS + D_w;

    S_p = MIN(0, dQ_SAS_dw - (D_w + 2.0*Y_w)/C_UDSI(c, t, OMG));

 /*   C_UDMI(c, t, 6) = Source;

      C_UDMI(c, t, 7) = S_p;  */

      C_UDMI(c, t, 5) = Q_SAS;
      C_UDMI(c, t, 6) = Q_SAS_Term1;
      C_UDMI(c, t, 7) = Q_SAS_Term2;
      C_UDMI(c, t, 8) = VortMag/StrainMag;
      C_UDMI(c, t, 9) = VonKarmonLengthScale;
      C_UDMI(c, t, 11) =
C_S_SAS*CellLength*pow(VONKARMON_K*ETA_2/(beta/C_MU - alpha), 0.5);
      C_UDMI(c, t, 12) = Mod_VonKarmonLengthScale;
      C_UDMI(c, t, 13) = Omega_Dot;
      C_UDMI(c, t, 14) = tke_Dot;
      C_UDMI(c, t, 15) = C_MU_T(c,t)*StrainMag*StrainMag/P_k_Tilda;

     dS[eqn] = S_p;
```

```
   return Source;
 }
/*==================Wall boundary====================== */
DEFINE_PROFILE(wall_d_bc,t,i)
{
   Thread *t0;
   face_t f;
   cell_t c;
   double omega_at_wall, wall_dist;
   double C_mu, beta_i;
   int wall_distance_was_zero = 0;
   C_mu = 0.09;
   beta_i = 0.09;
  begin_f_loop(f,t)
  {
     t0 = THREAD_T0(t);
       c = F_C0(f, t);
       wall_dist = C_UDMI(c,t0,WDD_UDM);

       if(wall_dist > 0.0)
       {
       omega_at_wall = 6.0*C_MU_L(c,t0)/(0.075*C_R(c,
t0)*wall_dist*wall_dist);
       }
         else
       {
            omega_at_wall = C_UDSI(c,t0,OMG);
            wall_distance_was_zero++;
       }
     F_PROFILE(f,t,i) = omega_at_wall;
  }
  end_f_loop(f,t)

  if(wall_distance_was_zero > 0)
  {
        Message("Warning: wall distance has not yet been calculated and
stored in C_UDMI(c,t,WDD)\n");
  }
}
/*****************************************************************
UDF for placing limits on turbulent parameters
*****************************************************************/
DEFINE_ADJUST(limit_k_omega, d)
{
/* Domain *d; */
Thread *t;
cell_t c;
d = Get_Domain(1); /* mixture domain if multiphase */
thread_loop_c(t,d)
{
      if (FLUID_THREAD_P(t))
      {
```

```
            begin_c_loop(c,t)
            {
/*
            if(C_UDSI(c,t,TKE) < 1e-8){ printf("Low TKE Found: k=%8.3e,
c=%d\n", C_UDSI(c,t,TKE), c); }
            if(C_UDSI(c,t,TKE) > 1000){ printf("High TKE Found:
k=%8.3e, c=%d\n", C_UDSI(c,t,TKE), c); }
            if(C_UDSI(c,t,OMG) < 10){ printf("Low Spec. Dis. Found:
w=%8.3e c=%d\n", C_UDSI(c,t,OMG), c); }
*/
            if(C_UDSI(c,t,TKE) < MIN_TKE){ C_UDSI(c, t, TKE) = MIN_TKE;
}
            if(C_UDSI(c,t,TKE) > MAX_TKE){ C_UDSI(c, t, TKE) = MAX_TKE;
}
            if(C_UDSI(c,t,OMG) < MIN_OMG){ C_UDSI(c, t, OMG) = MIN_OMG;
}
            if(C_UDSI(c,t,OMG) > MAX_OMG){ C_UDSI(c, t, OMG) = MAX_OMG;
}

            /* C_O(c, t) = 1000.0; */
            }
            end_c_loop(c,t)
      }
}

}
/*****************************************************************
UDF finding f_k based on length scale - grid ratio
*****************************************************************/
DEFINE_EXECUTE_AT_END(f_k_modeled)
{
Domain *d;
Thread *t;
cell_t c;
double CellLength, IntegralLength, dimension;
d = Get_Domain(1); /* mixture domain if multiphase */

dimension = (double) ND_ND;

thread_loop_c(t,d)
{
      if (FLUID_THREAD_P(t))
      {
            begin_c_loop(c,t)
            {
            C_UDSI(c, t, TKE) = MAX(C_UDSI(c, t, TKE), MIN_TKE);
            C_UDSI(c, t, TKE) = MIN(C_UDSI(c, t, TKE), MAX_TKE);
            C_UDSI(c, t, OMG) = MAX(C_UDSI(c, t, OMG), MIN_OMG);
            C_UDSI(c, t, OMG) = MIN(C_UDSI(c, t, OMG), MAX_OMG);

            CellLength = pow(C_VOLUME(c,t), 1.0/dimension);
            IntegralLength = pow(C_UDSI(c, t, TKE),
0.5)/(BETA_STAR_INF*C_UDSI(c, t, OMG));
```

```
            C_UDMI(c, t, 3) = MIN(3.0*pow(CellLength/IntegralLength,
2.0/3.0), 1.0);

            }
            end_c_loop(c,t)
      }
}
}
/************************************************************************
UDF finding f_k based on length scale - grid ratio
************************************************************************/
DEFINE_EXECUTE_AT_END(f_k_mean_k)
{
Domain *d;
Thread *t;
cell_t c;
int i;
double total_k;
double CellLength, IntegralLength, dimension;
d = Get_Domain(1); /* mixture domain if multiphase */

dimension = (double) ND_ND;

i=1;
thread_loop_c(t,d)
{
      if (FLUID_THREAD_P(t))
      {
            begin_c_loop(c,t)
            {

            CellLength = pow(C_VOLUME(c,t), 1.0/dimension);
            total_k = C_UDSI(c, t, 2);  /*  Mean tke from previous SST-
kw solution  */
            IntegralLength = pow(total_k, 0.5)/(BETA_STAR_INF*C_UDSI(c,
t, OMG));
            C_UDMI(c, t, 3) = MIN(3.0*pow(CellLength/IntegralLength,
2.0/3.0), 1.0);

            /*  printf("read velocity %6.2f %6.2f %6.2f %6.2f\n",
CellLength, total_k, IntegralLength, C_UDMI(c, t, 3));  */
            }
            end_c_loop(c,t)
      }
}
}
/************************************************************************
UDF finding f_k based on length scale - grid ratio from Forotutan and
Yavuzkurt
************************************************************************/
DEFINE_EXECUTE_AT_END(Savas_f_k_mean_k)
{
```

```
Domain *d;
Thread *t;
cell_t c;
int i;
double total_k, TIL_to_CellLength_Ratio, Term1, f_k;
double CellLength, IntegralLength, dimension;
d = Get_Domain(1); /* mixture domain if multiphase */

dimension = (double) ND_ND;

i=1;
thread_loop_c(t,d)
{
      if (FLUID_THREAD_P(t))
      {
            begin_c_loop(c,t)
            {
            C_UDSI(c, t, TKE) = MAX(C_UDSI(c, t, TKE), MIN_TKE);
            C_UDSI(c, t, TKE) = MIN(C_UDSI(c, t, TKE), MAX_TKE);
            C_UDSI(c, t, OMG) = MAX(C_UDSI(c, t, OMG), MIN_OMG);
            C_UDSI(c, t, OMG) = MIN(C_UDSI(c, t, OMG), MAX_OMG);

            CellLength = pow(C_VOLUME(c,t), 1.0/dimension);
            total_k = C_UDSI(c, t, 2);  /*  Mean tke from previous SST-
kw solution  */
            IntegralLength = pow(total_k, 0.5)/(BETA_STAR_INF*C_UDSI(c,
t, OMG));
            TIL_to_CellLength_Ratio = IntegralLength/CellLength;
            Term1 = pow(TIL_to_CellLength_Ratio, 2.0/3.0);
            f_k = (1.0 - pow(Term1/(0.23+ Term1), 4.5));
            C_UDMI(c, t, 3) = MAX(C_UDMI(c, t, 0), f_k);

/*          printf("read velocity %6.2e %6.3f %6.2f %6.4f\n",
C_VOLUME(c,t), total_k, C_UDSI(c, t, OMG), C_UDMI(c, t, 3));  */
            }
            end_c_loop(c,t)
      }
}
printf("Update Total f_k");
}
/*********************************************************************
UDF finding f_k based on length scale - grid ratio from Forotutan and
Yavuzkurt
*********************************************************************/
DEFINE_ON_DEMAND(OD_Savas_f_k_mean_k)
{
Domain *d;
Thread *t;
cell_t c;
int i;
double total_k, TIL_to_CellLength_Ratio, Term1, f_k;
double CellLength, IntegralLength, dimension;
d = Get_Domain(1); /* mixture domain if multiphase */
```

```
dimension = (double) ND_ND;

i=1;
thread_loop_c(t,d)
{
      if (FLUID_THREAD_P(t))
      {
            begin_c_loop(c,t)
            {
            C_UDSI(c, t, TKE) = MAX(C_UDSI(c, t, TKE), MIN_TKE);
            C_UDSI(c, t, TKE) = MIN(C_UDSI(c, t, TKE), MAX_TKE);
            C_UDSI(c, t, OMG) = MAX(C_UDSI(c, t, OMG), MIN_OMG);
            C_UDSI(c, t, OMG) = MIN(C_UDSI(c, t, OMG), MAX_OMG);

            CellLength = pow(C_VOLUME(c,t), 1.0/dimension);
            total_k = C_UDSI(c, t, 2);  /*  Mean tke from previous SST-
kw solution  */
            IntegralLength = pow(total_k, 0.5)/(BETA_STAR_INF*C_UDSI(c,
t, 3));
            TIL_to_CellLength_Ratio = IntegralLength/CellLength;
            Term1 = pow(TIL_to_CellLength_Ratio, 2.0/3.0);
            f_k = (1.0 - pow(Term1/(0.23+ Term1), 4.5));
            C_UDMI(c, t, 3) = MAX(C_UDMI(c, t, 0), f_k);

/*          printf("read velocity %6.2e %6.3f %6.2f %6.4f\n",
C_VOLUME(c,t), total_k, C_UDSI(c, t, OMG), C_UDMI(c, t, 3));  */
            }
            end_c_loop(c,t)
      }
}
printf("Update Total f_k");
}

void uds_derivatives(Domain *d, int n)
{
   /* Code to compute derivative of a variable.  Variable storage
allocation first.... */
        MD_Alloc_Storage_Vars(d, SV_UDSI_RG(n), SV_UDSI_G(n), SV_NULL);
        Scalar_Reconstruction(d, SV_UDS_I(n), -1, SV_UDSI_RG(n), NULL);
        Scalar_Derivatives(d, SV_UDS_I(n), -1, SV_UDSI_G(n),
SV_UDSI_RG(n), NULL);
        return;
}
/*****************************************************************
Calculate Q_SAS at the end of each iteration
*****************************************************************/
DEFINE_ADJUST(Update_Vel_Deriv, d)
{
/*    Domain *d;
       d = Get_Domain(1); */
      Thread *t;
      cell_t c;
```

```
    int i, n;

    thread_loop_c (t,d)
      begin_c_loop (c,t)

            C_UDSI(c, t, TKE) = MAX(C_UDSI(c, t, TKE), MIN_TKE);
            C_UDSI(c, t, TKE) = MIN(C_UDSI(c, t, TKE), MAX_TKE);
            C_UDSI(c, t, OMG) = MAX(C_UDSI(c, t, OMG), MIN_OMG);
            C_UDSI(c, t, OMG) = MIN(C_UDSI(c, t, OMG), MAX_OMG);

            for(i=0; i<3; i++){
                  C_UDSI(c, t, 3+i) = C_U_G(c,t)[i];
                  C_UDSI(c, t, 6+i) = C_V_G(c,t)[i];
                  C_UDSI(c, t, 9+i) = C_W_G(c,t)[i];
            }

      end_c_loop (c,t)

/*    Message("Finding Velocity Second Derivatives . . . \n");  */

    for(n=0; n<n_uds; ++n) uds_derivatives(d, n);



}
double coerce(double x, double min, double max)
{
      double temp;
      temp = MIN(x, max);
      temp = MAX(temp, min);
      return temp;
}
/************************************************************************
UDF finding f_k based on length scale - grid ratio
************************************************************************/
DEFINE_EXECUTE_AT_END(Update_Total_TKE)
{
Domain *d;
Thread *t;
cell_t c;
double U, V, W, total_k, tke_res;
double dimension;
d = Get_Domain(1); /* mixture domain if multiphase */
printf("Hi Mom!\n");
dimension = (double) ND_ND;

thread_loop_c(t,d)
{
      if (FLUID_THREAD_P(t))
      {
            begin_c_loop(c,t)
            {
```

```
            U = C_UDSI(c, t, 3);
            V = C_UDSI(c, t, 4);
            W = C_UDSI(c, t, 5);

            tke_res = 0.5*(U - C_U(c,t))*(U - C_U(c,t)) +
                          0.5*(V - C_V(c,t))*(V - C_V(c,t)) +
                          0.5*(W - C_W(c,t))*(W - C_W(c,t));

            total_k = tke_res + C_UDSI(c, t, TKE);

            C_UDSI(c, t, 2) = total_k;

            }
            end_c_loop(c,t)
      }
      printf("Update Total TKE");
}


}
```

B. TIME AVERAGED PARAMETERS FROM TRANSIENT SOLUTIONS

Details are of the time averaged transient results are presented in this section. This includes the 10 sub-averages of the local Nusselt number used to find the overall averaged presented section 5.1 and 5.1.2.5. In addition, the sub-averages for each portion of the object is also presented in this section. Finally, the frequency domain of the velocity trace taken downstream from the object is provided.

Staggered tube bank SST detailed results

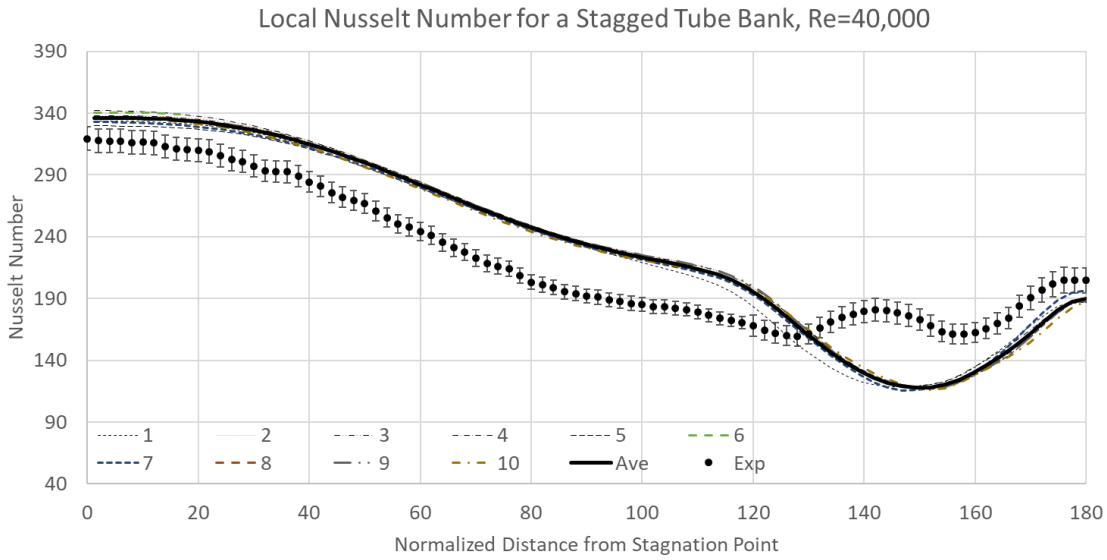

Figure B.1 Averaged local Nusselt number for SST model

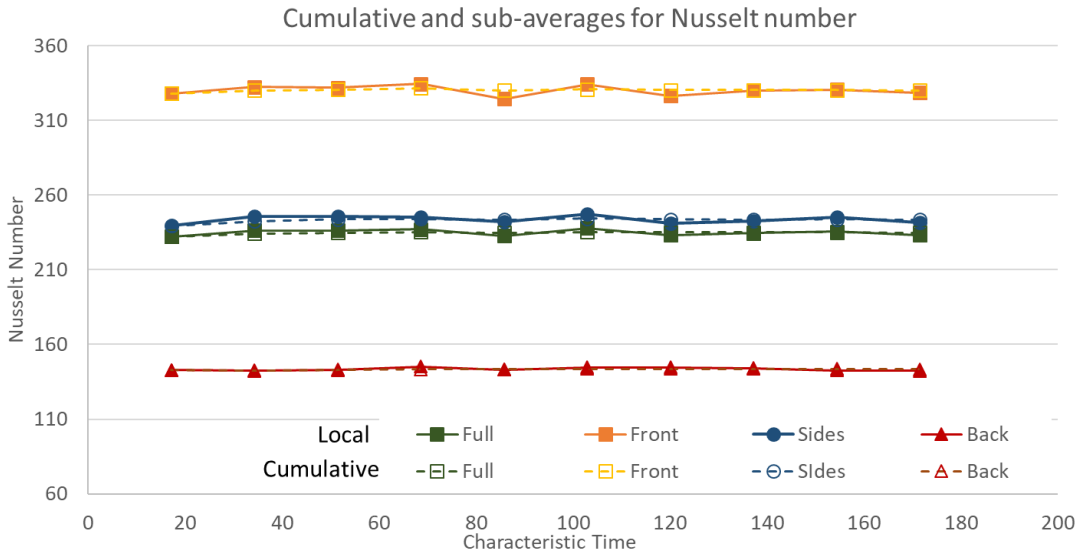

Figure B.2 Averaged local Nusselt number by sector for SST model

Staggered tube bank SST-SAS detailed results

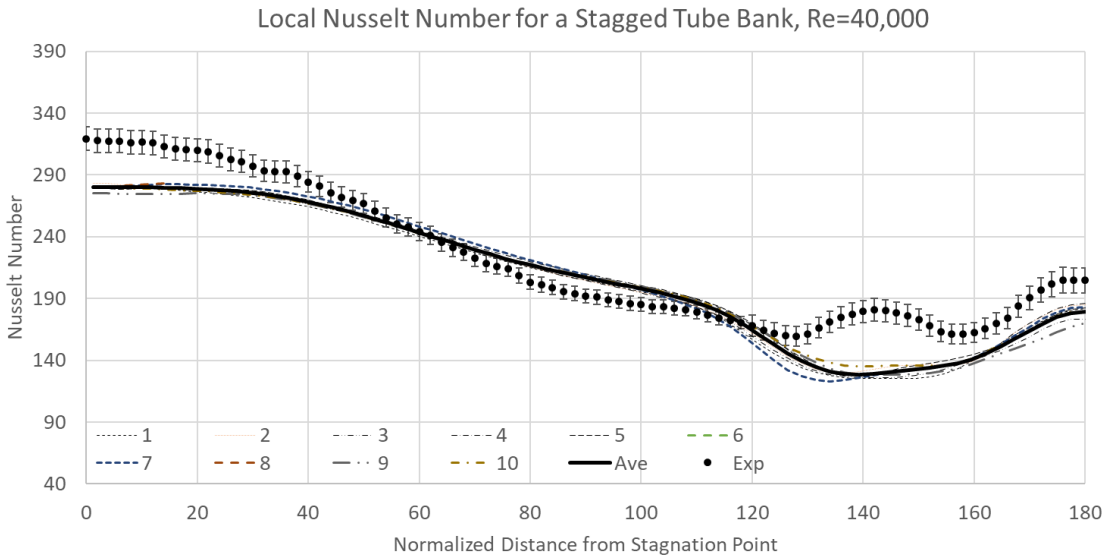

Figure B.3 Averaged local Nusselt number for SST-SAS model

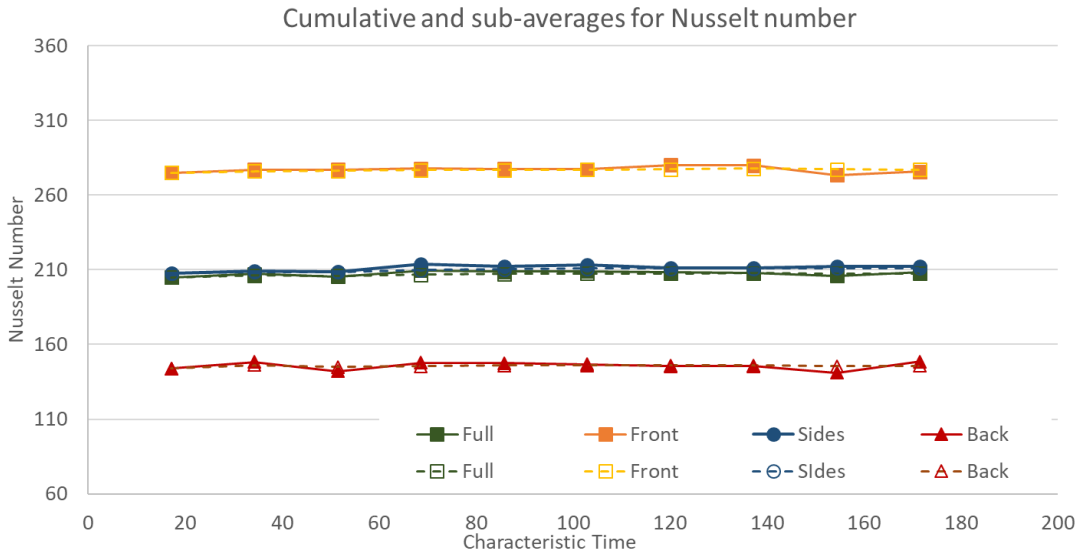

Figure B.4 Averaged local Nusselt number by sector for SST-SAS model

Staggered tube bank RSM detailed results

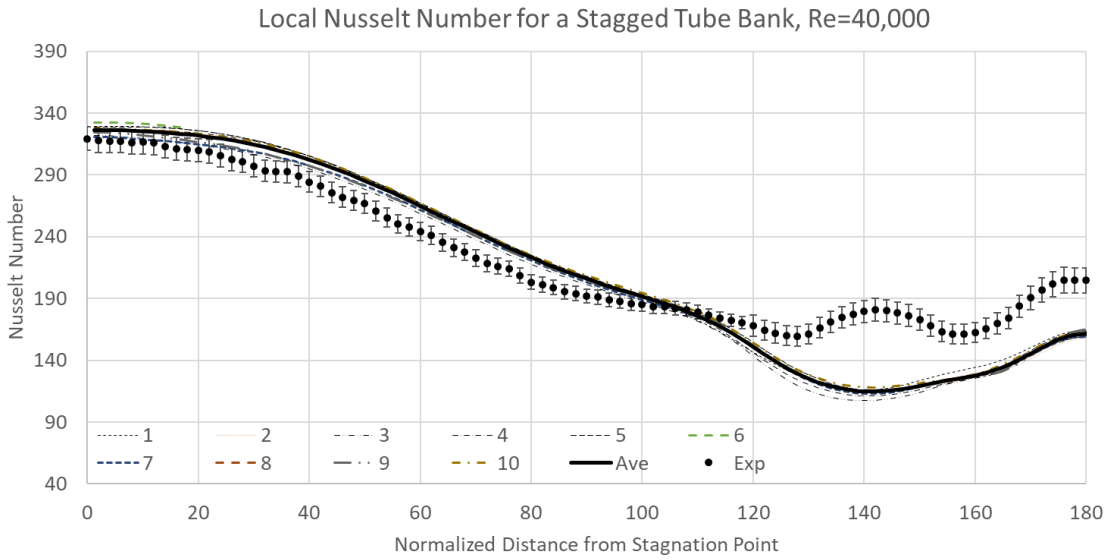

Figure B.5 Averaged local Nusselt number for RSM model

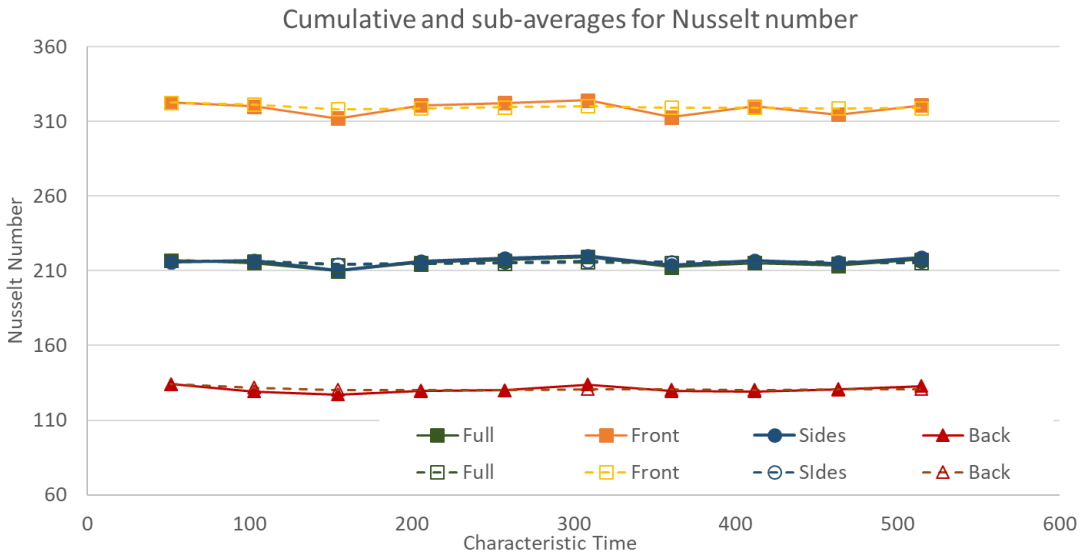

Figure B.6 Averaged local Nusselt number by sector for RSM model

Staggered tube bank PANS-SST detailed results

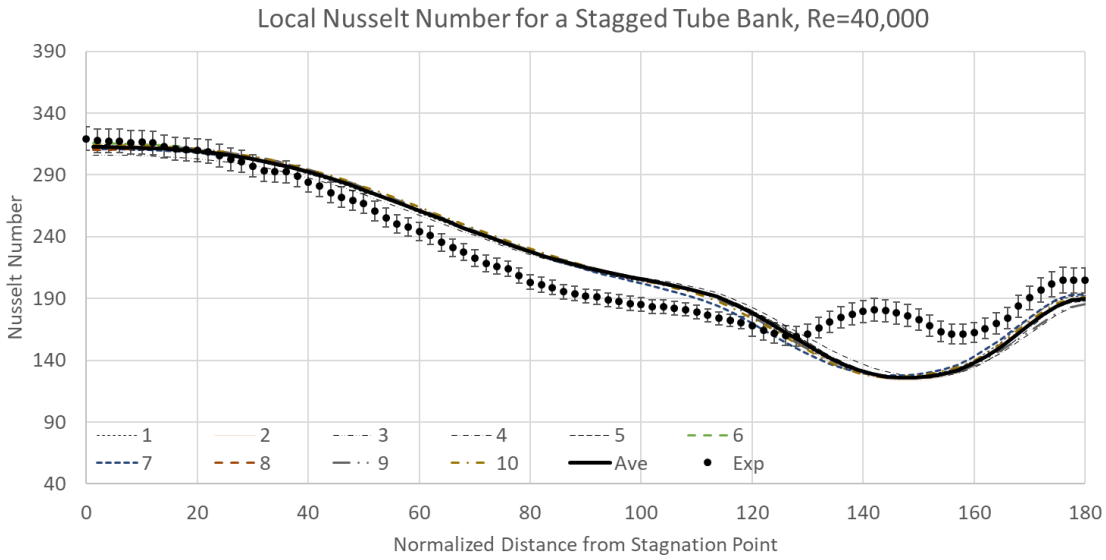

Figure B.7 Averaged local Nusselt number for PANS-SST model

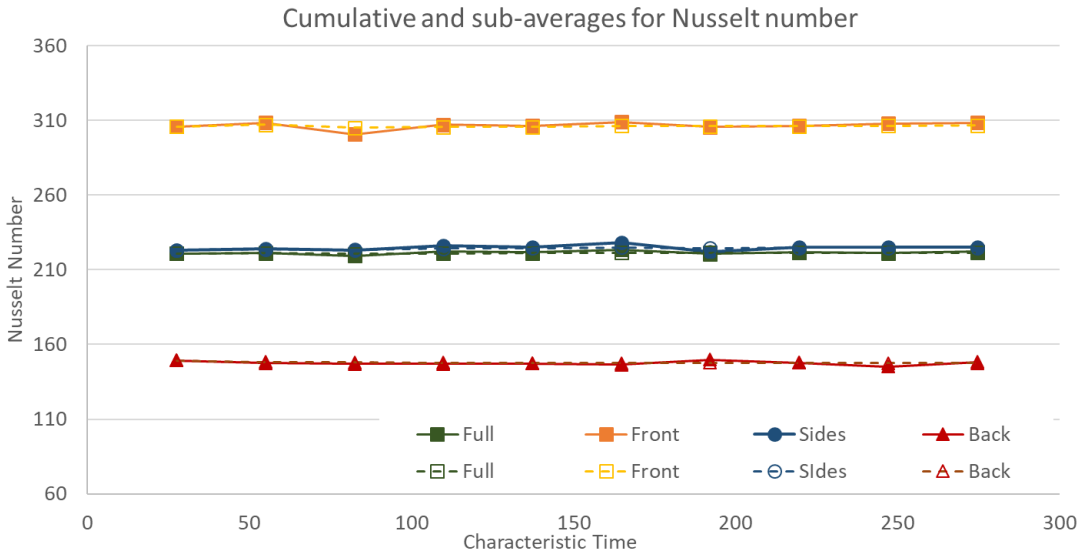

Figure B.8 Averaged local Nusselt number by sector for PANS-SST model

Staggered tube bank DES detailed results

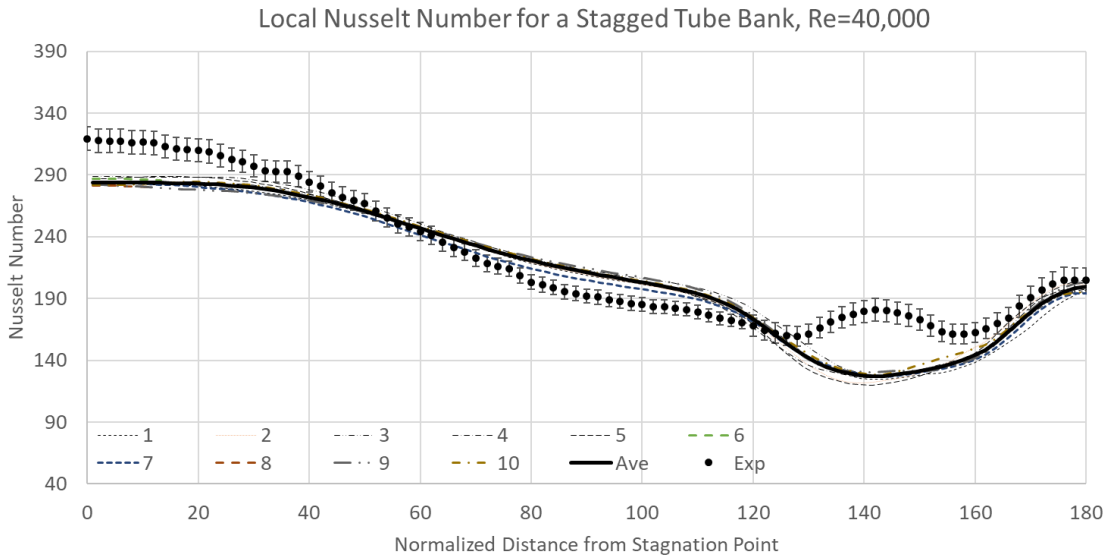

Figure B.9 Averaged local Nusselt number for DES model

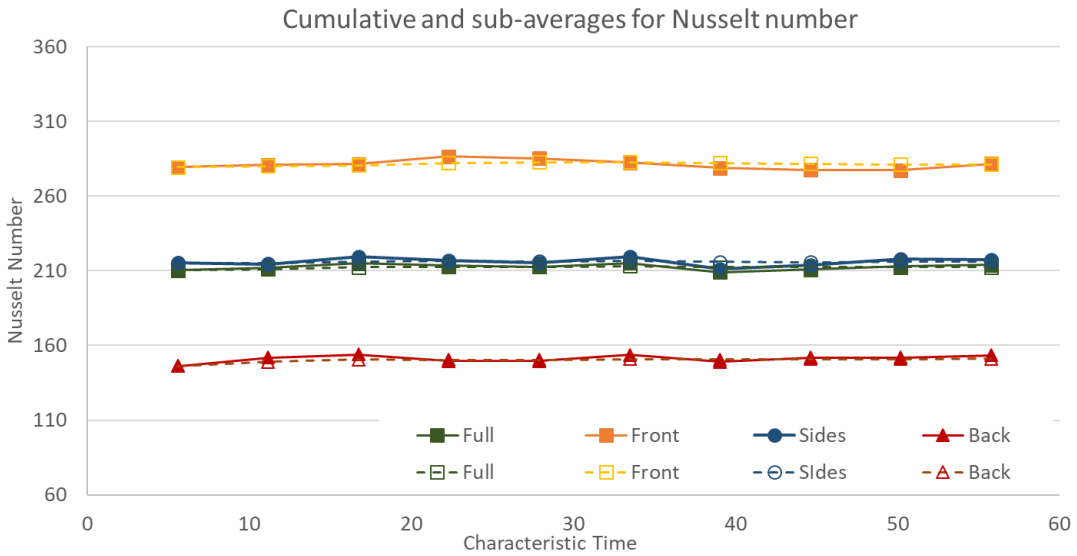

Figure B.10 Averaged local Nusselt number by sector for DES model

Staggered tube bank LES detailed results

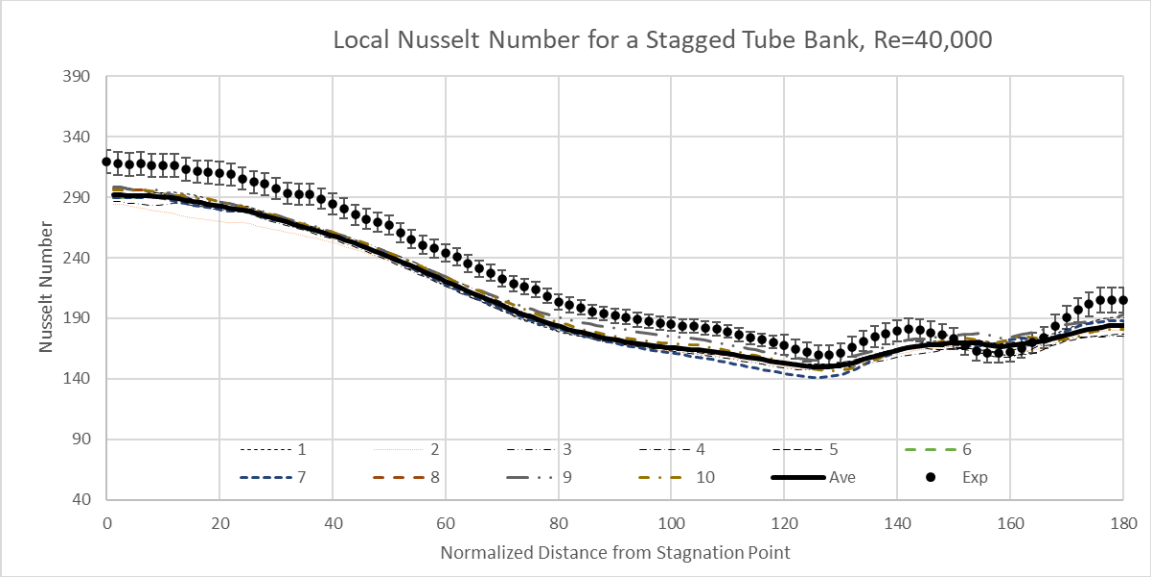

Figure B.11 Averaged local Nusselt number for LES Model

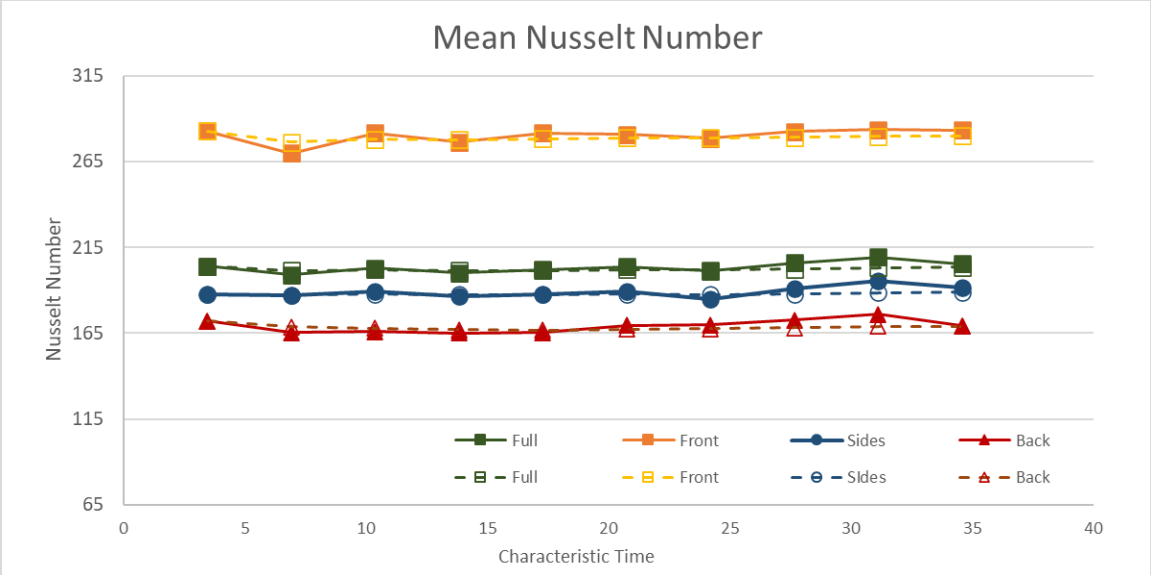

Figure B.12 Averaged local Nusselt number by sector for LES Model

Square in cross flow SST detailed results

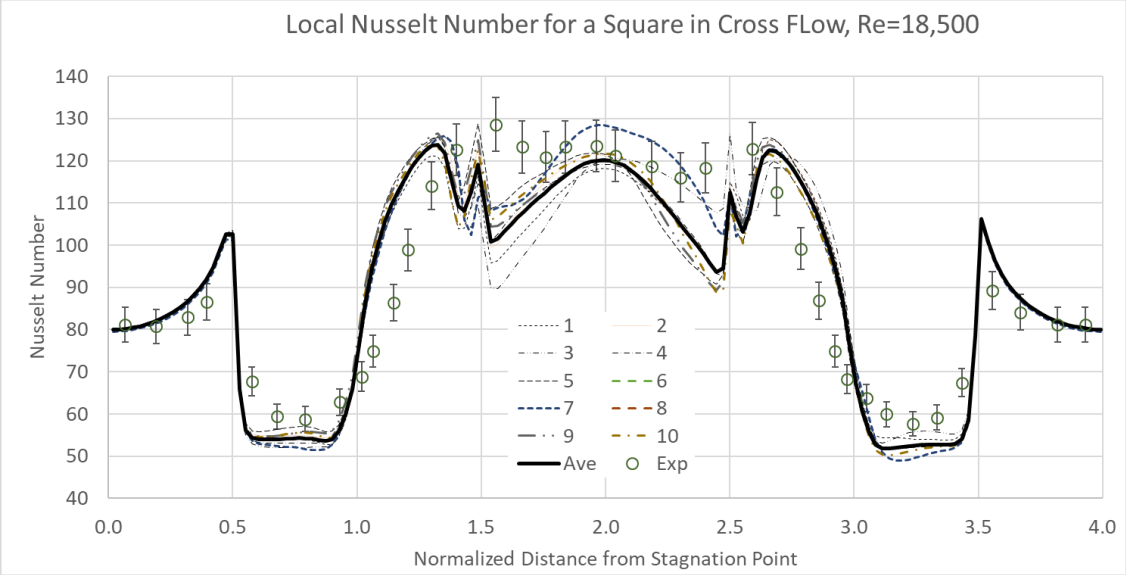

Figure B.13 Square in cross flow; averaged local Nusselt number for SST Model

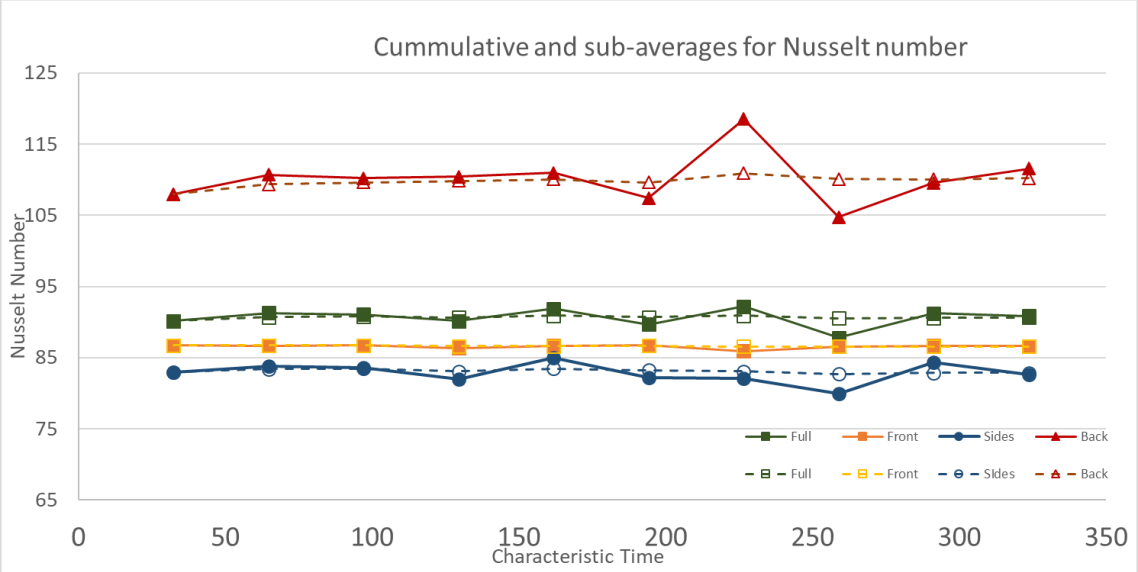

Figure B.14 Square in cross flow; averaged local Nusselt number by sector for SST Model

Square in cross flow SST-SAS detailed results

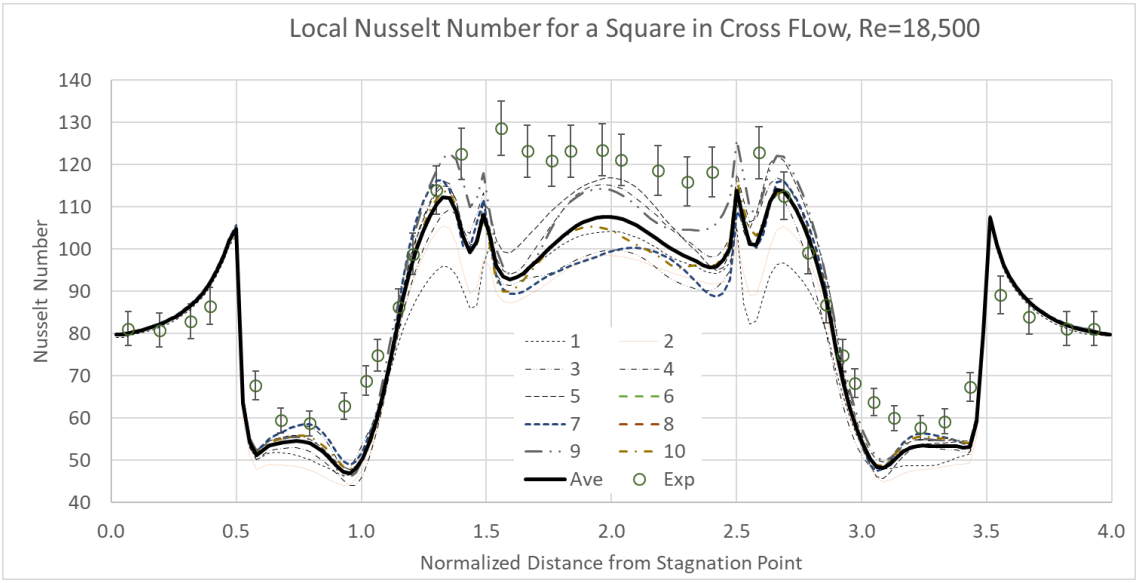

Figure B.15 Square in cross flow; averaged local Nusselt number for SST-SAS Model

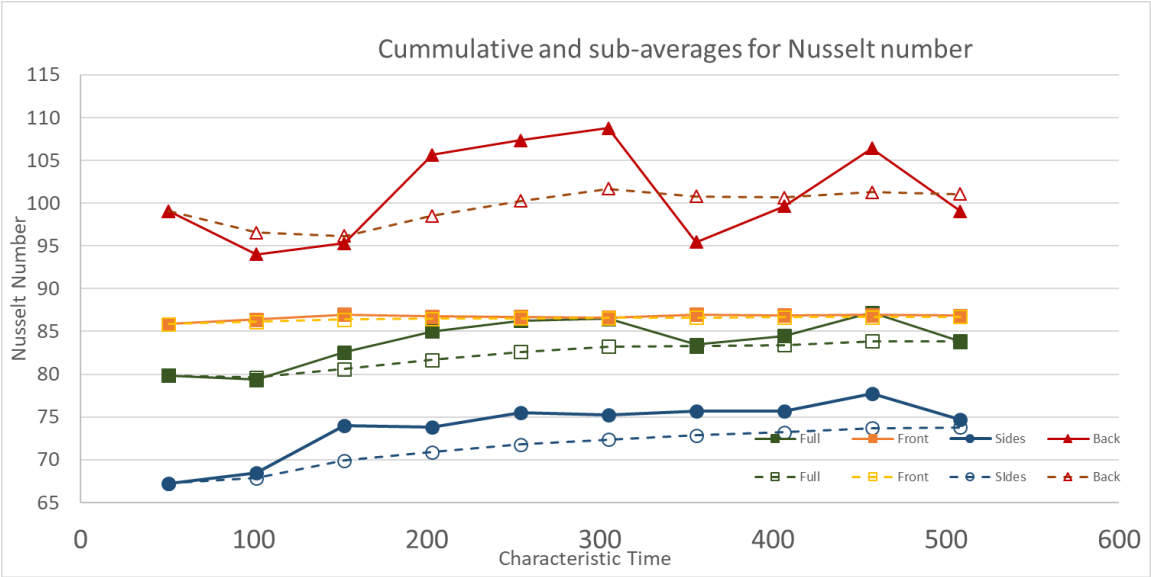

Figure B.16 Square in cross flow; averaged local Nusselt number by sector: SST-SAS Model

Square in cross flow RSM detailed results

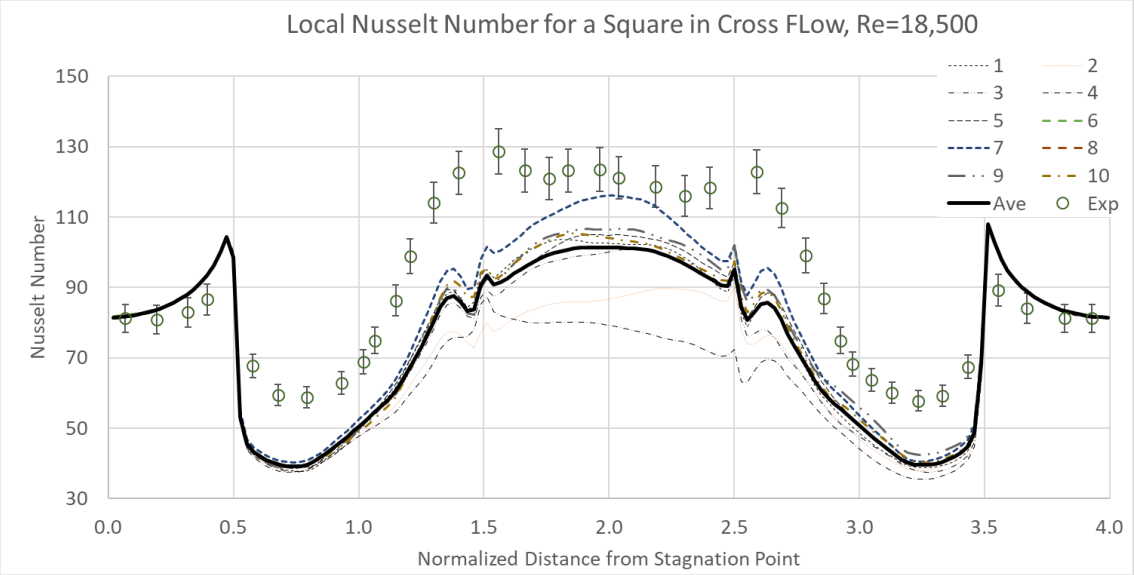

Figure B.17 Square in cross flow; averaged local Nusselt number for RSM model

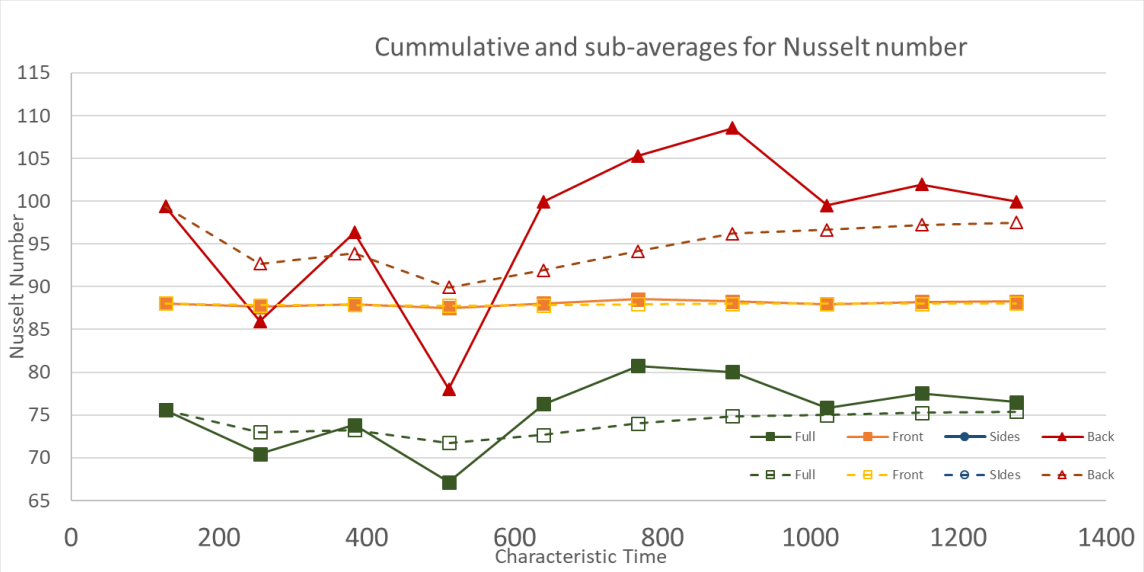

Figure B.18 Square in cross flow; averaged local Nusselt number by sector for RSM model

Square in cross flow PANS-SST detailed results

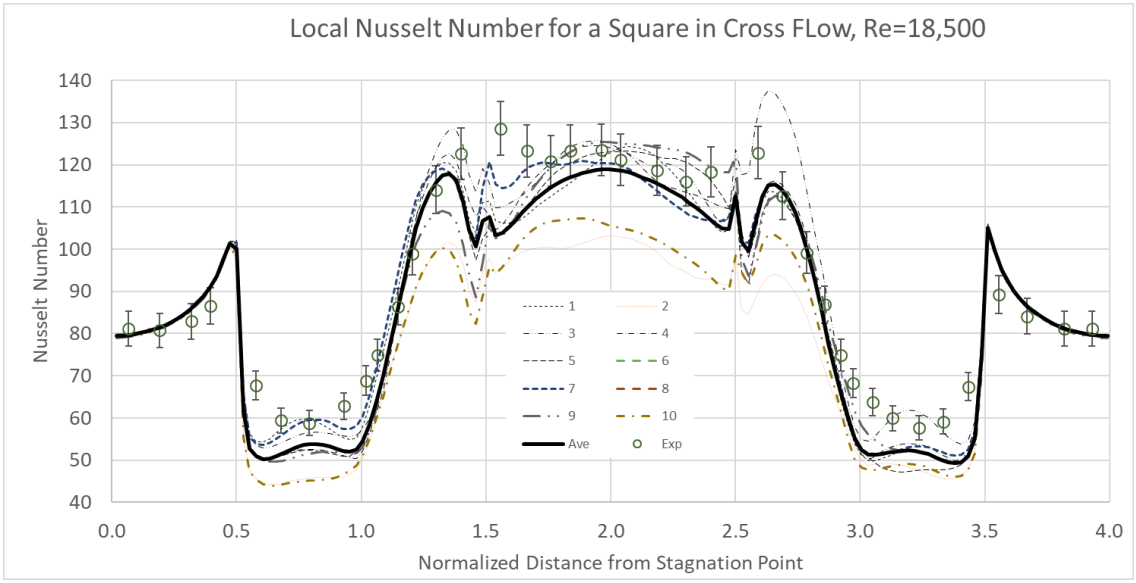

Figure B.19 Square in cross flow; averaged local Nusselt number for PANS-SST Model

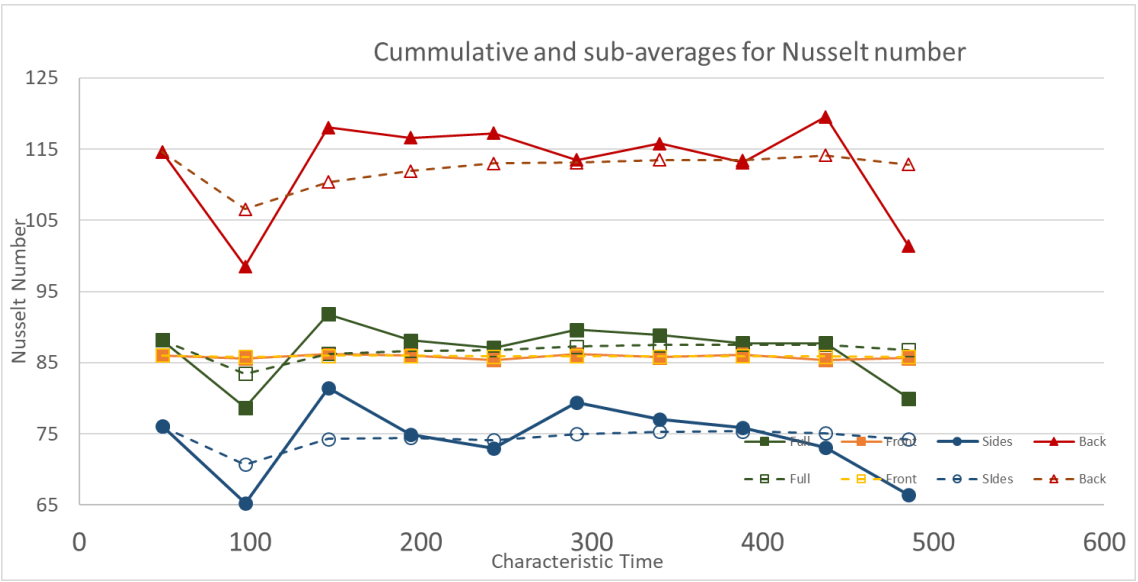

Figure B.20 Square in cross flow; averaged local Nusselt number by sector for PANS-SST Model

Square in cross flow DES detailed results

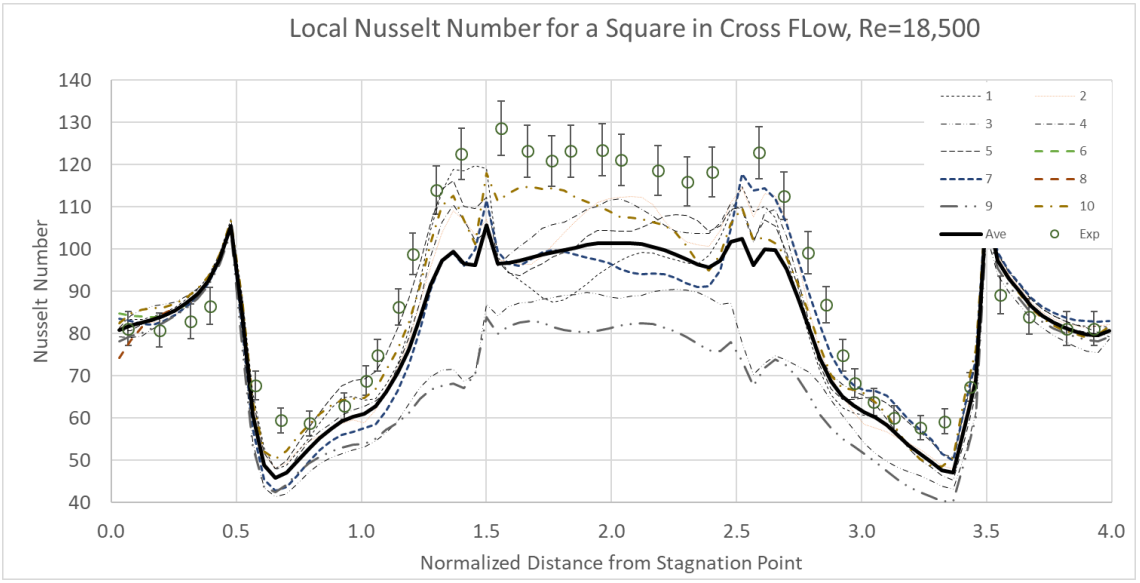

Figure B.21 Square in cross flow; averaged local Nusselt number for DES model

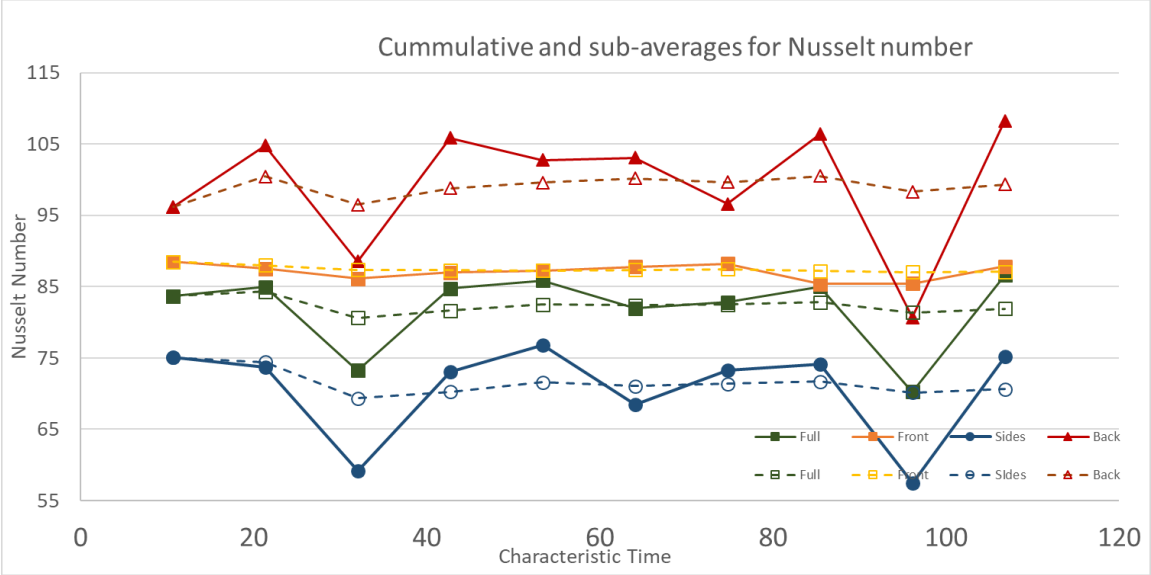

Figure B.22 Square in cross flow; averaged local Nusselt number by sector for DES Model

Square in cross flow LES detailed results

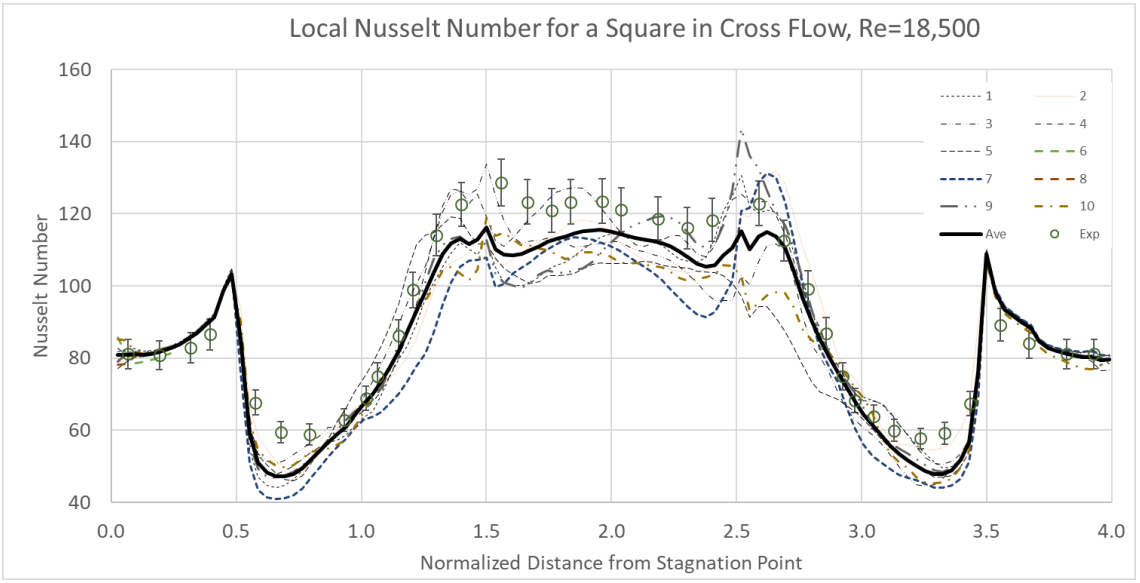

Figure B.23 Square in cross flow; averaged local Nusselt number for LES model

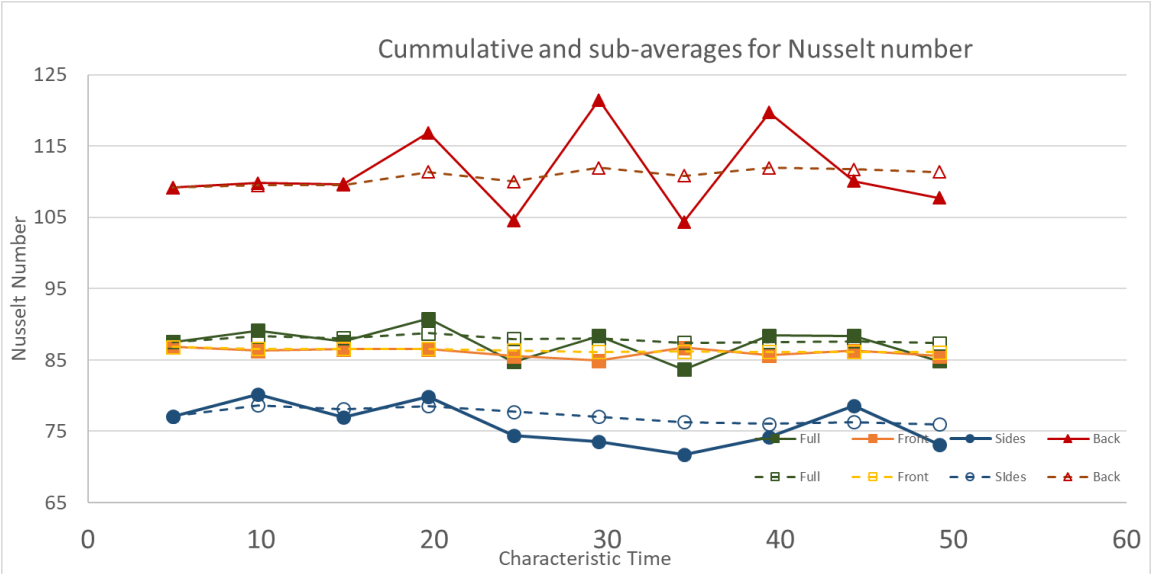

Figure B.24 Square in cross flow; averaged local Nusselt number by sector for LES model